INFORMATION TO USERS

This manuscript has been reproduced from the microfilm master. UMI films the text directly from the original or copy submitted. Thus, some thesis and dissertation copies are in typewriter face, while others may be from any type of computer printer.

The quality of this reproduction is dependent upon the quality of the copy submitted. Broken or indistinct print, colored or poor quality illustrations and photographs, print bleedthrough, substandard margins, and improper alignment can adversely affect reproduction.

In the unlikely event that the author did not send UMI a complete manuscript and there are missing pages, these will be noted. Also, if unauthorized copyright material had to be removed, a note will indicate the deletion.

Oversize materials (e.g., maps, drawings, charts) are reproduced by sectioning the original, beginning at the upper left-hand corner and continuing from left to right in equal sections with small overlaps. Each original is also photographed in one exposure and is included in reduced form at the back of the book.

Photographs included in the original manuscript have been reproduced xerographically in this copy. Higher quality 6" x 9" black and white photographic prints are available for any photographs or illustrations appearing in this copy for an additional charge. Contact UMI directly to order.

UMI

A Bell & Howell Information Company
300 North Zeeb Road, Ann Arbor MI 48106-1346 USA
313/761-4700 800/521-0600

BOUNDARY DETECTION IN ULTRASONIC SPECKLE

BY

RICHARD NORMAN CZERWINSKI

B.S.E.E., Drexel University, 1990
M.S., University of Illinois at Urbana–Champaign, 1993

THESIS

Submitted in partial fulfillment of the requirements
for the degree of Doctor of Philosophy in Electrical Engineering
in the Graduate College of the
University of Illinois at Urbana-Champaign, 1996

Urbana, Illinois

UNIVERSITY OF ILLINOIS AT URBANA-CHAMPAIGN

THE GRADUATE COLLEGE

JULY 1996

WE HEREBY RECOMMEND THAT THE THESIS BY

RICHARD NORMAN CZERWINSKI

ENTITLED BOUNDARY DETECTION IN ULTRASONIC SPECKLE

BE ACCEPTED IN PARTIAL FULFILLMENT OF THE REQUIREMENTS FOR

THE DEGREE OF DOCTOR OF PHILOSOPHY

W. O'Brien Douglas L. Jones
Director of Thesis Research

D. M. Craig
Head of Department

Committee on Final Examination†

Douglas L. Jones W. O'Brien
Chairperson

Brian Bar

David C. Munson, Jr.

† Required for doctor's degree but not for master's.

O-517

BOUNDARY DETECTION IN ULTRASONIC SPECKLE

Richard Norman Czerwinski, Ph.D.
Department of Electrical and Computer Engineering
University of Illinois at Urbana–Champaign, 1996
Douglas L. Jones and William D. O'Brien, Jr., Advisors

This dissertation considers the problem of detecting boundaries in ultrasound speckle imagery. For physiological reasons, we argue that boundaries between tissue layers appear as lines in ultrasound scans and approach the boundary detection problem as one of detecting lines of unknown orientation. We define a set of "sticks," short line segments of variable orientation that can locally approximate the boundaries. Using the physical principles that account for the speckle phenomenon, we derive the optimal detector for sticks of unknown orientation in fully developed speckle and compare the optimal detector to several suboptimal detection rules which are more computationally efficient. We show that when the underlying Gaussian random process underlying speckle noise is uncorrelated, a very simple suboptimal detection rule is nearly optimal, and that even in colored speckle, a related class of detectors can approach optimal performance. The basic technique is then extended in a number of ways to improve its performance. We investigate the effect of varying the size and shape of the sticks and show that these variations affect the performance of the algorithm in very fundamental ways, for example, by making it more or less sensitive to thinner or more tightly curving boundaries. We also present a means of improving performance by estimating the distribution function of the orientation of the line passing through each point. Next, we show that images can be "stained" for easier visual interpretation by applying to each pixel a false color whose hue is related to the orientation of the most prominent line segment at that point. Finally, an analysis is given of boundary detection approaches in radio-frequency ultrasound.

DEDICATION

To Baby
with sadness and love.

ACKNOWLEDGMENTS

During the past four years, this research was funded by the National Live Stock and Meat Board, the United States Department of Agriculture, the United States Army, and PHS Grant Number 5 T32 CA 09067, awarded by the National Cancer Institute, DHHS.

For one month In the winter of 1995, this work was conducted in the Interactive Systems Design Laboratory at the University of Washington, Seattle, WA. I gratefully acknowledge Professor Douglas Jones and his family for allowing me to stay at their home during my time there, Professor David C. Munson, Jr. and Ms. Jung-Ah Lee for accommodating my travel plans when arranging the responsibilities for my teaching assistantship that semester, and Professor Les Atlas and his research group at the University of Washington for the use of their computer laboratory.

During my stay at Illinois, I have been fortunate to enjoy the support and friendship of a great many talented individuals who have helped me in the successful completion of my degree. In particular, my advisors, Professors Douglas L. Jones and William D. O'Brien, Jr., have provided a collegial friendship, expert technical guidance and steady funding which enabled me to continue this research. My other committee members, Professors Yoram Bresler and David C. Munson, Jr., have also provided many helpful comments and suggestions, resulting in substantial improvements to this document.

I also wish to acknowledge:

• Akbar Sayeed, Samit Basu, and G. Harikumar for many technical conversations which have helped me to refine my ideas,

• my colleagues in the Coordinated Science Laboratory: Rich Baraniuk, Wade Bastien, Al Delaney, Lee Garth, Andy Hull, Ian Kerfoot, Mike Kramer, Brian Krongold, Jung-Ah Lee, Xiaohui Li, Jeff Mast, Jeff Meunier, Aria Nosratinia, Brett Robertson, Bernard Schnaufer, Sergio Servetto, Rob Soni, Jennifer Webb, Parker Willis, and Chris Young, for the stimulating laboratory environment in which I was fortunate to work.

• my colleagues in the Bioacoustics Research Laboratory: Eric Chen, Scott Ellis, Kate Frazier, Darshan Gandhi, Amjad Safvi, Nadine Smith, and Dudley Swiney, for providing the ultrasound perspective which has helped make my signal processing work practical,

• my friends: Allan Archer, Dean Chung, Beth, Lippold and Carl Haken, Jonas Heuer, Joe Hilliard, Laurie and Paul Hovland, Joan and Greg Paul, Juliann Seebauer, Tim Spila, Angi Vock, and Charley Williams for many pleasant hours of extracurricular diversion which refreshed my mind and spirit,

• my family, Theresa, Dick and Steve Czerwinski, for their patience with me as I pursued a degree which kept me 1000 miles from home for six long years, and

• my in-laws, Geri, Jim, John Paul, Greg, Jennelle and Gregory Gill for accepting me so readily into their family.

Finally, I offer sincere thanks to my wife Wendy for her support and encouragement during the past four years, a time filled with both happy memories and real tragedy, a true slice of life itself. It is my fondest privilege to walk through life with her.

TABLE OF CONTENTS

LIST OF TABLES

Table **Page**

LIST OF FIGURES

CHAPTER 1

INTRODUCTION

1.1 Ultrasound Medical Imaging

Ultrasound is a pulse-echo imaging modality based on interrogation of tissue with high frequency focused sound waves. Its use in medical imaging, particularly of the fetus, has become widespread because it is inexpensive and safe. Furthermore, because ultrasound images can be produced in real time, the modality allows for imaging dynamic structures such as the beating heart, as well as for exploratory imaging.

Ultrasound interrogation is accomplished by focusing a beam of high frequency coherent sound into tissue by means of a transducer, which also acts as a receiver, capturing the returned signal containing reflections from structures lying within the tissue. An image is formed by geometrically aligning echo signals – a linear scan is formed from a sequence of parallel interrogations from a sequence of starting positions lying on a line; a sector scan is formed by sweeping the beam through a range of angles from a single starting point. In both cases, a constant speed of sound is assumed so that the depth of a scatterer is directly proportional to the time delay of its reflection.

The strongest reflections of acoustic energy tend to come from large structures oriented nearly perpendicularly to the interrogating beam. In addition, ultrasound backscatter also contains reflections of the interrogating pulse from a large number of small scatterers spaced densely within the tissue. The effect of these diffuse scatterers is to produce a form of interference in ultrasound images, known as "speckle noise." Speckle is a phenomenon common to many coherent imaging systems, such as synthetic aperture radar (SAR) and laser holography. Although it is often viewed as noise, speckle is signal dependent because it contains information about the subresolvable structure of the tissue.

Medical ultrasound imaging systems are designed to make speckle usable for human diagnosis, instead of suppressing it. Skilled sonographers can interpret the "texture" of the speckle; for example a "shadowed" region may indicate the presence of a nearby sound absorbing or highly reflective region of tissue. Modern image quality is such that even untrained individuals are often able to make out features through the speckle. However, in optimizing images for visual interpretation, the problem of computer detection of boundaries is completely overlooked. The texture which provides diagnostic information can make computer detection of boundaries difficult.

In cases in which computer intervention may be necessary or convenient, such as in fetal maturity estimation or ultrasound mammography, conventional images pose unusual challenges for computer vision algorithms, which are usually designed for use in high signal to noise ratios (SNRs). This thesis considers the problem of detecting boundaries in medical ultrasound imagery and represents a contribution to the field of pattern analysis in speckle imagery. The main result is an image enhancement technique that facilitates boundary detection; detection itself is performed on the enhanced image by applying a threshold, perhaps after further enhancement, such as by a dynamic programming approach to edge linking.

This work is primarily distinguished from other edge detection procedures by its use of a line process (rather than a step process) to model the boundaries. This is appropriate because of the nature of the boundaries in ultrasound imagery – cross-sectional views of the two-dimensional surfaces separating tissue layers. These surfaces are generally smooth on the scale of the scan line spacing, and so appear in cross-section as curving lines. In a sufficiently small region surrounding each point on a boundary, the boundary appears as a straight line of variable orientation.

Thus, boundary detection can be phrased as a composite hypothesis testing problem and approached with the methods of statistical detection theory. The ultimate goal is to develop statistically motivated techniques to determine whether one of a set of short straight line segments ("sticks") of variable orientation is present passing through each pixel. This determination is made using local information from the pixel itself as well as from nearby pixels which are likely to be statistically correlated, especially when a boundary is truly present.

1.2 Overview of This Document

This thesis provides a complete study of statistical methods of boundary (line) detection in speckle, which can be extended to other pattern analysis problems in speckle. For purposes of analysis, speckle is assumed to be distributed as a correlated Rayleigh or Rician random field, as predicted by a reasonable model for the scattering process, described in Chapter 2. The treatment in Chapter 2 is adapted from [2], [3], [4] and [5], with some additional material from other sources to fill in the gaps. We know of no single published source which treats this material in the depth presented here.

The detection itself can be accomplished by a variety of different methods, ranging from an optimal likelihood ratio detection rule through less computationally intensive linear-quadratic detectors to very simple linear rules and *ad hoc* approaches. These detectors are defined in Chapter 3 and compared in performance by *Monte Carlo* simulation.

Chapter 4 contains a discussion of some useful extensions to the basic technique described in Chapter 3. In particular, it discusses the effects of varying the length and thickness of the template sticks. The chapter also presents a procedure for improving the algorithm's performance by inferring a distribution function on the angle of the line passing through each point. Finally, Chapter 4 presents a technique for applying false color to an image to visually enhance boundaries. The basic line detection technique developed in Chapters 3 and 4 was used as part of a larger package of software on a large scale data analysis project undertaken jointly by the Bioacoustics Research Laboratory and the Meat Science Laboratory of the University of Illinois. The operating manual for this software package is included in an appendix to this dissertation.

Chapter 5 extends the results in Chapters 3 and 4 to the detection of boundaries in radio frequency ultrasound. Again, the analysis is by simulation, and the performance differential between a coherent detector and an energy detector is noted for each of a number of aberrations that can be introduced into the signal.

Finally, Chapter 6 gives a summary and suggestions for future research.

CHAPTER 2

STATISTICS OF ULTRASOUND SPECKLE

Speckle occurs when a coherent source is used to illuminate a surface (or image through a medium) which is rough on the scale of the wavelength of illumination. The physical process that generates acoustic speckle is common to radar imaging and laser holography; consequently, the statistical properties of the images formed by these different means are similar in form. The discussion here is largely adapted from from [2], [3], [4] and [5], with some additional material from other sources to fill in the gaps. We know of no single published source which treats this material in this depth.

2.1 First-Order Statistics

2.1.1 Fully developed speckle

The first-order (pointwise) statistics of ultrasound speckle are derived using an argument exactly analogous to the one used to describe laser speckle statistics in [2]. Consider a radio frequency ultrasound trace. If there is no large target present in the trace, the most significant reflections come from numerous point scatterers with independent positions and scattering strengths. This scenario is illustrated in Figure 2.1, and leads to a signal of the form:

$$r(t) = \sum_i a_i \, p(t - T_i) \, e^{j\omega(t-T_i)}, \tag{2.1}$$

where $p(t)$ is the transmitted pulse and T_i is twice the time-of-flight to the ith reflector. Note that we have assumed that the reflectors themselves do not modify the pulse except by a real scaling factor a_i. This is a valid assumption when the scatterer size is small with respect to the wavelength; any phase imparted by the scatterers to the reflected signals is assumed to be accounted for by the delay term T_i.

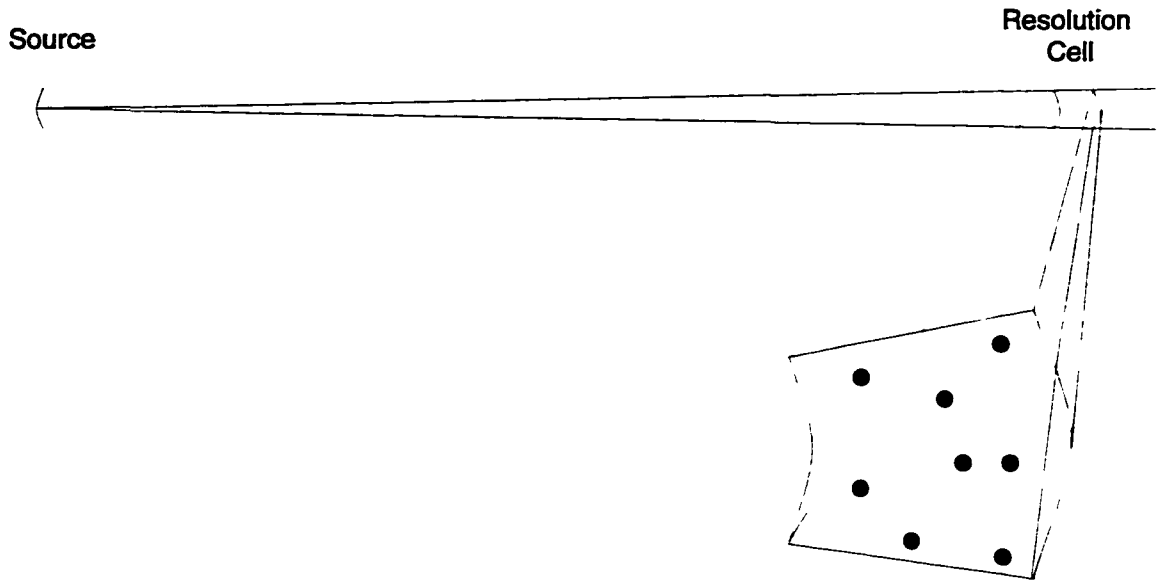

Figure 2.1 Speckle results from coherent interrogation of a rough medium, that is, one containing a distribution of small scatterers with independent positions and scattering strengths.

If the received trace is demodulated and a matched filter applied, the resulting waveform is

$$\begin{aligned}
\hat{r}(t) &= \int p(-\tau) r(t-\tau) e^{-j\omega(t-\tau)} d\tau \\
&= \int p(-\tau) \left[\sum_i a_i \, p(t-\tau-T_i) \, e^{j\omega(t-\tau-T_i)} \right] e^{-j\omega(t-\tau)} d\tau \\
&= \int p(-\tau) \sum_i a_i \, p(t-\tau-T_i) \, e^{-j\omega T_i} \, d\tau \\
&= \sum_i a_i e^{-j\omega T_i} \int p(-\tau) \, p(t-T_i-\tau) \, d\tau \\
&= \sum_i a_i e^{-j\omega T_i} \rho(t-T_i) \\
&= \sum_i |\beta_i| e^{-j\phi_i} \qquad (2.2)
\end{aligned}$$

where

$$\begin{aligned}
\rho(t) &= \int p(-\tau) \, p(t-\tau) \, d\tau \\
&= \int p(\tau) \, p(t+\tau) \, d\tau, \qquad (2.3)
\end{aligned}$$

$$\beta_i = a_i \rho(t - T_i), \tag{2.4}$$

and

$$\phi_i = \begin{cases} \omega T_i & \text{if } \beta_i \geq 0 \\ \omega T_i + \pi & \text{if } \beta_i < 0 \end{cases}, \tag{2.5}$$

If each resolution cell contains a large number of scatterers whose scattering strengths are independent of each other and of their positions, $i(x)$ can be shown to converge to a circular Gaussian random process by a central limit theorem argument [2], if the α_is are independent and identically distributed. If the scatterers are spaced such that $\omega T_i \text{MOD} 2\pi$ is uniformly distributed on $(0, 2\pi)$, then $r(t)$ takes on a circular Gaussian distribution, i.e., it has independent, identically (Gaussian) distributed real and imaginary parts.

The "circular" nature of this distribution can be seen by considering $i(x)$ as the resultant of a two-dimensional random walk in the complex plane. Each term in the summation is a step of some magnitude and direction. Since the directions are uniformly distributed, the steps in the real and imaginary directions are independent. In the limit of many scatterers, the distribution of the resultant is Gaussian with real and imaginary parts of equal variance, corresponding to a circularly symmetric probability density function (pdf), shown in Figure 2.2.

The complex image function $i(x)$ is inconvenient to display; it is customary in ultrasound to output the *magnitude* of the received signal from each resolution cell as a pixel intensity. The use of the signal magnitude simplifies the detection of the RF signal as well; typically, an envelope detector is used instead of demodulation, so complications such as frequency shifts due to pulse attenuation can be ignored.

Speckle conforming to this simple model is known as "fully-developed" speckle. The pixels of an image exhibiting fully developed speckle have a Rayleigh distribution:

$$p(V) = \begin{cases} \frac{V}{\sigma^2} \exp\left(-\frac{V^2}{2\sigma^2}\right) & \text{if } V \geq 0 \\ 0 & \text{if } V < 0 \end{cases}, \tag{2.6}$$

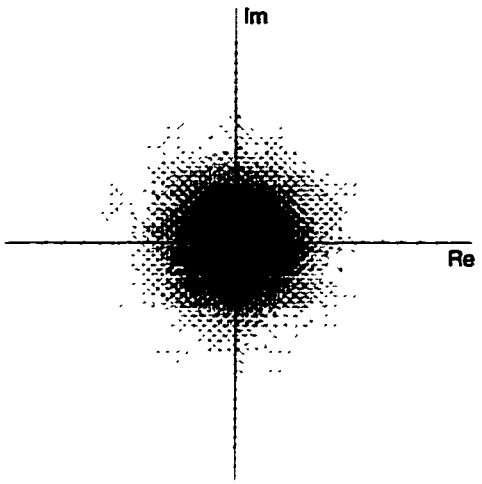

Figure 2.2 Circular complex probability density function for backscatter from many scatterers, each of which contributes an independent step in a uniformly distributed direction.

where σ^2 is the variance of the real or imaginary part of the underlying complex field. Note that the pointwise pdf is not a function of the correlation that may exist between pixels.

2.1.2 Coherent reflectors

If a highly reflective target (such as a structure much larger than a wavelength) is present in a resolution cell, the result is also visualized in terms of the complex random walk analogy: the coherent reflector represents a large step in a single direction which is added to the many small reflections in random directions. The resultant is a circular complex Gaussian random variable with a non-zero complex mean value as shown in Figure 2.3.

The magnitude of a pixel containing coherent reflected energy has a Rician distribution function

$$p(V) = \begin{cases} \frac{V}{\sigma^2} \exp\left(\frac{-(V_s^2+V^2)}{2\sigma^2}\right) \mathrm{I}_0\left(\frac{VV_s}{\sigma^2}\right) & \text{if } V \geq 0 \\ 0 & \text{if } V < 0 \end{cases}, \tag{2.7}$$

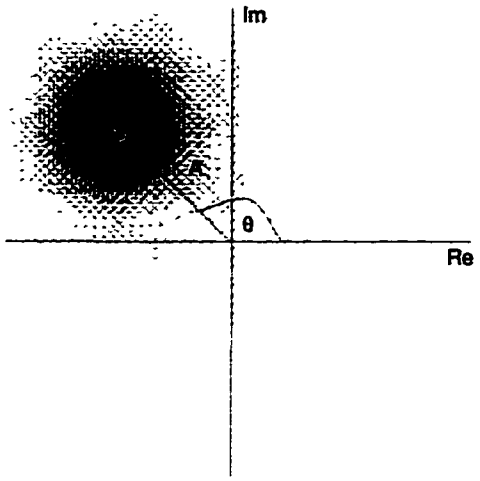

Figure 2.3 Circular complex probability density function for a resolution cell containing a single strong scatterer in addition to diffuse scattering.

where σ^2 is the variance of the real or imaginary part of the underlying complex random variable, I_0 is a modified Bessel function of the first kind, and V_s is the magnitude of the coherent reflection within the resolution cell.

2.2 Second-Order Statistics of Ultrasound Speckle

In the far field of the transducer, the interpixel correlations due to speckle noise are separable into two correlations, one in the axial direction and one in the transverse direction. Correlation between nearby pulses within a single trace (axial correlation) is due to an intersymbol interference-like effect between resolution cells. Correlation between cells on different traces is due to beam diffraction. Because of the independence of these effects, they can be studied separately.

2.2.1 Axial correlation

After detection, the amplitude of a demodulated ultrasound trace at a point corresponding to depth z is given by

$$a(z) = r(2z/c)e^{j\omega 2z/c}$$

$$= \sum_i a_i e^{-j\omega T_i} p(2z/c - T_i) \tag{2.8}$$

where $r(t)$ is defined in (2.1). The correlation function $R_{ax}(z_1, z_2)$ is

$$\begin{aligned}
R_{ax}(z_1, z_2) &= \mathrm{E}[a(z_1)a^*(z_2)] \\
&= \mathrm{E}\left[\sum_i a_i e^{-j\omega T_i} p(2z_1/c - T_i) \sum_k a_k^* e^{j\omega T_k} p(2z_2/c - T_k)\right] \\
&= \sum_i \sum_k \mathrm{E}\left[a_i a_k^*\right] \mathrm{E}\left[e^{-j\omega(T_i - T_k)} p(2z_1/c - T_i) p(2z_2/c - T_k)\right] \\
&= \sum_i \mathrm{E}\left[|a_i|^2\right] \mathrm{E}\left[e^{-j\omega(T_i - T_k)} p(2\delta_i/c) p(2(\Delta z + \delta_i)/c)\right] \\
&\quad + \sum_i \sum_{k \neq i} \mathrm{E}\left[a_i\right] \mathrm{E}\left[a_k^*\right] \mathrm{E}\left[e^{-j\omega(T_i - T_k)} p\left(2\delta_i/c\right) p\left(2(\Delta z + \delta_k)/c\right)\right] \qquad (2.9) \\
&= \sum_i \mathrm{E}\left[|a_i|^2\right] \mathrm{E}\left[e^{-j\omega(T_i - T_k)} p(2\delta_i/c) p(2(\Delta z + \delta_i)/c)\right] \qquad (2.10) \\
&= \sum_i \mathrm{E}\left[|a_i|^2\right] \frac{c/2}{\delta_{max} - \delta_{min}} \int_{\delta_{min}}^{\delta_{max}} p(u) p(u + 2\Delta z/c) du \qquad (2.11)
\end{aligned}$$

where

$$\begin{aligned}
d_i &= \text{the distance from the transducer to the } i\text{th scatterer} \\
T_i &= 2d_i/c \\
\Delta z &= z_1 - z_2 \\
z_2 - d_i &= z_2 - z_1 + z_1 - d_i \text{ and} \\
\delta_k &= z_1 - d_i \\
&= \Delta z + \delta_k, \qquad (2.12)
\end{aligned}$$

and (2.10) follows from (2.9) because the a_i arise from scatterers which are equally likely to contribute constructively or destructively to $r(t)$, and are thus symmetrically distributed about zero, leading to $\mathrm{E}[\mathrm{a_i}] = 0$.

Because we have assumed a convolutional model for the imaging process, the limits on the integral in (2.11) are the support of $p(u)$, and thus the correlation $R_{ax}(z_1, z_2)$ is a

function of the distance $\Delta z = z_1 - z_2$:

$$R_{ax}(z_1, z_2) \propto p(u) * p(-u)|_{v=2\Delta z/c}, \tag{2.13}$$

where $*$ denotes convolution. This is the accepted result for the axial correlation function.

2.2.2 Transverse correlation

In the transverse direction, the correlation is caused by diffraction of the beam as it proceeds into the tissue. If we assume homogeneous, constant speed sound propagation and that the tissue is being imaged in the far field of the transducer, the correlation function is dependent only on the size and shape of the transducer aperture, and not on properties of the medium.

A monochromatic, monodirectional plane wave propagating through free space is modified according to the Huygens-Fresnel point-spread function [6]:

$$\begin{aligned} h(x,y,d) &= \mathcal{F}^{-1}\left\{e^{j2\pi\sqrt{k^2-f_x^2-f_y^2}}\right\} \\ &= \frac{1}{2\pi}\left[\frac{d}{(d^2+x^2+y^2)^{3/2}} - j\frac{kd}{(d^2+x^2+y^2)}\right]e^{jk\sqrt{d^2+x^2+y^2}}, \end{aligned} \tag{2.14}$$

where $\mathcal{F}^{-1}$ denotes the inverse Fourier transform, and $k = 2\pi/\lambda$, the wave number. If an intensity profile is known in plane $(x, y, z = 0)$, then the point-spread function can be used to determine the intensity profile in the plane $(x, y, z = d)$ by a convolution of the $(x, y, 0)$ intensity profile with $h(x, y, d)$.

If $d^2 \gg x^2 + y^2$, then the Huygens-Fresnel point spread function can be simplified:

$$\begin{aligned} h(x,y,d) &\approx \frac{kd}{j2\pi(d^2+x^2+y^2)}e^{jk\sqrt{d^2+x^2+y^2}} \\ &\approx \frac{k}{j2\pi\sqrt{d^2+x^2+y^2}}e^{jk\sqrt{d^2+x^2+y^2}} \\ &\approx \frac{k}{j2\pi d}e^{jk\sqrt{d^2+x^2+y^2}} \end{aligned} \tag{2.15}$$

Consider a plane wave $i(x,y,0)$ propagating in the z direction. At point (x,y,z), the intensity profile is given by

$$i(x,y,z) = \frac{k}{j2\pi z}\int\int i(\xi,\eta,0)e^{jk\sqrt{z^2+(x-\xi)^2+(y-\eta)^2}}d\xi d\eta. \tag{2.16}$$

When $z^2 \gg (x-\xi)^2+(y-\eta)^2$,

$$\begin{aligned} R &= \sqrt{z^2+(x-\xi)^2+(y-\eta)^2} \\ &\approx z\left(1+\frac{1}{2}\frac{(x-\xi)^2+(y-\eta)^2}{z^2}+\cdots\right), \end{aligned} \tag{2.17}$$

by the Fresnel approximation.

By neglecting the high-order terms and substituting (2.17) into (2.16) the intensity simplifies to

$$\begin{aligned} i(x,y,z) &\approx \int\int \frac{k}{j2\pi z}e^{jkz}i(\xi,\eta,0)e^{j\frac{k}{2z}((x-\xi)^2+(y-\eta)^2)} \\ &= \frac{k}{z}e^{jkz}\left[i_0(x,y,0) \ast\ast e^{jk(x^2+y^2)/2z}\right], \end{aligned} \tag{2.18}$$

where $i_0(x,y,0)$ differs from $i(x,y,0)$ by a constant factor and $\ast\ast$ denotes two-dimensional convolution. The quantity $\exp(jk(x^2+y^2)/2z)$ is known as the point-spread function of free space.

Transverse correlation between image pixels arises because diffraction spreads out the interrogating beam, interrogating adjacent tissue regions in addition to the region of interest. The amount of spreading the beam experiences can be calculated by application of (2.18). Consider a transducer which focuses acoustic energy into a circular beam of radius R. Inside the beam, power intensity is constant; outside, it is zero. At depth z, the beam intensity is given by

$$\begin{aligned} i(x,y,z) &= \frac{k}{z}e^{jkz}\int_{x,y} i(\xi,\eta,0)\exp\left(j\frac{k}{2z}((\xi-x)^2+(\eta-y)^2)\right)d\xi d\eta \\ &= \frac{k}{z}e^{jkz}\exp\left(j\frac{k}{2z}(x^2+y^2)\right) \end{aligned}$$

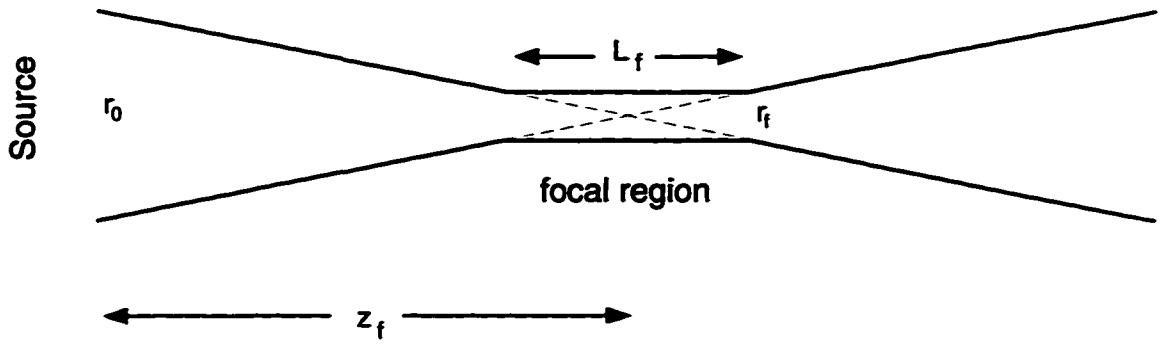

Figure 2.4 Geometric model of the profile of a focused beam.

$$\int_{x,y} i(\xi,\eta,0)\exp\left(-j\frac{k}{2z}(2\xi x+2\eta y-\xi^2-\eta^2)\right)d\xi d\eta \tag{2.19}$$

which in polar coordinates is given by

$$\begin{aligned} i(r,\phi,z) &= \frac{k}{jz}e^{jkz}\int_{\theta=0}^{2\pi}\int_{\rho=0}^{R}\exp\left(-j\frac{k}{2z}(2\rho r\cos\theta\cos\phi+2r\rho\sin\theta\sin\phi)\right) \\ &\qquad \exp\left(j\frac{k}{2z}(\rho^2\cos^2\theta+\rho^2\sin^2\theta)\right)\rho\,d\rho\,d\theta \\ &= \frac{k}{z}e^{jkz}\int_{\theta=0}^{2\pi}\int_{\rho=0}^{R}\exp\left(-j\frac{k}{2z}2\rho r\cos(\theta-\phi)\right)\exp\left(j\frac{k}{2z}\rho^2\right)\rho\,d\rho\,d\theta \\ &= \frac{k}{z}e^{jkz}\int_{\rho=0}^{R}J_0\left(\frac{k\rho r}{z}\right)\exp\left(j\frac{k}{2z}\rho^2\right)\rho\,d\rho. \end{aligned} \tag{2.20}$$

The 3 dB beamwidth at depth z is the largest r for which $i^2(r,\phi,z) < i^2(0,\phi,z)/2$, or equivalently

$$\frac{\left|\int_{\rho=0}^{R}J_0\left(\frac{k\rho r}{z}\right)\exp\left(j\frac{k}{2z}\rho^2\right)\rho\,d\rho\right|^2}{\left|\int_{\rho=0}^{R}\exp\left(j\frac{k}{2z}\rho^2\right)\rho\,d\rho\right|^2} < 1/2. \tag{2.21}$$

This beamwidth has been numerically determined for a realistic range of values of R and k/z, and found to be inversely proportional to both R and k/z. This is in agreement with the beam profile derived for a spherical transducer mounted in a rigid baffle in [7].

In practice, ultrasound beams are focused, or directed inward at the source to produce a narrow beam in a region of the scan plane called the focal region. This allows the system to achieve high lateral resolution in an area of interest at the expense of lateral resolution in other regions. The beam profile as a function of depth is as shown in Figure 2.4. The

beam width at any depth z can be determined geometrically:

$$r(z) = \begin{cases} r_0 - \frac{(r_0 - r_f)z}{z_f - L_f/2} & z < z_f - L_f/2 \\ r_f & z_f - L_f/2 < z < z_f + L_f/2 \\ r_f + \frac{(r_0 - r_f)(z-(z_f+L_f/2))}{z_f + L_f/2} & z < z_f + L_f/2 \end{cases} . \quad (2.22)$$

When the beam reaches a target at depth z, the reflection is characterized as a complex field $\alpha(x, y)$. The reflected wave then travels back towards the transducer, where a diffracted version is received after passing through tissue of thickness z:

$$\begin{aligned} a(x, y, z) &= \frac{1}{\lambda z} e^{jkz} \iint \alpha(\xi, \eta) e^{jk((x-\xi)^2 + (y-\eta)^2)/2z} d\xi d\eta \\ &= \frac{1}{\lambda z} e^{jkz} e^{jk(x^2+y^2)/2z} \iint \alpha(\xi, \eta) e^{-jk(x\xi + y\eta)/z} e^{jk(\xi^2+\eta^2)/2z} d\xi d\eta. \end{aligned} \quad (2.23)$$

The correlation between two points at depth z is given by

$$\begin{aligned} \mathrm{E}\left[a(x_1, y_1, z) a^*(x_2, y_2, z)\right] &= \left(\frac{1}{\lambda z}\right)^2 e^{jk(x_1^2+y_1^2)/2z} e^{-jk(x_2^2+y_2^2)/2z} \\ &\quad \iiint \mathrm{E}\left[\alpha(\xi_1, \eta_1) \alpha^*(\xi_2, \eta_2)\right] e^{-jk(x_1\xi_1 + y_1\eta_1 - x_2\xi_2 - y_2\eta_2)/z} \\ &\quad e^{jk(\xi_1^2 + \eta_1^2 - \xi_2^2 - \eta_2^2)/2z} d\xi_1 d\eta_1 d\xi_2 d\eta_2. \end{aligned} \quad (2.24)$$

Because of the independence of scatterers, prior to diffraction, i.e., at the reflecting surface), the complex field is spatially uncorrelated with itself for any non-zero shift. In other words,

$$\mathrm{E}\left[\alpha(\xi_1, \eta_1) \alpha^*(\xi_2, \eta_2)\right] = \gamma P(\xi_1, \eta_1) P^*(\xi_2, \eta_2) \delta(\xi_1 - \xi_2, \eta_1 - \eta_2), \quad (2.25)$$

where $\delta(\cdot, \cdot)$ denotes a two-dimensional impulse, and $P(\cdot, \cdot)$ is the amplitude of the field at the point of interest, i.e.,

$$|P(x, y)|^2 = \mathrm{E}\left[|\alpha(x, y)|^2\right]. \quad (2.26)$$

Substituting (2.25) into (2.24), we obtain

$$\begin{aligned} \mathrm{E}\left[a(x_1,y_1,z)a^*(x_2,y_2,z)\right] &= \frac{\gamma}{\lambda^2 z^2} e^{jk(x_1^2+y_1^2-x_2^2-y_2^2)/2z} \\ &\quad \int\int |P(\xi,\eta)|^2 e^{-jk\xi(x_1-x2)/z} e^{-jk\eta(y_1-y2)/z} d\xi d\eta. \end{aligned} \tag{2.27}$$

Normalizing so that $\mathrm{E}\left[|a(x,y,z)|^2\right] = 1$, we obtain

$$\begin{aligned} \mathrm{E}\left[a(x_1,y_1,z)a^*(x_2,y_2,z)\right] &= \frac{e^{jk(x_1^2+y_1^2-x_2^2-y_2^2)/2z} \int\int |P(\xi,\eta)|^2 e^{-jk\xi\Delta x/z} e^{-jk\eta\Delta y/z} d\xi d\eta}{\int\int |P(\xi,\eta)|^2 d\xi d\eta} \\ &= e^{jk(x_1^2+y_1^2-x_2^2-y_2^2)/2z} \int\int |P_0(\xi,\eta)|^2 e^{-jk\xi\Delta x/z} e^{-jk\eta\Delta y/z} d\xi d\eta, \end{aligned} \tag{2.28}$$

where

$$P_0(\xi,\eta) = \frac{P(\xi,\eta)}{\sqrt{\int\int |P(x,y)|^2 dx dy}}. \tag{2.29}$$

If $z \gg x^2 + y^2$, the initial exponential term in (2.28) becomes negligible, and the correlation simplifies to

$$\mathrm{E}\left[a(x_1,y_1,z)a^*(x_2,y_2,z)\right] \approx \int\int |P_0(\xi,\eta)|^2 e^{-jk\xi\Delta x/z} e^{-jk\eta\Delta y/z}, \tag{2.30}$$

which is the Fourier transform of the square of the interrogating pulse. If a circular transducer is used to produce a disk-shaped beam intensity profile of radius R at depth z, the correlation in (2.30) is

$$\mathrm{E}\left[a(x,y,z)a^*(x+\Delta x, y+\Delta y, z)\right] = \frac{2\mathrm{J}_1\left(2\pi\frac{R}{\lambda z}\sqrt{(\Delta x)^2+(\Delta y)^2}\right)}{2\pi\frac{R}{\lambda z}\sqrt{(\Delta x)^2+(\Delta y)^2}}, \tag{2.31}$$

where J_1 is a Bessel function of the first kind.

The *interpixel* correlations (as opposed to the correlations between points of the complex field) can be determined by a similar technique involving a bit more algebra:

$$R_{trans}(\Delta x, \Delta y) = \mathrm{E}\left[|a(x,y,z)|^2 |a(x+\Delta x, y+\Delta y, z)|^2\right]$$

$$= \left(\int\int |P(x,y)|^2 dxdy\right)^2 \left(1 + \left(\frac{2\mathrm{J}_1\left(2\pi\frac{R}{\lambda z}\sqrt{(\Delta x)^2+(\Delta y)^2}\right)}{2\pi\frac{R}{\lambda z}\sqrt{(\Delta x)^2+(\Delta y)^2}}\right)^2\right). \tag{2.32}$$

2.3 Higher-Order Moments

Image pixels are obtained by non-coherently detecting the complex Gaussian quantities discussed in the previous sections. Interpixel correlations can be obtained in terms of the parameters of the underlying complex Gaussian field using moment generating functions [8], since expected products of pixel intensities are simply moments of the underlying Gaussian random field. If $i(\cdot,\cdot)$ is the complex field received at the transducer face, and $I(x,y) = |i(x,y)|^2$, then

$$\mathrm{E}\left[I(x,y)I(x+\Delta x, y+\Delta y)\right] = \mathrm{E}\left[i(x,y)i^*(x,y)i(x+\Delta x, y+\Delta y)i^*(x+\Delta x, y+\Delta y)\right], \tag{2.33}$$

which is a moment of the random vector

$$\begin{bmatrix} i(x,y) \\ i(x+\Delta x, y+\Delta y) \\ i^*(x,y) \\ i^*(x+\Delta x, y+\Delta y) \end{bmatrix}. \tag{2.34}$$

If $\mathbf{z}$ is a circular complex Gaussian random vector, and η is formed by concatenating $\mathbf{z}$ and $\mathbf{z}^*$

$$\eta = \begin{bmatrix} \mathbf{z} \\ \mathbf{z}^* \end{bmatrix}, \tag{2.35}$$

it is easy to derive statistical quantities such as (2.33). If complex vector $\mathbf{z}$ has correlation matrix $\mathbb{R} = \mathrm{E}\left[(\mathbf{z}-\mu)(\mathbf{z}-\mu)^H\right]$, where ^{H} denotes conjugate transposition, $\mu = \mathrm{E}[\mathbf{z}]$, and the compound vector η has correlation matrix

$$\Sigma = \begin{bmatrix} \mathbb{O} & \mathbb{R} \\ \mathbb{R} & \mathbb{O} \end{bmatrix}, \tag{2.36}$$

and probability density function

$$f(\eta) = \frac{1}{\pi^n |\mathbb{R}|} \exp\left(-\frac{1}{2}(\eta - \mathbf{h})^T \Sigma^{-1} (\eta - \mathbf{h})\right), \tag{2.37}$$

where $\mathbf{h} = \mathrm{E}[\eta]$, and n is the number of elements in z (half the number in η), and $\mathbb{O}$ denotes the $n \times n$ null matrix.

The moment generating function for this distribution is [8]:

$$\begin{aligned} \Phi(\nu) &= \mathrm{E}\left[\nu^T \eta\right] \\ &= \exp\left(\frac{1}{2}\nu^T \Sigma \nu + \nu^T \mathbf{h}\right). \end{aligned} \tag{2.38}$$

The nth moment of $|z|$ (analogous to (2.33)) is given by

$$\mathrm{E}\left[z_1 z_2 \cdots z_n z_1^* z_2^* \cdots z_n^*\right] = \frac{\partial^{2n}}{\partial \nu_1 \partial \nu_2 \cdots \partial \nu_{2n}} \exp\left(\frac{1}{2}\nu^T \Sigma \nu + \nu^T \mathbf{h}\right)\Big|_{\nu=\mathbf{0}}. \tag{2.39}$$

The moment generating function allows higher-order image statistics to be computed using estimated second-order statistics.

2.4 Estimation of Speckle Moments

The generation of higher order moments from lower order quantities is a potentially valuable tool for researchers seeking to use higher order statistics in tissue characterization. However, researchers often attempt to estimate these moments as in [9, 10], instead of directly calculating them by application of (2.39). These estimates, especially estimates of higher-order moments, generally have a very high variance, as shown in this section.

If $X_i, i = 1, 2, \ldots N$, are N independent realizations of a speckle pattern, the Mth moment of X can be estimated by

$$\theta_M = \frac{1}{N} \sum_{i=1}^{N} X_i^M \tag{2.40}$$

where X_i is obtained from an underlying complex Gaussian random process according to

$$X_i = |n_c + \mu|^2, \tag{2.41}$$

n_c is zero mean, complex Gaussian with independent and identically distributed real and imaginary parts, and μ is the strength of the coherent reflection present. This corresponds to the intensity of a speckle image, not the magnitude as is often displayed in ultrasound imaging. The expected value of θ_M is

$$\begin{aligned} \mathrm{E}[\theta_M] &= \frac{1}{N}\mathrm{E}\left[\sum_{i=1}^{N} X_i^M\right] \\ &= \frac{1}{N}\sum_{i=1}^{N}\mathrm{E}\left[|n_c+\mu|^{2M}\right] \\ &= \mathrm{E}\left[|n_c+\mu|^{2M}\right]. \end{aligned} \tag{2.42}$$

Thus θ_M is an unbiased estimator of X^M.

The expected value of θ_M can be evaluated by noting that

$$\begin{aligned} \mathrm{E}\left[|n_c+\mu|^{2M}\right] &= \mathrm{E}\left[((n_c+\mu)(n_c+\mu)^*)^M\right] \\ &= \sum_{k=0}^{M}\binom{M}{k}^2 \mathrm{E}\left[|n_c|^{2k}\right]|\mu|^{2M-2k}, \end{aligned} \tag{2.43}$$

where

$$\binom{M}{k} = \frac{M!}{k!(M-k)!}. \tag{2.44}$$

By application of the moment generating function (2.39),

$$\mathrm{E}\left[|n_c|^{2k}\right] = \sigma^{2k}, \tag{2.45}$$

where

$$\begin{aligned} \sigma^2 &= \mathrm{E}\left[|n_c|^2\right] \\ &= 2\mathrm{E}\left[\mathrm{Real}[n_c]\right] = 2\mathrm{E}\left[\mathrm{Imag}[n_c]\right]. \end{aligned} \tag{2.46}$$

Thus,

$$\mathrm{E}\left[\theta_M\right] = \sum_{k=0}^{M} \binom{M}{k}^2 \sigma^{2k} |\mu|^{2M-2k}. \tag{2.47}$$

The variance of θ_M can be similarly evaluated:

$$\begin{aligned}
\mathrm{E}\left[(\theta_M - \mathrm{E}[\theta_M])^2\right] &= \mathrm{E}\left[\theta_M^2\right] - \mathrm{E}[\theta_M]^2 \\
&= \mathrm{E}\left[\left(\frac{1}{N}\sum_{i=1}^{N} |n_c + \mu|^{2M}\right)^2\right] - \mathrm{E}[\theta_M]^2 \\
&= \frac{1}{N^2}\sum_{i=1}^{N}\sum_{j=1}^{N} \mathrm{E}\left[|n_c^i + \mu|^{2M} |n_c^j + \mu|^{2M}\right] - \mathrm{E}[\theta_M]^2 \\
&= \frac{1}{N^2}\sum_{i=1}^{N}\sum_{j\neq i} \mathrm{E}\left[|n_c^i + \mu|^{2M}\right] \mathrm{E}\left[|n_c^j + \mu|^{2M}\right] \\
&\qquad + \frac{1}{N}\sum_{i=1}^{N} \mathrm{E}\left[|n_c^i + \mu|^{4M}\right] - \mathrm{E}\left[|n_c + \mu|^{2M}\right]^2 \\
&= \frac{1}{N^2}\sum_{i=1}^{N}\sum_{j\neq i} \mathrm{E}\left[|n_c^i + \mu|^{2M}\right]^2 - \mathrm{E}\left[|n_c + \mu|^{2M}\right]^2 \\
&\qquad + \frac{1}{N}\sum_{i=1}^{N} \mathrm{E}\left[|n_c^i + \mu|^{4M}\right] \\
&= \left(\frac{N(N-1)}{N^2} - 1\right) \mathrm{E}\left[|n_c + \mu|^{2M}\right]^2 + \frac{1}{N}\mathrm{E}\left[|n_c + \mu|^{4M}\right] \\
&= \frac{1}{N}\left\{\mathrm{E}\left[|n_c + \mu|^{4M}\right] - \mathrm{E}\left[|n_c + \mu|^{2M}\right]^2\right\},
\end{aligned} \tag{2.48}$$

which can be evaluated by application of (2.45) and (2.43). Note that as the number of independent observations grows large, the variance of the estimate becomes small; θ_M is a *consistent* estimator of X^M.

2.5 The K-Distribution

Typically, statistical treatments of ultrasonic speckle involve assumptions such as those made here: that each resolution cell contains a large number of scatterers, and that the scatterers' positions and scattering strengths are independent of each other.

This results in a Rayleigh or Rician distribution of pixel magnitudes. These assumptions are seldom met exactly, however, especially in abnormal or diseased tissue, where the deviation of the scattering parameters from ideal values has been considered characteristic of abnormality.

A more general distribution function known as the K-distribution has been recently borrowed from the radar scattering literature, where it was first proposed in the mid 1970s [11, 12, 13]. The K-distribution has been been proposed for ultrasound analysis because it couples the true number of scatterers to their scattering cross section to produce an "effective" number of scatterers. It has been conjectured that the effective number of scatterers can be an indicator of diseased tissue [10].

The K-distribution is derived as follows [11]. Consider a received signal

$$E(r,t) = \mathrm{Re}\left[e^{j\omega t}\sum_{i=1}^{N} a_i(r,t)e^{j\phi_i(r,t)}\right], \tag{2.49}$$

equivalent to an un-demodulated form of (2.2). Here, $a_i(r,t)$ and $\phi_i(r,t)$ are the magnitude and phase received at time t on the rth scan line. The characteristic function of E is given by

$$\begin{aligned} C(U) &= \mathrm{E}\left[e^{jUE}\right] \\ &= \mathrm{E}\left[\exp\left(jU\mathrm{Re}\left[e^{j\omega t}\sum_{i=1}^{N} a_i e^{j\phi_i}\right]\right)\right] \\ &= \prod_{i=1}^{N}\mathrm{E}\left[\exp\left(jUa_i\mathrm{Re}\left[e^{j\omega t}e^{j\phi_i}\right]\right)\right] \\ &= \prod_{i=1}^{N}\mathrm{E}\left[\exp\left(j|U|a_i\cos(\omega t+\phi_i+\phi)\right)\right] \\ &= \prod_{i=1}^{N}\mathrm{E}\left[J_0(|U|a_i)\right], \end{aligned} \tag{2.50}$$

in which the independence of all a_i and ϕ_i is used to pull the sum outside the exponential function in the third step, and to perform the expectation with respect to ϕ separate from that with respect to a_i in the last step. If the scattering strengths a_i are identically

distributed, (2.50) simplifies to

$$C(U) = \mathrm{E}\left[J_0(|U|a)\right]^N . \tag{2.51}$$

The K-distribution arises if we assume that the a are distributed according to

$$p(a) = \frac{2b}{\Gamma(1+\nu)}\left(\frac{ba}{2}\right)^{\nu+1} K_\nu(ba), \tag{2.52}$$

where b and ν are functions of the viewing position, and K_ν is a modified Bessel function of the second kind of order ν. This distribution function was first derived by assuming the radar return from a single "patch" of sea surface to be a product of two random quantities, one negative exponentially distributed (related to the overall properties of the patch) and the other (corresponding to the patch's "tilt") distributed as a Chi-square variate of order $2(\nu-1)$ [11]. More importantly, however, (2.52) leads to a tractable form for the distribution of $|E|^2$.

Assuming (2.52), the characteristic function of E reduces to

$$\begin{aligned} C(U) &= \mathrm{E}\left[J_0(|U|a)\right]^N \\ &= \left(\frac{b^2}{b^2+|U|^2}\right)^M \end{aligned} \tag{2.53}$$

where $M = N(\nu+1)$, and the distribution of $I = |E|^2$ is given by

$$p(I) = \frac{b/\sqrt{I}}{\Gamma(M)}\left(\frac{b/\sqrt{I}}{2}\right) K_{M-1}(b\sqrt{I}). \tag{2.54}$$

This distribution has come to be applied to ultrasound statistics because the quantity $M = N(\nu+1)$ can be loosely interpreted as an effective number of scatterers, dependent not only on their true numbers, but also on their scattering cross sections. In the limit of large M, the K-distribution can be shown to approach familiar Rayleigh, Rician, Gaussian and log-normal distributions.

2.6 Conclusion

This chapter has dealt with statistical properties of ultrasound speckle. First and second order statistics have been derived from a physical model for the scattering process, and a technique has been proposed to generate higher-order moments. The K-distribution is also described as a more general distribution function which may have a role in analysis of the statistics of backscatter from diseased or abnormal media.

CHAPTER 3

LINE AND BOUNDARY DETECTION IN SPECKLE IMAGES

3.1 Line and Boundary Detection

The problem of detecting linear features in an image computed by coherent acoustical, radar or laser illumination is of interest because these features may contain important information. For example, in synthetic aperture radar (SAR) scenery, it may be known *a priori* that roads travel along straight lines. Similarly, medical ultrasound systems display tissue boundaries as broad curves that appear as straight line segments if observed at a sufficiently small scale [14]. The detection of these features may be an essential first step in segmenting an image for reconnaissance or diagnostic purposes.

Feature detection in acoustical or SAR imagery is a challenging problem because of the presence of speckle noise. The physical mechanism of laser speckle, common to all forms of coherent imaging speckle, was surveyed by Goodman [2]. The statistical treatment in [2] was adapted by Burckhardt [3] and Wagner et al. [15] to better describe the statistics of ultrasound speckle. Later, Wagner et al. [4] introduced the concept of correlation length to describe the distance over which image pixels show statistical correlation, in terms of imaging parameters such as frequency of interrogation and transducer array size.

Even though speckle can be treated statistically, and is often said to "corrupt" an image, it is important to note that speckle is not noise in the sense in which engineers often use the term. In SAR imaging, for instance, Munson and Sanz [16] showed that speckle is *necessary* to be able to form an image at all. In medical ultrasonics, it is widely believed that the speckle "texture" conveys information about the region being imaged, although the exact method of interpreting that information is in dispute [10, 17].

A few authors have proposed processing schemes motivated by statistical considerations, notably Kuan et al. [18], who derive adaptive techniques for the restoration of speckle imagery, and Donohue [19], who computes the maximum likelihood estimator for coherently reflecting targets from A-mode ultrasound backscatter, enabling statistical detection of targets in raw RF data.

Other processing schemes make simplified assumptions on the speckle statistics to develop useful processing techniques. A survey of some of these techniques is given by [20]. Bovik and Munson [21], Bovik [22], and Donohue et al. [23] assumed a multiplicative model for speckle to produce useful techniques for edge detection, in spite of flaws in the multiplicative noise model [24]. The result in [22] is arguably the state of the art in detecting step discontinuities in speckle imagery; however, none of these techniques consider second or higher-order speckle statistics in the development of processing techniques.

This thesis represents a comprehensive study of detection methods in speckle noise. In particular, in this chapter, we discuss the optimal and near optimal detection of lines. We also describe a suboptimal approach, similar in principle to the Hough transform [25], which works well when the speckle field is uncorrelated, and which offers reasonable performance at low computational complexity in colored noise. We also find that theoretically, the performance of this technique can be significantly improved by "prewhitening" the speckle field.

A related technique has been in use in pattern recognition by Lee and Rhodes [26, 27, 28, 29] and by Hou and Bamberger [30, 31]. Our own work is the first use of this idea in medical imaging [14, 32], and includes a strong argument for the near optimality of this approach, at least in the case of ultrasound speckle, which is lacking in [26, 27, 28, 29, 30, 31].

3.2 Detection in Speckle

In this chapter, the problem of detecting lines in images is broken down into a simpler problem, that of determining whether or not a line passes through each pixel. We consider a neighborhood around each pixel and search for lines passing through the center of that neighborhood. This is an M-ary hypothesis testing problem, where each of the hypotheses

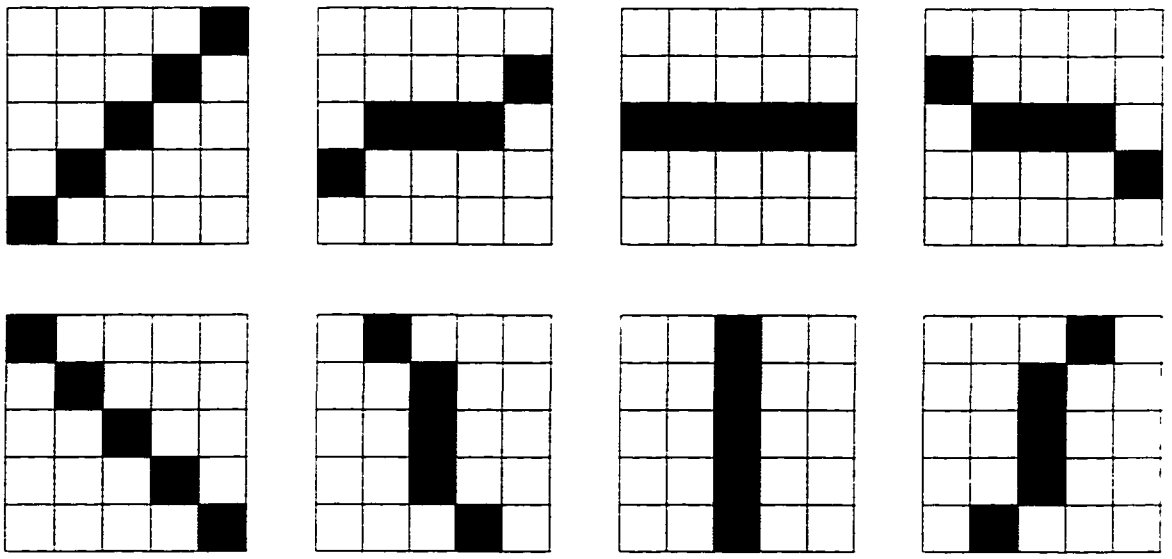

Figure 3.1 Orientations of a length 5 stick. Each of these orientations represents a hypothesis to evaluate at each pixel.

represents a possible line orientation. More general M-ary detection problems can be considered by substituting a different set of hypotheses for the straight-line segments considered here.

For simplicity, we take the neighborhood to be an $N \times N$ square region, and the number of possible orientations, equal to the number of hypotheses, to scale linearly with N. We refer to the set of lines as "sticks" because although they are long compared with the correlation length of the speckle field, they are short on the scale of the features of interest; in a sense, large-scale linear features are "built up" of sticks at different locations and orientations. Figure 3.1 shows a set of sticks of length 5.

In the subsections which follow, several different detection strategies are discussed. In each case, except for the rotating kernel transformations, the desired test is performed by comparing the maximum test statistic value at each point to a threshold. For the rotating kernel transformations, the test is implemented by subtracting the minimum test statistic from the maximum test statistic and comparing the result to a threshold.

3.2.1 Optimal detection

Optimal M-ary hypothesis testing is accomplished by selecting the hypothesis that maximizes the likelihood ratio function [33]

$$\Lambda_i(\mathbf{x}) = \frac{P[\mathbf{x}|H_i]}{P[\mathbf{x}|H_0]}, \tag{3.1}$$

where the signal vector $\mathbf{x}$ is a set of image points in a neighborhood, and the ith hypothesis H_i represents the ith orientation straight line passing through the center of the neighborhood.

The likelihood ratio function is the ratio of the probability density of a particular realization $\mathbf{x}$ under hypothesis i (H_i) to its probability density under the null hypothesis (H_0). In the stick detection problem, we wish to distinguish between the null hypothesis H_0 and hypotheses H_1 through H_M, each of which corresponds to the presence of a straight line. The different hypotheses are characterized statistically by

$$H_i : \mathbf{x} = |\mathbf{n}_c + \mu^{(i)}|^2 \tag{3.2}$$

$$H_0 : \mathbf{x} = |\mathbf{n}_c|^2, \tag{3.3}$$

where $\mathbf{n}_c = \mathbf{a} + j\,\mathbf{b}$ is a zero mean complex Gaussian random vector whose real and imaginary parts are Gaussian, independent, and identically distributed, and $\mu^{(i)}$ is the stick at the ith orientation. This corresponds to the case of specular reflection of sound from the boundary.

Note that we have "unrolled" the square $N \times N$ image regions into $N^2 \times 1$ vectors for ease of manipulation. This is done without loss of generality since all the spatial correlations of the two-dimensional discrete Gaussian random field can be expressed in a correlation matrix. Note also that we will be performing the hypothesis test on the *squared* magnitude of the image rather than on the magnitude. This invertible transformation is done to simplify computation.

The probability density function (pdf) of the signal vector $\mathbf{x}$ under hypothesis i can be computed from the underlying normal distribution on the constituents of $\mathbf{x}$:

$$\begin{aligned}
p_{\mathbf{X}}[\mathbf{x}|H_i] &= \lim_{\underline{\delta}\to 0} \frac{1}{\prod_j 2\delta_j} P\left[\mathbf{x}-\underline{\delta} \le X \le \mathbf{x}+\underline{\delta}\right] \\
&= \lim_{\underline{\delta}\to 0} \frac{1}{\prod_j 2\delta_j} P\left[\mathbf{x}-\underline{\delta} \le (\mathbf{a}+\underline{\mu}^{(i)})^2+\mathbf{b}^2 \le \mathbf{x}+\underline{\delta}\right] \\
&= \int_{-\infty}^{\infty} p_{\mathbf{B}}(\mathbf{b}) \lim_{\underline{\delta}\to 0} \frac{1}{\prod_j 2\delta_j} \left\{ P\left[\sqrt{\mathbf{x}-\underline{\delta}-\mathbf{b}^2}-\underline{\mu}^{(i)} \le \mathbf{a} \le \sqrt{\mathbf{x}+\underline{\delta}-\mathbf{b}^2}-\underline{\mu}^{(i)}\right] \right. \\
&\qquad \left. + P\left[\sqrt{\mathbf{x}-\underline{\delta}-\mathbf{b}^2}-\underline{\mu}^{(i)} \le \mathbf{a} \le \sqrt{\mathbf{x}+\underline{\delta}-\mathbf{b}^2}+\underline{\mu}^{(i)}\right] \right\} d\mathbf{b} \\
&= \int_{-\infty}^{\infty} p_{\mathbf{B}}(\mathbf{b}) \frac{1}{\prod_j \sqrt{x_j-b_j^2}} \\
&\qquad \left\{ p_{\mathbf{A}}\left(\sqrt{\mathbf{x}-\mathbf{b}^2}-\underline{\mu}^{(i)}\right) + p_{\mathbf{A}}\left(\sqrt{\mathbf{x}-\mathbf{b}^2}+\underline{\mu}^{(i)}\right) \right\} d\mathbf{b}, \qquad (3.4)
\end{aligned}$$

expressed in terms of an integral over $\mathbf{b}$, a nuisance parameter with known Gaussian distribution. Note that in (3.4), the vector square roots are applied to each element, and the notation $P[\mathbf{x} \le \mathbf{X} \le \mathbf{y}]$ indicates the probability that a scalar inequality is true for every element of vectors $\mathbf{x}$, $\mathbf{X}$, and $\mathbf{y}$.

The pdf under the null hypothesis is obtained from (3.4) by setting $\underline{\mu}$ to the zero vector:

$$p_{\mathbf{X}}[\mathbf{x}|H_0] = \int_{-\infty}^{\infty} p_{\mathbf{B}}(\mathbf{b}) \frac{2}{\prod_j \sqrt{x_j-b_j^2}} p_{\mathbf{A}}\left(\sqrt{\mathbf{x}-\mathbf{b}^2}\right) d\mathbf{b}. \qquad (3.5)$$

The likelihood ratio function for each hypothesis is thus the ratio of two N^2-dimensional integrals, where N is the length of the stick. The most probable hypothesis for any given image region is the hypothesis that maximizes the likelihood ratio function. If all the likelihood ratio functions are less than some threshold, then the null hypothesis should be selected. Thus the optimal stick detection scheme is to evaluate a family of integrals for each point, compute the maximum result and compare to a threshold.

The true likelihood ratio function has tremendous computational complexity (on the order of $N^4 q^{N^2}$ multiplications per hypothesis by Gaussian quadrature integration, where N is the stick length) to evaluate because of all the interpixel correlations that make (3.4)

and (3.5) iterated integrals rather than products of one-dimensional integrals. However, if the speckle is known to have uncorrelated pixels, optimal detection can be performed at more modest cost.

A speckle field tends to decorrelate spatially rather quickly, so one way of dealing with speckle is to decimate the image to the point where the interpixel correlations are insignificant. In this case, the speckle field can be modeled as the magnitude squared of a white Gaussian field. Thus, the pixels are independent, and the problem reduces to a multidimensional Rayleigh/Rician detection problem, well-known in non-coherent communications [34]. Note that it is the *magnitude* (not magnitude squared) of a Gaussian random variable that has a Rayleigh or Rician distribution. Thus, the likelihood ratio below is expressed in terms of $\sqrt{\mathbf{x}}$, where $\mathbf{x}$ is the square of the image pixels, consistent with the definition above.

For white speckle noise [34], the likelihood function is given by

$$\Lambda_i(\mathbf{x}) = \prod_j \exp\left(-\frac{\mu_j^{(i)}}{2\sigma^2}\right) \mathrm{I}_0\left(\frac{1}{\sigma^2}\sqrt{\mathbf{x}_j \left|\mu_j^{(i)}\right|^2}\right), \tag{3.6}$$

where $\mathrm{I}_0(\cdot)$ is a modified Bessel function, $\sigma^2 = E_0[\mathbf{x}_i]$, and $\mu_j^{(i)}$ is the jth component of the stick at the ith orientation. Collecting terms, we obtain

$$\begin{aligned} \Lambda_i(\mathbf{x}) &= \exp\left(\sum_j -\frac{\mu_j^{(i)}}{2\sigma^2}\right) \prod_j \mathrm{I}_0\left(\frac{1}{\sigma^2}\sqrt{\mathbf{x}_j \left|\mu_j^{(i)}\right|^2}\right) \\ &= K \prod_j \mathrm{I}_0\left(\frac{1}{\sigma^2}\sqrt{\mathbf{x}_j \left|\mu_j^{(i)}\right|^2}\right), \end{aligned} \tag{3.7}$$

where K is a constant with respect to $\mathbf{x}$ which can be incorporated into the threshold.

3.2.2 Quadratic detection

The optimal detector in the colored noise case is prohibitively expensive to implement. Even in the case of uncorrelated speckle, optimal detection requires the evaluation of a set of Bessel functions for each image point. Thus, a suboptimal detection rule may be

desirable for detection in colored noise if it offers reasonable performance at significant computational savings.

We now center our attention on the class of linear-quadratic detectors, since they are much simpler computationally than the optimal colored-noise detectors, require no special function evaluations, and can offer high performance. One well-known technique for designing linear-quadratic detectors is to use the deflection criterion. Historically, deflection was first used to design optimal linear-quadratic systems for detecting Gaussian signals in Gaussian noise [35]. However, the approach of Picinbono and Duvaut [36] allows the technique to be generalized to the case of arbitrarily distributed noise, provided certain noise statistics are known.

A linear-quadratic test statistic has the form

$$S_\alpha(\mathbf{x}) = \mathbf{x}^T\mathbf{M}_\alpha\mathbf{x} + \mathbf{h}_\alpha^T\mathbf{x} + \mathrm{tr}(\mathbf{C}\mathbf{M}_\alpha), \tag{3.8}$$

where $\mathbf{C} = \mathrm{E}[\mathbf{x}\mathbf{x}^T]$, and the trace term is included to ensure that $S(\mathbf{x}) = 0$ under the null hypothesis. The subscript α is used to denote a particular hypothesis. The deflection-optimal linear-quadratic detection rule has the form of (3.8), and uses values of $\mathbf{h}$ and $\mathbf{M}$ which maximize deflection $D(S)$:

$$D(S) = \frac{(\mathrm{E}_1[S])^2}{\mathrm{E}_0[S^2]}. \tag{3.9}$$

For Gaussian signals in Gaussian noise, $D(S)$ is a signal to noise ratio; in non-Gaussian detection problems, it is globally maximized by the likelihood ratio [36]. In the case of speckle, a linear-quadratic test can not be globally optimal. It may, however, offer a computationally tractable suboptimal solution.

Picinbono and Duvaut [36] showed that the deflection optimal $\mathbf{h}_\alpha$ and $\mathbf{M}_\alpha$ can be obtained by solving the following linear equations simultaneously:

$$s_\alpha(i) = \sum_k C(i,k)h_\alpha(k) + \sum_{k,l} B(i,k,l)M_\alpha(k,l) \tag{3.10}$$

$$\Gamma_\alpha(i,j) = \sum_k B(i,j,k)h_\alpha(k) + \sum_{k,l} A(i,j,k,l)M_\alpha(k,l) \tag{3.11}$$

where

$$\begin{aligned}
\mathrm{E}_0[\mathbf{x}] &= \mathbf{0} && (3.12)\\
\mathrm{E}_\alpha[\mathbf{x}] &= \mathbf{s}_\alpha && (3.13)\\
\mathrm{E}_0[\mathbf{x}\mathbf{x}^T] &= \mathbf{C} && (3.14)\\
\mathrm{E}_\alpha[\mathbf{x}\mathbf{x}^T] &= \Gamma_\alpha + \mathbf{C} && (3.15)\\
\mathrm{E}_0[x_i x_j x_k] &= B(i,k,l) && (3.16)\\
\mathrm{E}_0[x_i x_j x_k x_l] &= A(i,j,k,l) + C(i,j)C(k,l). && (3.17)
\end{aligned}$$

These statistics can be calculated using the moment generating function (2.39). Note that since speckle patterns are strictly positive, the mean under the null hypothesis

$$\begin{aligned}
\mathrm{E}_0[\mathbf{x}] &= \mathrm{E}[|\mathbf{a}|^2]\\
&= \mathrm{E}[\mathrm{Re}(\mathbf{a})^2 + \mathrm{Im}(\mathbf{a})^2]\\
&= \begin{bmatrix}\sigma^2 & \sigma^2 & \cdots & \sigma^2\end{bmatrix}^T && (3.18)
\end{aligned}$$

must be subtracted from the observation so that Equation (3.12) holds. We define $\mathbf{y} = \mathbf{x} - [\sigma^2 \ \cdots \ \sigma^2]^T$, and derive the moments above for $\mathbf{y}$ instead of $\mathbf{x}$.

Without lengthy derivation, we calculate

$$\begin{aligned}
\mathrm{E}_0[\mathbf{y}] &= \mathbf{0} && (3.19)\\
\mathrm{E}_\alpha[\mathbf{y}] &= \left|\mu^{(\alpha)}\right|^2 && (3.20)\\
\mathrm{E}_0[y_i y_j] &= \sigma^4 \rho_{ij}^2 && (3.21)\\
\mathrm{E}_\alpha[y_i y_j] &= \sigma^4 \rho_{ij}^2 + \left|\mu_i^{(\alpha)}\right|^2 \left|\mu_j^{(\alpha)}\right|^2 && (3.22)\\
\mathrm{E}_0[y_i y_j y_k] &= 2\sigma^6 \rho_{ij}\rho_{jk}\rho_{ik} && (3.23)\\
\mathrm{E}_0[y_i y_j y_k y_l] &= \sigma^8\Big(\rho_{il}^2\rho_{jk}^2 + \rho_{ij}^2\rho_{kl}^2 + \rho_{ik}^2\rho_{jl}^2 + 2\rho_{ik}\rho_{il}\rho_{jk}\rho_{jl}\\
&\qquad + 2\rho_{ij}\rho_{il}\rho_{jk}\rho_{kl} + 2\rho_{ij}\rho_{ik}\rho_{jl}\rho_{kl}\Big) && (3.24)
\end{aligned}$$

where $\mu_i^{(\alpha)}$ is the ith element of the α orientation stick, and ρ_{ij} is the "correlation coefficient" between two points in the complex speckle pattern, taking on values between -1

and 1:

$$\mathrm{E}[a_i a_j^*] = \mathrm{E}[a_i^* a_j] = \sigma^2 \rho_{ij}. \tag{3.25}$$

Since the detector coefficients $\mathbf{h}_\alpha$ and $\mathbf{M}_\alpha$ derived from the statistics computed in (3.19) through (3.24) are in terms of $\mathbf{y} = \mathbf{x} - [\sigma^2 \ \cdots \ \sigma^2]^T$ instead of $\mathbf{x}$, the deflection-optimal detector has the form

$$S_\alpha(\mathbf{x}) = \mathbf{x}^T \mathbf{M}_\alpha \mathbf{x} + \left(\mathbf{h}_\alpha - 2\mathbf{M}_\alpha \begin{bmatrix} \sigma^2 \\ \vdots \\ \sigma^2 \end{bmatrix} \right)^T \mathbf{x} + \mathrm{tr}\left(\left\{ \mathbf{C} + \sigma^4 \begin{bmatrix} 1 & 1 & \cdots & 1 \\ 1 & 1 & \cdots & 1 \\ \vdots & \vdots & \ddots & \vdots \\ 1 & 1 & \cdots & 1 \end{bmatrix} \right\} \mathbf{M}_\alpha \right). \tag{3.26}$$

3.2.3 Generalized likelihood ratio detection

In many cases where a likelihood ratio test is intractable, a computationally simpler *generalized likelihood ratio test* (GLRT) can be used instead The GLRT is the ratio of active to null hypothesis conditional pdfs, conditioned on maximum likelihood estimates of which active and null hypotheses are present [37]. Mathematically, the GLRT is written

$$\Lambda(\mathbf{x}) = \frac{\max_\theta p_1(x|\theta)}{\max_\theta p_0(x|\theta)}, \tag{3.27}$$

where $p_1(x|\theta)$ and $p_0(x|\theta)$ are conditional active and null hypothesis pdfs. A significant advantage of the GLRT is its ability to deal with unknown parameters.

In this subsection, we compute the GLRT for a stick of unknown amplitude in additive colored Gaussian speckle. Like the deflection criterion, this method may provide a useful technique in spite of unrealistic assumptions on the noise statistics. The signal model is the following:

$$H_i : \mathbf{x} = \mathbf{n} + \beta \underline{\mu}^{(i)} \tag{3.28}$$

$$H_0 : \mathbf{x} = \mathbf{n}, \tag{3.29}$$

where n is a colored Gaussian random vector, μ_i is the unit magnitude stick of orientation i, and β is a positive quantity denoting the unknown magnitude of the stick.

The GLRT is

$$\begin{aligned}
\Lambda(\mathbf{x}) &= \frac{\max_{i,\beta} p_1(\mathbf{x}|i,\beta)}{\max_i p_0(\mathbf{x}|i)} \\
&= \frac{\max_{i,\beta} \exp\left(-\frac{1}{2}(\mathbf{x}-\beta\underline{\mu}_i)^T\Sigma^{-1}(\mathbf{x}-\beta\underline{\mu}_i)\right)}{\exp\left(-\frac{1}{2}\mathbf{x}^T\Sigma^{-1}\mathbf{x}\right)} \\
&= \max_{i,\beta} \exp\left(\frac{1}{2}\mathbf{x}^T\Sigma^{-1}\mathbf{x} - \frac{1}{2}(\mathbf{x}-\beta\underline{\mu}_i)^T\Sigma^{-1}(\mathbf{x}-\beta\underline{\mu}_i)\right) \\
&= \max_{i,\beta} \exp\left(\beta\underline{\mu}_i^T\Sigma^{-1}\mathbf{x} - \frac{1}{2}\beta^2\underline{\mu}_i^T\Sigma^{-1}\underline{\mu}_i\right). \qquad (3.30)
\end{aligned}$$

Since i is a discrete valued parameter (the index into a family of sticks), we maximize first with respect to β; the maximum occurs when

$$\beta = \frac{\underline{\mu}_i^T\Sigma^{-1}\mathbf{x}}{\underline{\mu}_i^T\Sigma^{-1}\underline{\mu}_i}. \qquad (3.31)$$

Because the exponential is a monotonically increasing function, we can implement an equivalent GLRT by thresholding only its argument; thus, the GLRT is

$$\Lambda(\mathbf{x}) = \max_i \frac{\left(\underline{\mu}_i^T\Sigma^{-1}\mathbf{x}\right)^2}{2\underline{\mu}_i^T\Sigma^{-1}\underline{\mu}_i}. \qquad (3.32)$$

Note that we have assumed that $\beta > 0$; however, it is possible for negative values to occur. Since Σ^{-1} is a positive semi-definite correlation matrix, $\beta < 0$ implies that $\underline{\mu}_i^T\Sigma^{-1}\mathbf{x} < 0$. We will treat this as an error condition implying that no signal is present at that orientation.

With this assumption, the GLRT can be implemented as

$$\max_i K(i)\underline{\mu}_i^T\Sigma^{-1}\mathbf{x}, \qquad (3.33)$$

where

$$K(i) = \frac{1}{\sqrt{2\underline{\mu}_i^T\Sigma^{-1}\underline{\mu}_i}}. \qquad (3.34)$$

If the noise is circularly distributed, $K(i)$ is constant with respect to i, and can be neglected, leading to a particularly simple linear test.

3.2.4 Linear detection

3.2.4.1 Sticks

If the noise is assumed to be white, (3.33) reduces to a simple linear projection operation. At each point, the detection statistic is produced by adding all the pixel intensities falling along a stick of one orientation and maximizing the sum over all possible stick rotations:

$$\Lambda(\mathbf{x}) = \max_i \underline{\mu}_i^T \mathbf{x}. \tag{3.35}$$

Although speckle is neither additive, Gaussian nor white, we have found the "Sticks" technique to be useful for detection of linear components as well as for image enhancement [14, 32].

3.2.4.2 Pre-whitened matched filtering

Although the Sticks technique has yielded useful results, it is based on highly faulty assumptions, particularly that the speckle is Gaussian and uncorrelated. A more sophisticated linear detection rule can be constructed by "prewhitening" the image to remove the interpixel correlations, and then applying a matched filter. The prewhitening filter is implemented by retaining the Σ^{-1} term in (3.33) but assuming $K(i)$ from (3.34) is constant with respect to i:

$$\Lambda(\mathbf{x}) = \max_i \underline{\mu}_i^T \Sigma^{-1} \mathbf{x}. \tag{3.36}$$

where

$$\mathbf{\Sigma} = \mathrm{E}_\alpha \left[\left(\mathbf{x} - \mu_{(\alpha)} \right) \left(\mathbf{x} - \mu_{(\alpha)} \right)^T \right] \tag{3.37}$$

This can be evaluated element-wise by application of the statistics calculated in (3.19) through (3.24):

$$\{\mathbf{\Sigma}\}_{ij} = \sigma^4 \rho_{ij}^2. \tag{3.38}$$

Note that the correlation expression in (3.38) is independent of the presence or absence of a line. The prewhitening operation assumes the noise has Gaussian distribution with mean and covariance calculated by the moment generating function, applies a whitening

filter to the observation, then applies a matched filter. The technique is still suboptimal since speckle does not have a Gaussian distribution.

3.2.5 Rotating kernel transformations

The use of rotating kernel transformations, introduced by Lee and Rhodes [26, 27, 28, 29] for pattern recognition and enhancement of linear features, represents a generalization of the Sticks technique. The transformations involve the convolution of the original image with a long narrow operator at various orientations. The convolutions produce a set of output values for each pixel; the enhanced image is computed pointwise as a function of the output values at each point. Until the present work, the use of these techniques has been statistically uncharacterized. In each of the rotating kernel transformations, a new image point $I(x, y)$ is obtained from the original image i by some combination of the results of a set of angle-dependent filter outputs:

$$I(x,y) = g\left(\sum_k \sum_l f_\theta(x-k, y-l) i(k,l)\right). \tag{3.39}$$

The choice of $f_\theta(x, y)$ and $g(h(\theta))$ in (3.39) distinguishes the transformations. Table 3.1 summarizes a few of these algorithms.

Lee and Rhodes [26, 27, 28, 29] proposed a "rotating kernel min-max transformation" (RKMT) similar to Sticks, except that the detection statistic is the arithmetic difference between the largest and smallest stick projections, instead of the maximum. This technique may offer better performance when the original image has varying degrees of brightness at different points of the image, or a varying signal-to-noise ratio. A tapering function can be used with the RKMT by applying a taper to the stick instead of using a rectangular contour. This is a potentially useful means of matching the operator to the line profile when the target has significant curvature; along the support of the stick, the target may have a tapered profile more exactly matched by a tapered stick. Rectangular, Gaussian and triangular tapering functions are compared in Section 3.3.3.

Table 3.1 Summary of Rotating Kernel Transformations

Operator	$f_\theta(x,y)$	$g(h(\theta))$
Sticks	$\begin{cases} 1 & \text{if } \lvert x\rvert \le \frac{N}{2}, \text{ and } y = 0 \\ 0 & \text{otherwise} \end{cases}$	$\max_\theta h(\theta)$
RKMT	$\begin{cases} 1 & \text{if } \lvert x\rvert \le \frac{N}{2}, \text{ and } y = 0 \\ 0 & \text{otherwise} \end{cases}$	$\max_\theta h(\theta) - \min_\theta h(\theta)$
RKMT with triangular contour	$\begin{cases} 1 - \frac{\lvert x\rvert}{T} & \text{if } y = 0 \text{ and } \lvert x\rvert < T \\ 0 & \text{otherwise} \end{cases}$	$\max_\theta h(\theta) - \min_\theta h(\theta)$
RKMT with Gaussian contour	$\begin{cases} e^{-\alpha x^2} & \text{if } y = 0 \\ 0 & \text{otherwise} \end{cases}$	$\max_\theta h(\theta) - \min_\theta h(\theta)$

3.2.6 Other operators

The number of potential line detection operators is virtually unlimited. For example, we have experimented with the use of a median operation in place of the line sum used by Sticks [38], and with estimating the prior probabilities of each line orientation to help in detection [39]. At this time, we will defer analysis of these techniques, and simply comment that they illustrate the variety of related techniques that can be developed. A comparison of techniques showing their performance in processing real images will be presented in Chapter 4.

3.3 Comparison of Results

This section presents a comparison of the techniques described above by way of *Monte Carlo* simulation. In each case, the detector performance is summarized in a receiver operating characteristic (ROC) curve, in which the probability of correctly detecting a line segment (P_D) is plotted versus the probability of falsely detecting a segment when none is present (P_{FA}). The threshold is a parameter that increases along the ROC curve with increasing values of P_{FA}. More powerful detectors have higher ROC curves (i.e.,

for a given false alarm probability, they yield a higher probability of correct detection). For cases in which the ROC curves for two detectors cross, detector performance can be quantified in a *figure of merit* (FoM) equal to the area under the curve.

To obtain an ROC for a given detector, an experiment was run 1000 times in which a speckle pattern was simulated according to the model in (3.3). For each experiment, a set of simulations was performed where a line segment of every possible orientation (in the sense of Figure 3.1) was immersed in the noise realization. The detector in question was applied to the set of noise-only and signal-in-noise realizations, and the numerical detector output from each case was recorded. The simulations used a random number generator from *Numerical Recipes* [40] and linear algebra subroutines from LAPACK [41] and Matlab [42].

For each detector, the result of the simulation was two sets of $1000 \times 2(N-1)$ detector outputs, one for each line orientation in each separate experiment, and $2(N-1)$ for each noise-only speckle realization. This procedure is equivalent to generating 1000 detection statistics for each active hypothesis, and $2(N-1)$ for the null hypothesis. For any fixed threshold, the expected number of correctly detected signals in the $1000 \times 2(N-1)$ active hypothesis realizations is $1000 \times 2(N-1) \times p_D$, where p_D is the probability of correct detection. Similarly, the expected number of false alarms in the $1000 \times 2(N-1)$ null hypothesis realizations is $1000 \times 2(N-1) \times p_F$, where p_F is the probability of false alarm. Thus, p_D and p_F can be estimated by

$$p_D = \frac{1}{1000 \times 2(N-1)} Q_D \tag{3.40}$$

and

$$p_F = \frac{1}{1000 \times 2(N-1)} Q_F, \tag{3.41}$$

where Q_D and Q_F are respectively the number of active and null hypothesis test statistics exceeding the threshold.

The variance of these estimates are $(p_D - p_D^2)/1000$ and $(p_F - p_F^2)/1000$ which are upper bounded by 2.5×10^{-4}, since p_D and p_F lie between 0 and 1. The probabilities p_D and p_F are actually functions of the threshold applied; the locus of (p_F, p_D) obtained by varying the threshold is the ROC curve. The area under the curve, used as a figure

of merit, also has variance upper bounded by 2.5×10^{-4}; this is actually a loose upper bound, however, as it assumes no correlation between p_D and p_F at different thresholds.

Note that the ROC curves given here represent average detector performance over all possible stick orientations. Note also that we have not considered the problem of correctly classifying target orientation; if a statistic mismatched in orientation to the target returns the maximum value, it is simply accepted as a correct detection. The different detectors do not appear to differ in their classification ability, however no complete study of this topic has been undertaken.

The severity of the noise and the power of the detectors evaluated were controlled by setting several parameters. First, the "stick length," or linear size of the operator affects the performance of the detector in a direct way. A long stick will smooth speckle better than a short stick, but possibly at the expense of also smoothing out edge features. In practice, we expect that the edges are only locally approximated by the linear model; i.e., we assume some curvature to the edges. Therefore in actual image processing, this parameter should be set as long as the length over which the edges are expected to be roughly straight [14]. In the simulations here, the signal is always matched perfectly in length by the detection template. Thus if all noise parameters are set equivalently, a longer stick will outperform a shorter stick, since it averages over more data.

In the simulations presented here, the correlation length of the speckle was controlled by changing the size of the smoothing kernel used to introduce correlation to the underlying Gaussian noise; a size of 1 implies white noise with variance 1. The smoothing kernel is Gaussian in shape, and is truncated at some point. To keep the simulations to manageable length, the kernel size could not be made large enough to allow the noise correlation to taper gradually to zero. However, since the goal of the simulations was to compare detector performance in arbitrarily correlated noise, the short-term correlation is sufficient to model reality.

In the following subsection, simulation results will be reported in terms of low, medium and high signal amplitude. No numerical values are given for signal to noise ratio because of the difficulty in defining a meaningful SNR in non-additive, possibly correlated noise. The distinctions used here are sufficient to illustrate the relative powers of detectors, over a range of signal to noise ratios.

3.3.1 Comparison of detectors in white speckle noise

Figure 3.2(a) shows the ROC curves for the Sticks detector, the deflection-optimal detector and the optimal white noise detector defined in (3.7) for a low signal amplitude scenario. The noise level is very severe, and no detector does a very acceptable job for noise this strong. A sample noise realization at this noise level is given in Figure 3.2(b), which shows a diagonal line which is almost totally obscured by the noise.

Figure 3.3(a) shows ROCs for the Sticks detector, the deflection-optimal detector and the optimal white noise detector for a higher signal amplitude white noise simulation. In the sample noise realization in Figure 3.3(b), the diagonal line is more prominent than in Figure 3.2(b). As in the low signal amplitude case, the three detectors offer very similar performance; since the Sticks detector is much more computationally simple than the deflection and optimal detection rules, we conclude that the simple linear matched filter (Sticks) is sufficient to obtain near optimal performance in the case of white speckle.

3.3.2 Comparison of detectors in colored speckle noise

Figures 3.4(a), 3.5(a) and 3.6(a) show ROCs comparing the performance of Sticks with that of the deflection-optimal detector and the prewhitened Sticks detector in the low, medium and high signal amplitude colored noise cases. Noise realizations at these noise levels are presented in Figures 3.4(b), 3.5(b) and 3.6(b). The stick length has been changed from the setting used in the white noise case to ensure that it is longer than the correlation length induced by the coloring kernel.

For the low signal amplitude case, we see a clear increase in performance as we move from the simple linear Sticks detector to the more sophisticated linear prewhitened Sticks detector to the quadratic deflection-optimal detector. This is reasonable, since in general, the optimal linear-quadratic detector must be no worse than the optimal linear detector and may in fact be more powerful. What is surprising is that, especially in the medium and high signal amplitude cases, the deflection-optimal and prewhitened Sticks detectors perform almost equally well. This indicates that the optimal linear-quadratic detector is dominated by its linear component, which is approximately the same as the prewhitened Sticks detector.

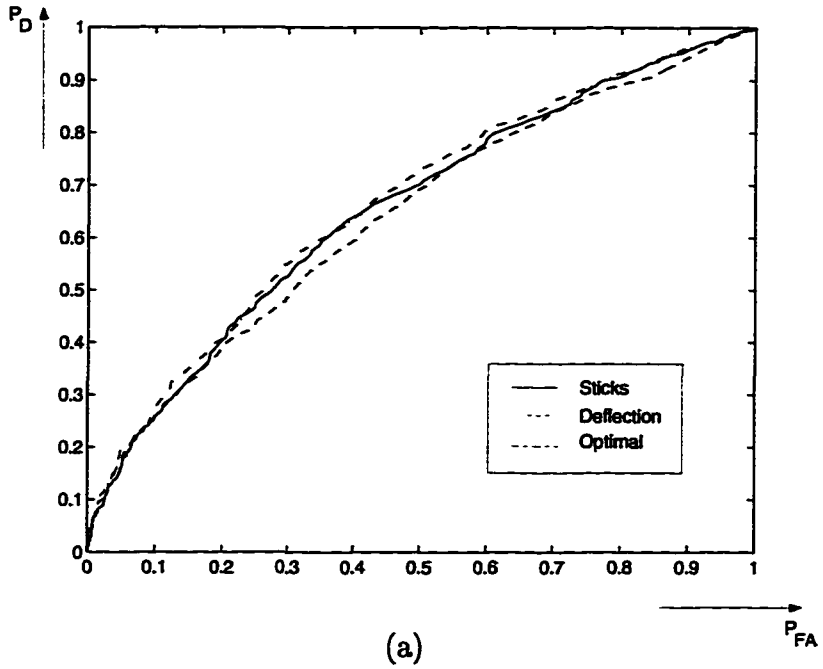

(a)

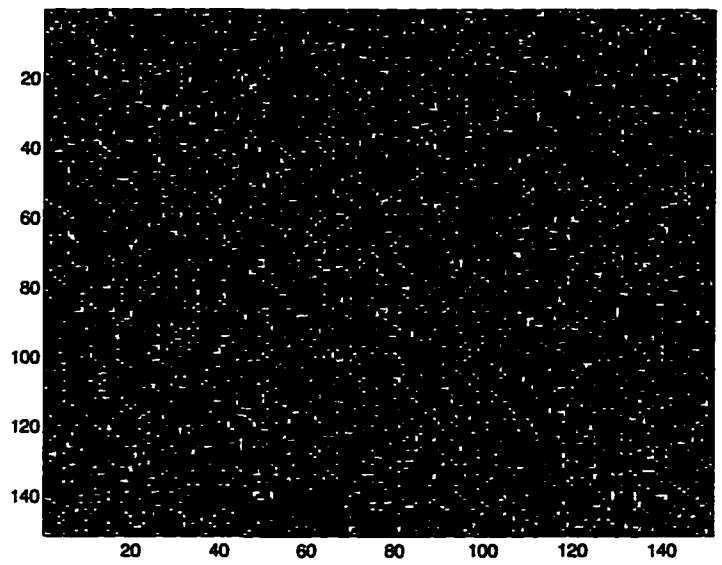

(b)

Figure 3.2 (a) ROC curves comparing detectors in white noise with low signal amplitude. and (b) Sample image prepared with the signal and noise settings used in calculating the ROCs. The signal is a diagonal line barely visible through the noise; this is an unrealistically low SNR simulation of ultrasound imaging. The simulation parameters used here are stick length = 5, kernel size = 1 (white noise), signal amplitude = 1.0 . The poor performance of even the optimal detector is due to the very poor image quality.

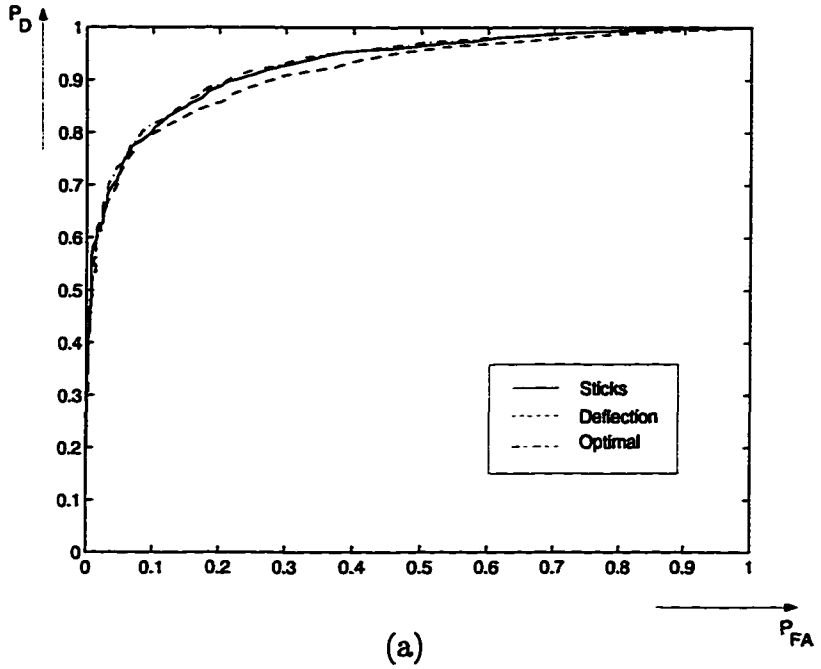

(a)

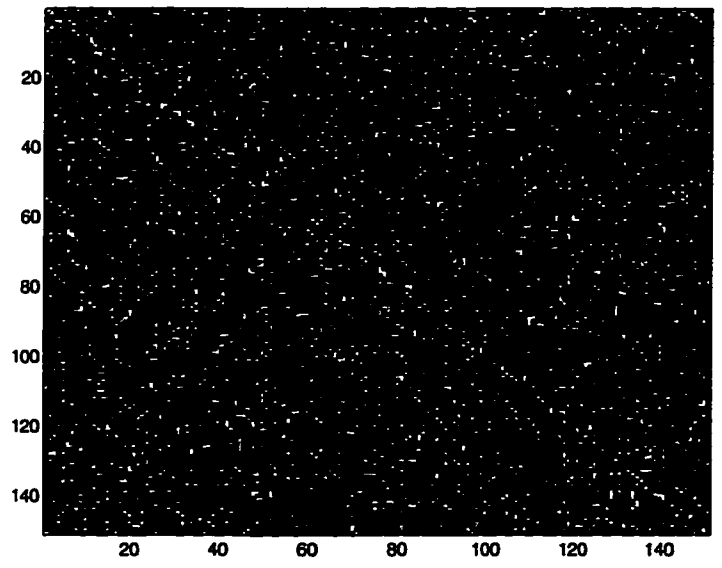

(b)

Figure 3.3 (a) ROC curves comparing detectors in white noise at a higher signal amplitude, and (b) Sample image prepared with signal and noise settings used in calculating ROCs. The simulation parameters used here are stick length = 5, kernel size = 1 (white noise), signal amplitude = 2.0 . This noise level is much more representative of ultrasound image quality than that portrayed in Figure 3.2. The diagonal line is visible, though still significantly noise corrupted. Uncorrelatedness of the noise could be achieved in practice by decimating the image to the theoretical resolution limit of the device used in producing the image.

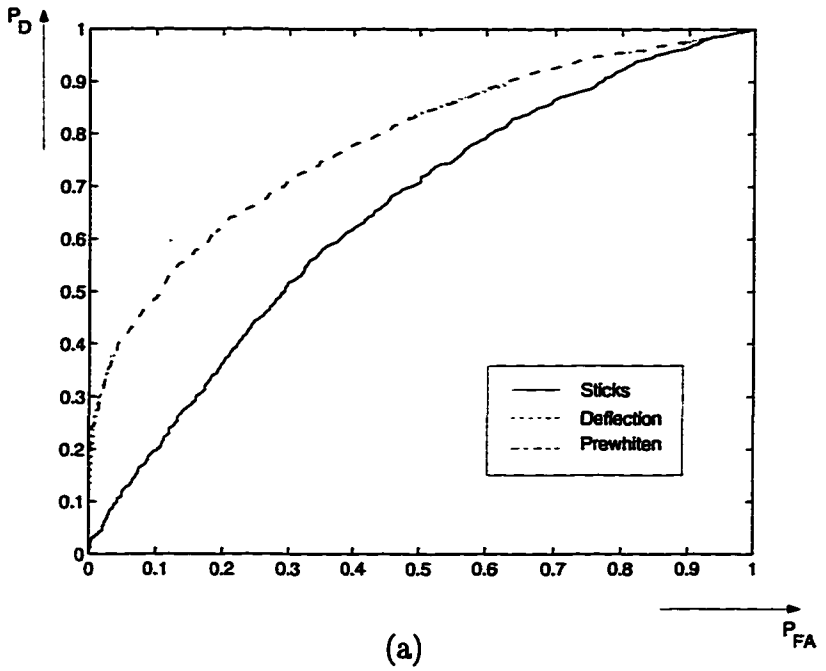

(a)

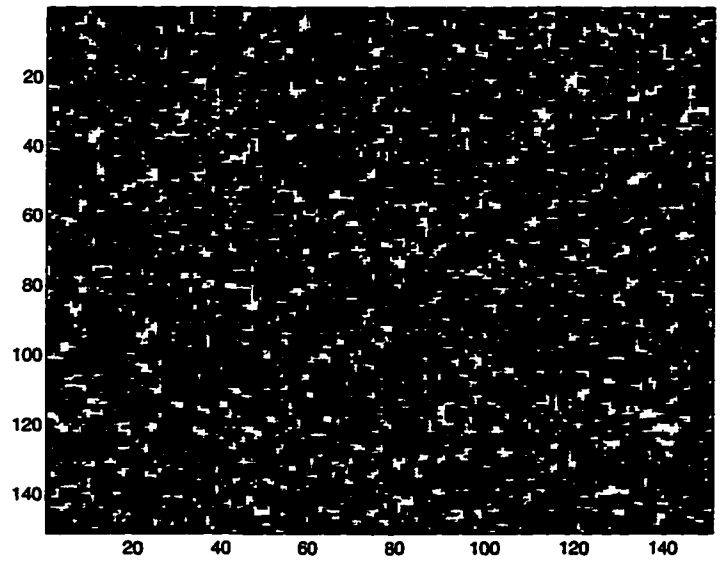

(b)

Figure 3.4 (a) ROC curves comparing detectors in colored noise at low signal amplitude and (b) Sample image prepared with signal and noise settings used in calculating ROCs. The simulation parameters used here are stick length = 7, kernel size = 3, signal amplitude = 3.0 . As in Figures 3.2 and 3.3, the signal present is a diagonal line from upper left to lower right. As in Figure 3.2, this represents an unrealistic simulation of ultrasound speckle. It does serve to illustrate the benefits of prewhitening, however, as Figure 3.4 shows a clear improvement of the prewhitening and deflection detectors over simple Sticks.

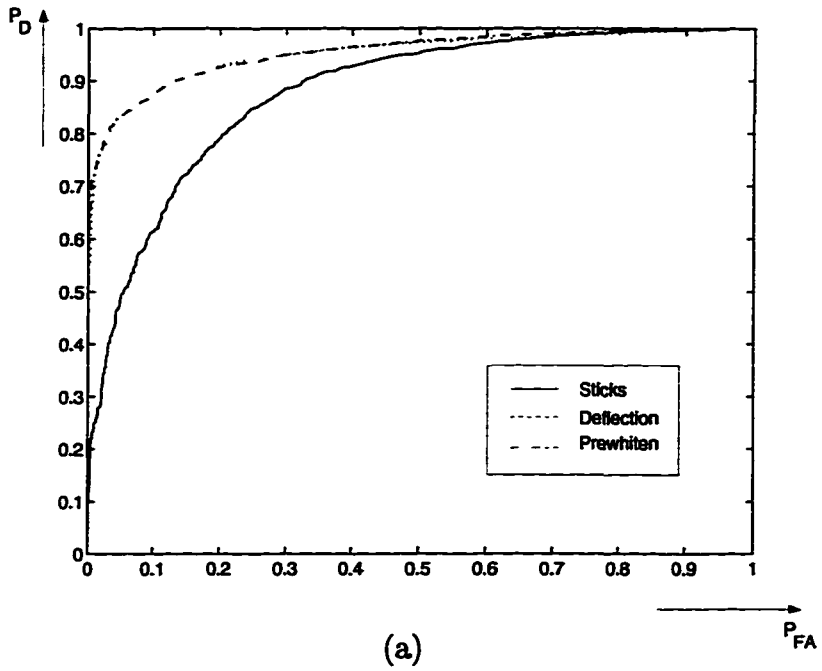

(a)

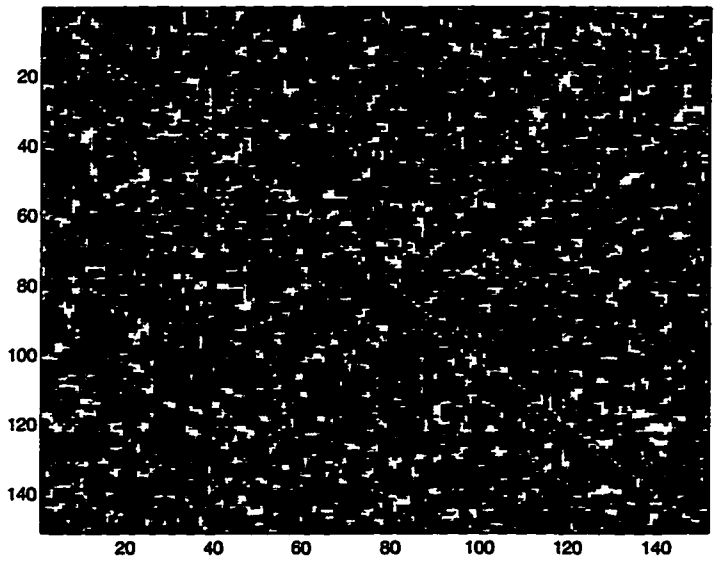

(b)

Figure 3.5 (a) ROC curves comparing detectors in colored noise at medium signal amplitude, and (b) Sample image prepared with signal and noise settings used in calculating ROCs. The simulation parameters used here are stick length = 7, kernel size = 3, signal amplitude = 5.0 . The signal present is again a diagonal line from upper left to lower right. This noise level is more representative of ultrasound image quality than that in Figure 3.4(b), but still represents a rather low SNR. In this case, the performance of the deflection and prewhitened Sticks detectors is approximately optimal, and simple Sticks somewhat worse. We conclude that in the medium signal amplitude case, the noise coloring is much more important as a corrupting influence than non-Gaussianity.

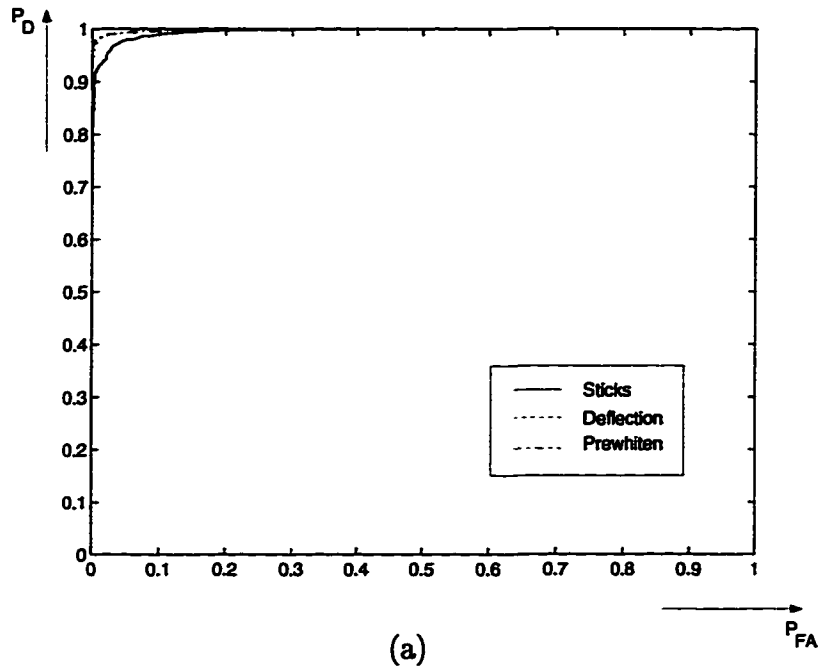

(a)

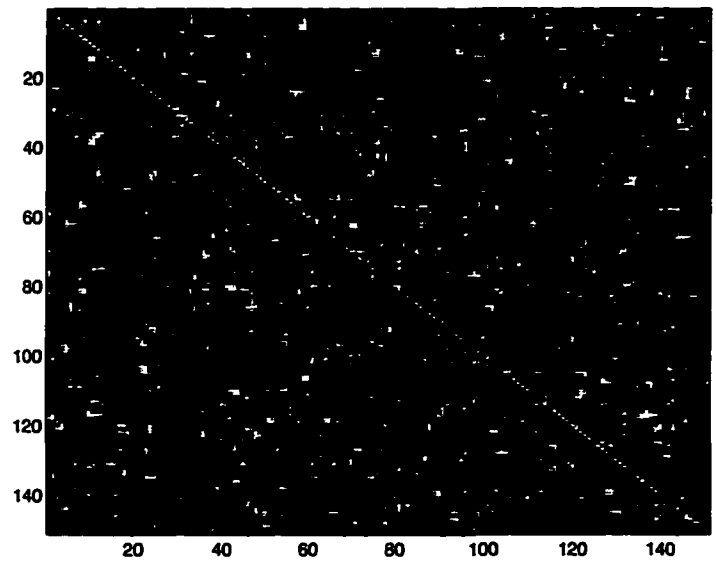

(b)

Figure 3.6 (a) ROC curves comparing detectors in colored noise at high signal amplitude, and (b) Sample image prepared with signal and noise settings used in calculating ROCs. The simulation parameters used here are stick length = 7, kernel size = 3, signal amplitude = 8.0 . The signal present is again a diagonal line from upper left to lower right. This noise level is more representative of ultrasound image quality than the noise in Figures 3.4 and 3.5. As in Figure 3.5, the deflection and prewhitened Sticks detectors give nearly optimal performance.

This result, along with the near optimality of Sticks detection of lines in white speckle noise, implies that the *coloring* of speckle affects the performance of a detection rule more than the non-Gaussianity of the noise. It also suggests that prewhitened sticks may approach optimality in the colored speckle case as nearly as does Sticks detection of lines in the white noise case. In colored noise, however, the use of an inverse filter is superior to decimation as a whitening operation because the decimation causes a loss in signal power without reducing noise power. This is because shorter sticks must be used, since the lines to be detected are reduced in pixel length by the decimation.

It must be noted that the success of any statistically motivated detection rule is highly sensitive both to errors in estimating noise statistics and defining the target model. In many situations, including ultrasound image processing, it may not be possible to reliably estimate the noise statistics without averaging over an area of image containing unwanted statistical variations (such as targets and varying SNR). One possible solution is to use an adaptive whitening filter to decorrelate the noise. Since the noise correlation is separable into axial and transverse components, a one-dimensional filter can be applied successively in each direction, and will be able to operate on the entire image in spite of the changes in noise correlation or SNR that occur from region to region.

Finally, a difficulty arises in detection because the stick model for line segments is itself imprecise. If the actual targets are broader than a single pixel, for example, the performance of detectors which use off-stick regions of the image may be dramatically reduced. The ROC curves presented here thus represent performance bounds on detection rules of a fixed order searching a known statistical environment for a precisely defined target; actual performance under realistic circumstances will be somewhat less.

3.3.3 Comparison of rotating kernel techniques

The rotating-kernel min-max (RKMT) transforms proposed by Lee and Rhodes [26, 27, 28, 29] and summarized in Table 3.1 are compared in performance with the Sticks detector in Figure 3.7. The RKMT detectors differ from Sticks in that instead of simply using the maximum stick projection at each point as the test statistic, the RKMT detectors use the difference between the maximum and minimum stick projections. While

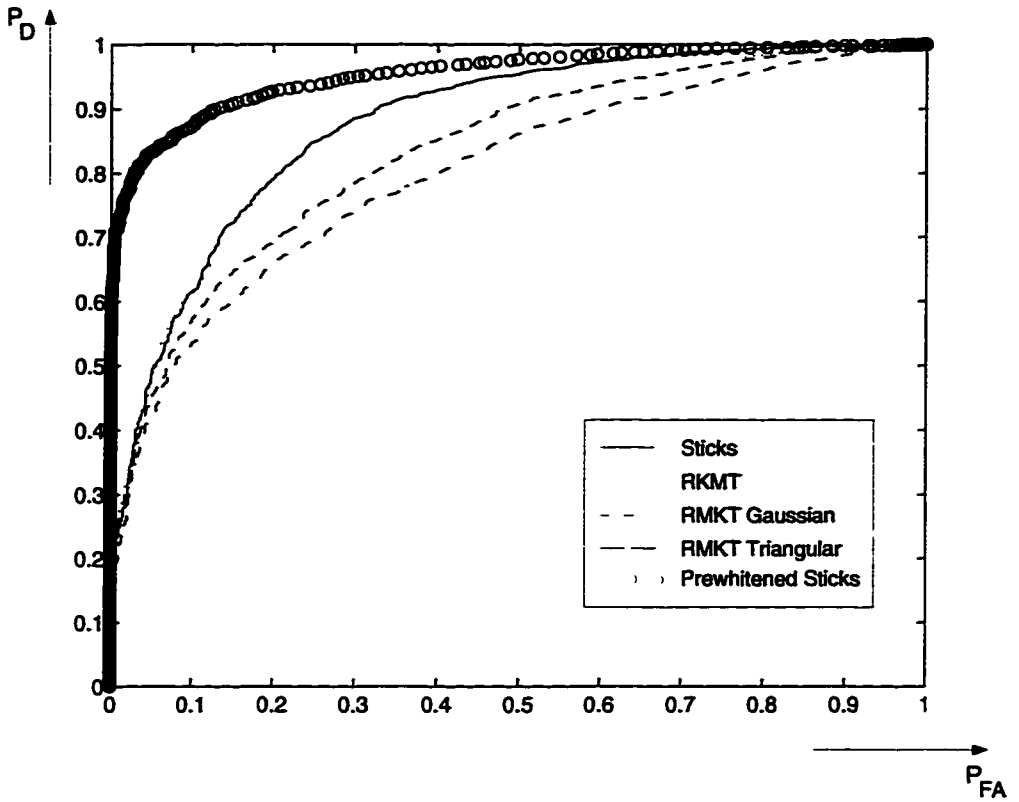

Figure 3.7 ROC curves comparing Sticks with RKMT detectors in colored speckle noise. RKMT detection is suboptimal in constant SNR case, but may be useful for detection when the SNR or general brightness level varies within an image.

the RKMT detectors are suboptimal for the general detection problem, they may find application in cases where the target strength varies from point to point in the image, or the targets are curving lines. While these scenarios can not be adequately simulated, they may nevertheless arise in real imaging problems.

3.3.4 Comparison of techniques by figures of merit

The comparison of detection rules in this section is summarized in Table 3.2, in which figures of merit are computed for each detector in each experiment by calculating the area under the corresponding ROC curve. The values in Table 3.2 have a variance less than 2.5×10^{-4}. The table contains no surprises; in the white noise case when an optimal

Table 3.2 Figures of Merit for Detectors Surveyed

Detector	White low amp.	White high amp.	Colored low amp.	Colored medium amp.	Colored high amp.
Optimal White	0.661	0.932	–	–	–
Deflection	0.642	0.919	0.800	0.954	0.997
Prewhitened Sticks	–	–	0.784	0.954	0.999
Sticks	0.657	0.930	0.649	0.879	0.995
RKMT	0.595	0.870	0.621	0.855	0.993
RKMT-Gauss	0.574	0.793	0.631	0.802	0.954
RKMT-triangle	0.571	0.781	0.635	0.833	0.980

detector is available, it always offers the highest FoM. Otherwise, the deflection detector generally features the highest FoM, followed by the prewhitened Sticks detector (in the colored noise case), the Sticks detector, and finally the suboptimal RKMT detectors. In a few cases, the deflection detector has a lower FoM than another detector. This is likely due to the fact that the deflection operators are selected to maximize the deflection criterion, not this particular figure of merit, which is a more appropriate measure of detector power in non-Gaussian noise.

In the colored noise cases, the deflection and prewhitened Sticks detectors yield the best performance of any technique surveyed here. The deflection detector is quadratic in the observation, and requires higher complexity than the linear techniques to compute the test statistic at each point. Furthermore, the coefficients used in the deflection detector are obtained by solving a large set of equations; solving for the coefficients is straightforward, but computation-intensive. The other detectors surveyed do not require such elaborate computation to determine the detection rule.

By comparison, the new prewhitened Sticks detection rule is a linear function of the observation, requires low computational complexity ($O(N^2)$ multiplies per pixel, where N is the stick length), and offers excellent performance. When second-order statistics for the speckle field can be exactly estimated, the prewhitened Sticks detector is the technique of choice. Finally we note that when SNR is high, the added expense of estimating statistics

for the prewhitened Sticks or deflection detectors may not be worthwhile, since Sticks itself compares favorably, especially in the white noise case.

3.3.5 Enhancement of real images

The Sticks technique has been very successful in our work in enhancing images for boundary detection. While it is impossible to define the "right" answer as precisely as in simulations, an image formed by plotting the Sticks detection statistic at each point is much smoother and visually more easily interpretable. Figure 3.8(a) shows a 512 × 442 pixel image of a pig muscle collected with a commercial medical ultrasound scanning system. Figure 3.8(b) shows a Sticks processed image, using an operator of length 15 pixels. This operator size was determined by subjectively estimating the length over which the boundaries appear to be composed of straight-line segments. In practice, the stick length can often be set using prior knowledge of the specific problem being addressed. A comparison of the results with different stick lengths will be presented in Chapter 4.

Note the thin boundary between the two top layers of subcutaneous fat, emphasized in the processed image even though it is only a few pixels wide. An equivalent size (for example 4 × 4 pixel) median or linear low-pass filter would be incapable of enhancing long straight components as well as the present technique, while filtering with a larger operator, such as a 15 × 15 filter would obliterate features such as dark gaps between lines [43]. Adaptive or stick-like median filters [43, 44] are an alternative to stick-projection processing. Finally, the text displayed at the bottom of Figure 3.8(a) is also processed and displayed in Figure 3.8(b). The tendency of the Sticks to resolve image features into lines is evident in the processed text, where connections are made between letters, and between unconnected parts of letters. In medical imaging, tightly curving features such as lettering are uncommon; in more general image processing applications, such as SAR, intersections of lines at acute angles might be more common. The Sticks technique must therefore be used with care, especially in the vicinity of line intersections where the templates model the image features very poorly.

3.3.6 Threshold selection for Line Detection

Great care must be used in applying a threshold in real data analysis, as a fixed threshold may not be appropriate at every point of the image. Sticks processed images were successfully used to estimate fat and muscle thicknesses in ultrasound scans of beef carcasses in connection with Beef Ultrasound Grading Project (BUGS) at the Bioacoustics Research Laboratory at the University of Illinois (see Appendix A). The data varied significantly in quality during this project, and so tissue boundaries were identified by extracting a cross-sectional trace, and selecting with the highest point that 1) exceeded a low threshold, 2) was a local maximum, and 3) fell between a region known with high probability to contain the desired feature.

More analytically, it is possible to use a threshold which achieves a constant false alarm rate (CFAR). A threshold is selected which produces a certain acceptable number of false alarms in a region known not to contain a boundary. This threshold is then used throughout the image. The performance of this thresholding technique can be analyzed as follows. Assume the speckle is Gaussian distributed with first- and second-order statistics the same as in Section 3.2.2. Here we will consider the image itself, without the mean subtracted off as in that earlier discussion, and neglect interpixel correlations ($\rho_{ij} = 0$).

We set a threshold two standard deviations above the mean:

$$\begin{aligned} \gamma &= \mathrm{E}_0[\mathbf{s}^T\mathbf{x}] + 2\sqrt{\mathrm{E}_0\left[\left(bfs^T\mathbf{x}\right)^2\right]} \\ &= \mathbf{s}^T\mathrm{E}[\mathbf{x}] + 2\sqrt{\mathbf{s}^T\mathbb{R}_0\mathbf{s}} \\ &= N\alpha(2\sigma^2) + 2N\alpha(2\sigma^2) \\ &= 3N\alpha(2\sigma^2), \end{aligned} \tag{3.42}$$

where $2\sigma^2$ is the variance of the underlying complex Gaussian random field, $\mathbb{R}_0 = \mathrm{E}_0[xx^T]$, $\mathbf{s}$ is the stick of the selected orientation and α is the amplitude of the stick operator itself. This threshold corresponds to a probability of false alarm of 0.004.

The probability of correct detection can be computed with knowledge of the first and second order moments under the active hypothesis:

$$\begin{aligned} \mathrm{E}_1[\mathbf{s}^T\mathbf{x}] &= \mathbf{s}^T\mathrm{E}_1[\mathbf{x}] \\ &= \mathbf{s}^T\left(2\sigma^2 + |\mu|^2\right) \\ &= N\alpha(2\sigma^2) + N\alpha\beta, \end{aligned} \tag{3.43}$$

and

$$\begin{aligned} \mathrm{E}_1[(\mathbf{s}^T\mathbf{x})^2] &= \mathbf{s}^T R_1 \mathbf{s} \\ &= (2\sigma^2)^2(N\alpha)^2 - 2(2\sigma^2)(N\alpha)^2\beta, \end{aligned} \tag{3.44}$$

where $\beta = \mathrm{E}_1[x]$, the expected magnitude of a target in the image.

Under this threshold, the probability of correct detection can be computed as

$$\begin{aligned} p_D &= \mathrm{erfc}\left(\frac{\gamma - \mathrm{E}_1[\mathbf{s}^\mathrm{T}\mathbf{x}]}{\sqrt{\mathrm{E}_1[(\mathbf{s}^\mathrm{T}\mathbf{x})^2]}}\right) \\ &= \mathrm{erfc}\left(\frac{4\sigma^2 - \beta}{2\sigma^2(2\sigma^2 - 2\beta)}\right), \end{aligned} \tag{3.45}$$

which is independent of the template amplitude; equally powerful tests can thus be implemented with unit amplitude sticks.

3.4 Conclusion

This chapter has discussed the theory of line detection for the case of speckle noise such as that which corrupts acoustical and radar images. It represents a comprehensive survey of optimal and suboptimal approaches to detecting lines and boundaries in speckle noise. The optimal detectors are computationally expensive to implement in practice, so suboptimal detectors of linear and quadratic orders are surveyed as well. A statistical analysis is performed to compare the relative performances of the optimal and suboptimal detection rules under various noise colorings and powers; the resulting receiver operating characteristic curves are bounds on the performance of the detectors under ideal circum-

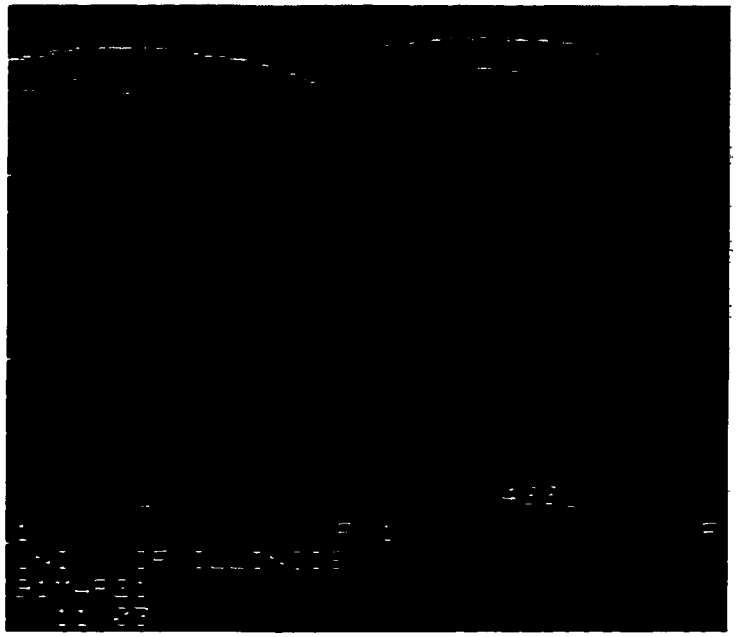

(a)

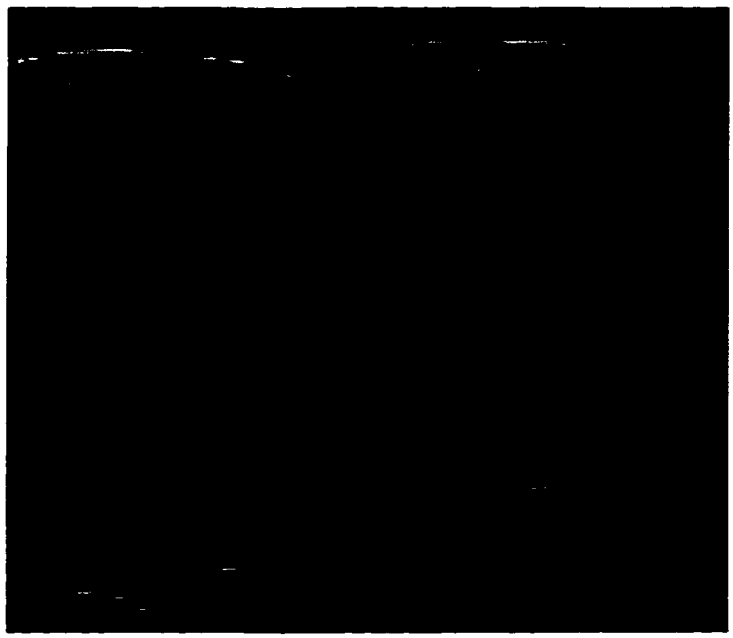

(b)

Figure 3.8 A 512 × 442 pixel image of a pig muscle (a) before and (b) after processing with length 15 stick operators. The resulting image is further modified by raising each pixel to the power 1.5, then renormalizing to 255 gray levels. The processed image is clearly enhanced, showing even thin lines without smearing, and rejecting background speckle, which typically appears as spots rather than lines.

stances. While the analysis as given here is valid only for the case of detecting lines and piecewise sticklike curves in Rayleigh speckle, it can be generalized to other multiple or composite hypothesis testing problems by using a different set of templates in place of the sticks discussed here, and adapting the noise model to fit the true statistics.

The performance comparison indicates that a linear scheme (Sticks) with the form of a matched filter in additive white Gaussian noise performs near optimally when the speckle is uncorrelated, for instance if the image has been decimated. In the case of colored speckle, a prewhitening step prior to the matched filter can yield dramatic improvement in performance if the speckle statistics are exactly known. In the absence of such knowledge, however, the Sticks detector is a useful approach that offers reasonable performance in a variety of noise environments. The image formed by plotting the Sticks output shows even very thin details from the original image clearly, while still smoothing the speckle. As a result, the machine detectability of image contours is substantially improved.

CHAPTER 4

APPLICATION OF LINE DETECTION TECHNIQUES TO MEDICAL ULTRASOUND

4.1 Boundary Detection in Medical Ultrasound

The boundaries of interest in an ultrasound scan correspond to discontinuities between tissue layers, which are large on the scales of both the wavelength of interrogation and the scan line spacing. In the two-dimensional scan plane, these three-dimensional surfaces take on the appearance of bright streaks against a darker, less densely reflecting background. Features with this appearance are unlikely to occur randomly in speckle noise; speckle's correlation structure is more likely to give rise to bright spots of characteristic size [4]. Conventional edge detection procedures, e.g., Canny, Roberts or Sobel operators [45, 46] and related techniques such as [22], are ill-suited to detect the boundaries because they are not well-modeled as step discontinuities in image intensity. In contrast, we have had success with an approach designed to respond preferentially to *line processes* [14, 43]. This approach results in an operator that is sensitive even to thin edges, while still providing for speckle reduction.

To formalize this idea, we have approached the problem of boundary detection with the techniques of statistical decision theory. This has led to a number of detection rules motivated by a statistical model for the targets and noise. In Chapter 3 we derived optimal boundary detection techniques and tested them in simulated speckle to establish performance bounds for other detectors. We compared several suboptimal detectors of varying complexity and power with the bounds and showed that a simple suboptimal detector based on the generalized likelihood ratio test (GLRT) is extremely robust in the face of an uncertain or inexactly modeled statistical environment. Furthermore, we were

able to quantify the performance lost in using this detector and identify circumstances in which that loss was negligible in Chapter 3. This chapter studies that detector in more detail, focusing in part on a number of different parameters which can be changed to alter its properties, such as the length and thickness of the templates used to model the boundaries.

This chapter also addresses a weakness of the technique in Chapter 3, the assumption that all orientation sticks are equally likely at each point. In practice this is not the case, since B-mode ultrasound is capable of imaging only those structures normal to the beam. To improve upon the performance of the basic technique, the image itself can be used to estimate a distribution on the angle of the lines at each point in the image. This prior information can help to reject unlikely hypotheses.

Finally, we introduce the use of false color as a visualization tool, to indicate the direction of the most prominent linear image feature at each point. The color can be applied to either the original or a processed image, and represents a way of displaying additional information on an image without changing the image gray scale itself. This is an important issue in medical ultrasound, where sonographers are skilled in interpreting unprocessed gray level images.

These issues are somewhat apart from simple detector power. In Chapter 3, the detection scenario was carefully controlled so that the target and noise statistics were known; here the various tradeoffs will be quantified by showing the effect of the different settings on the processing of a single real image. This test image is given in Figure 3.8(a), a scan of the longissimus muscle of a live pig, imaged with a PIE medical ultrasound scanning system and a Targa 16 Image Processing card. Each half of this image shows three major fat boundaries near the top of the image. These appear as bright streaks which grow fainter near the right hand side, especially the second boundary from the top, which appears to grow thinner as it fades out. The ability of different algorithms to enhance this boundary is a good criterion to use in comparing the performance of different detectors.

4.2 Effect of Stick Length and Thickness

The implementation of the Sticks technique requires a tradeoff between effective line enhancement and good speckle reduction. To obtain good results, the sticks should be made longer than the correlation length of the noise, yet shorter than the distance over which the boundaries appear to be straight lines. A longer stick achieves greater speckle suppression at the expense of a weaker match with more tightly curving boundaries; similarly, "fatter" sticks are more sensitive than thinner sticks to broad but dim boundaries.

Figure 4.1 shows a composite of images processed with sticks of lengths 1, 15 and 23 pixels, and thicknesses 1, 3 and 5 pixels. The longer sticks have the effect of blurring the speckle in the interior of the muscle, while more clearly emphasizing the boundaries between fat layers and the muscle. However, these effects come at the expense of visibility of certain image features, such as the thin boundary between the fat layers in the upper-right corner of the image. Increasing stick thickness has the effect of enhancing the relative brightness of the broad boundaries, while introducing some blur in the transitions between boundary and off-boundary pixels. More importantly, the use of thicker sticks makes very thin boundaries less visible.

These effects can be more quantitatively studied by considering the statistics of the stick operator output. Ideally, we hope to obtain a large valued, low variance output when a target is present and a small valued, low variance output when no target is present. A useful index of performance is given by

$$\begin{aligned} D(N,M) &= \frac{\mathrm{E}[Y(N,M)-Y(N,0)]^2}{\max(\mathrm{var}(Y(N,M)),\mathrm{var}(Y(N,0)))} \\ &= \frac{\mathrm{E}[Y(N,M)-Y(N,0)]^2}{\mathrm{var}(Y(N,M))}, \end{aligned} \tag{4.1}$$

where

$$Y(N,M) = \frac{1}{N^2}\left[\sum_{i=1}^{M} x_1(i) + \sum_{j=1}^{N-M} x_0(j)\right]. \tag{4.2}$$

This is the output of a size N stick of normalized energy, i.e., one containing N pixels, each of height $1/N^2$. The quantity $Y(N,M)$ is the sum of pixel intensities from M true target points and $N-M$ pure noise points, corresponding to partial overlap of a stick

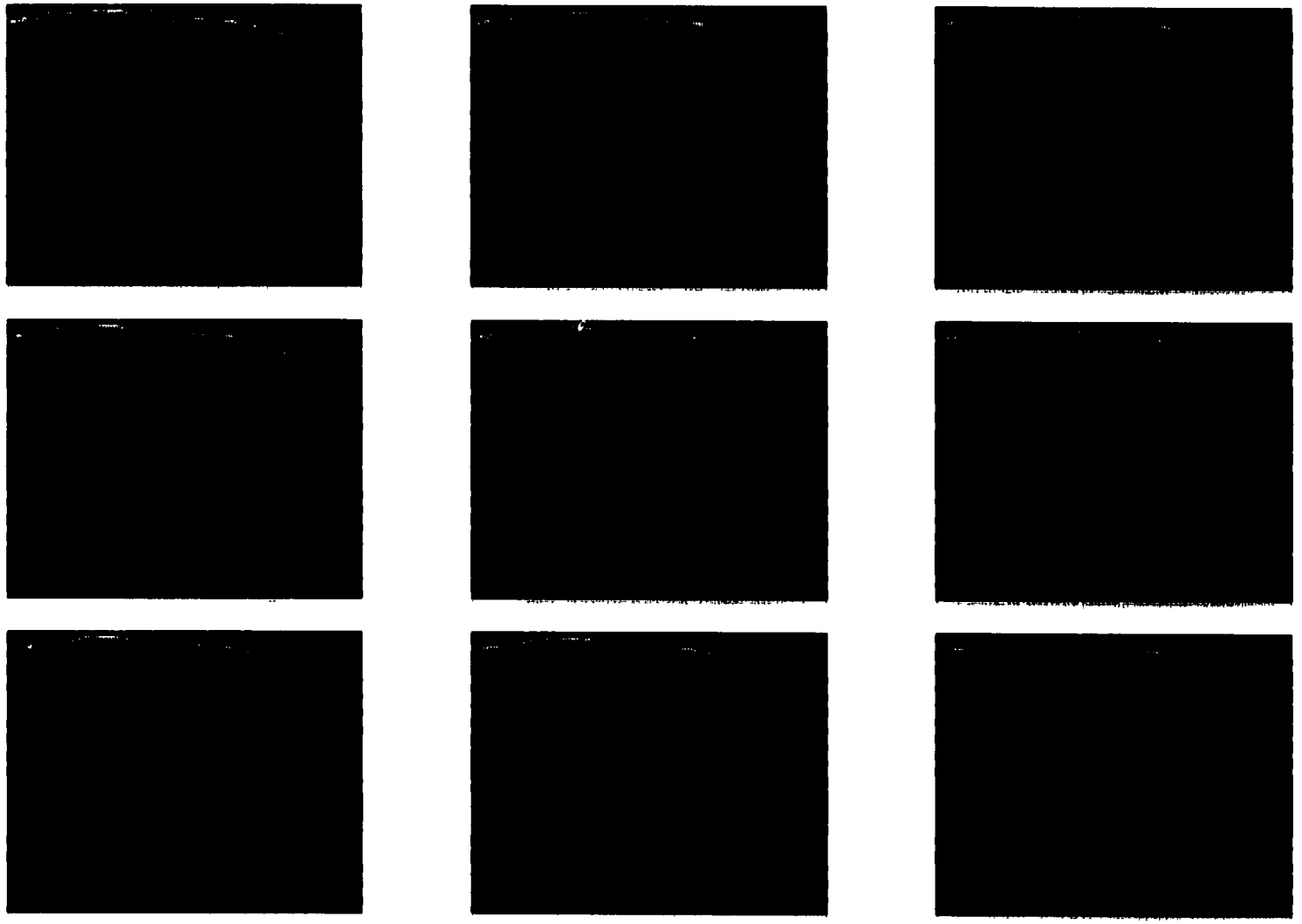

Figure 4.1 Composite of images processed with sticks of varying lengths and thicknesses. Length varies from 7 to 15 to 23 from left to right; thickness varies from 1 to 3 to 5 from top to bottom. (Image cropped to show detail.)

detection template with a target. Detection with a stick perfectly fit to the target is indicated by $Y(N,N)$, while the stick output under the null hypothesis is $Y(N,0)$.

The quantity $D(N,M)$ can be interpreted as a signal to noise ratio, since it is proportional to the square of the expected difference in stick output under active and null hypotheses, and inversely proportional to the variance under the active hypothesis, which is always greater than the null hypothesis variance:

$$\begin{aligned}
\mathrm{var}_1[X] &= \mathrm{E}[(|n+\mu|^2)^2] - \mathrm{E}[(|n+\mu|^2)]^2 \\
&= \mathrm{E}[|n+\mu|^4] - (|\mu|^2+\sigma^2)^2 \\
&= \mathrm{E}[|n|^4] + 4|\mu|^2\mathrm{E}[|n|^2] + \mathrm{E}[|\mu|^4] - |\mu|^4 - 2|\mu|^2\sigma^2 - \sigma^4 \\
&= \mathrm{E}[|n|^4] + 2|\mu|^2\sigma^2 \\
&= 2\sigma^4 + 2|\mu|^2\sigma^2 \\
&\geq \mathrm{var}_0[X] = 2\sigma^4. \qquad (4.3)
\end{aligned}$$

Notably, $D(N,M)$ is related to deflection [36], which is used as a criterion for the design of optimal linear-quadratic detection rules in Chapter 3, and also to the *contrast* [2] of the speckle pattern, which has been used in ultrasound tissue characterization (for example in [47] and [9]). Intuitively, $D(N,M)$ is large when the difference between the conditional means under the two hypotheses are large, and the variance of each is small.

If the speckle is assumed to be minimally correlated and described by Rayleigh/Rician statistics, the mean and second moment of $Y(N,M)$ are given by

$$\begin{aligned}
\mathrm{E}[Y(N,M)] &= \frac{1}{N^2}\mathrm{E}\left[\sum_{i=1}^{M} x_1(i) + \sum_{j=1}^{N-M} x_0(j)\right] \\
&= \frac{M\mu_1 + (N-M)\mu_0}{N^2}, \qquad (4.4)
\end{aligned}$$

and

$$\mathrm{E}[Y(N,M)^2] = \frac{1}{N^4}\mathrm{E}\left[\left(\sum_{i=1}^{M} x_1(i) + \sum_{j=1}^{N-M} x_0(j)\right)^2\right]$$

$$
\begin{aligned}
&= \frac{1}{N^4}\mathrm{E}\left[\left(\sum_{i=1}^{M} x_1(i)\right)^2 + 2\left(\sum_{i=1}^{M} x_1(i)\right)\left(\sum_{j=1}^{N-M} x_0(j)\right) + \left(\sum_{j=1}^{N-M} x_0(j)\right)^2\right] \\
&= \frac{1}{N^4}\left(\left\{M\mathrm{E}\left[x_1^2\right] + M(M-1)\mathrm{E}\left[x_1\right]^2\right\} + 2(N-M)M\mathrm{E}\left[x_1\right]\mathrm{E}\left[x_0\right]\right. \\
&\qquad \left. + \left\{(N-M)\mathrm{E}\left[x_0^2\right] + (N-M)(N-M-1)\mathrm{E}\left[x_0\right]^2\right\}\right) \\
&= \frac{1}{N^4}\left(M\sigma_1^2 + M^2\mu_1^2 + (N-M)\sigma_0^2 + (N-M)^2\mu_0^2 + 2(N-M)M\mu_0\mu_1\right)
\end{aligned}
\tag{4.5}
$$

where μ_1, μ_0, σ_1^2 and σ_0^2 are the means and variances of points in the image, statistics that can be calculated by application of the Gaussian moment theorem in terms of the underlying Gaussian random field statistics.

The variance of $Y(N,M)$ is then

$$
\begin{aligned}
\mathrm{var}[Y(N,M)] &= \mathrm{E}\left[Y(N,M)^2\right] - \mathrm{E}[Y(N,M)]^2 \\
&= \frac{1}{N^4}\left[M\sigma_1^2 + M^2\mu_1^2 + (N-M)\sigma_0^2 + (N-M)^2\mu_0^2 + 2(N-M)M\mu_0\mu_1\right. \\
&\qquad \left. - \left(M^2\mu_1^2 + 2(N-M)M\mu_0\mu_1 + (N-M)^2\mu_0^2\right)\right] \\
&= \frac{M\sigma_1^2 + (N-M)\sigma_0^2}{N^4}.
\end{aligned}
\tag{4.6}
$$

Finally, we calculate $D(N,M)$:

$$
\begin{aligned}
D(N,M) &= \frac{\mathrm{E}[Y(N,M) - Y(N,0)]^2}{\mathrm{var}(Y(N,M))} \\
&= \frac{(M\mu_1 + (N-M)\mu_0)^2/N^4}{(M\sigma_1^2 + (N-M)\sigma_0^2)/N^4} \\
&= \frac{(M\mu_1 + (N-M)\mu_0)^2}{(M\sigma_1^2 + (N-M)\sigma_0^2)}
\end{aligned}
\tag{4.7}
$$

in terms of the mean and variance of the speckle pattern.

For a given target size, $D(N,M)$ increases linearly with increasing stick length, reaching a maximum value when the stick exactly matches the target. When the stick is larger than the target, increases in stick size can only extend the operator to include pure noise. This results in an increase in M, and a constant value of N, leading to a decrease in $D(N,M)$. The value of $D(N,M)$ is plotted for targets of varying length in 5.2 dB noise

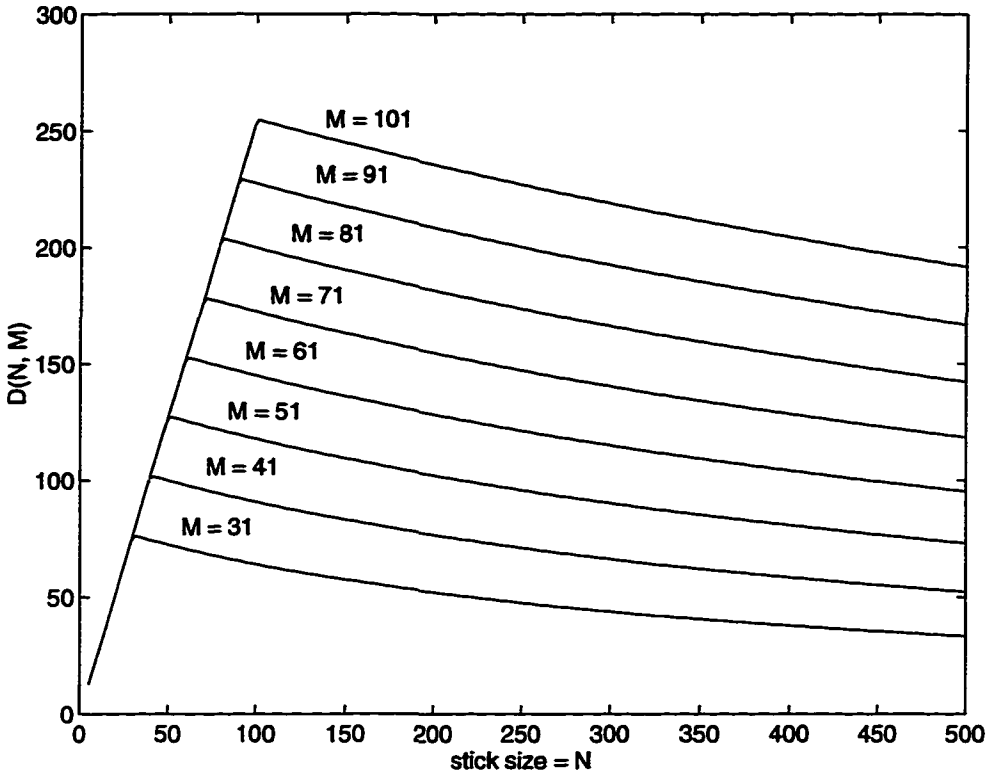

Figure 4.2 $D(N, M)$ for targets of indicated length in 5.2 dB simulated speckle. As stick size increases up to the target length, $D(N, M)$ increases linearly; when stick size N is larger than the target size M, $D(N, M)$ decreases, indicating optimal performance when the stick is well-matched to the target.

in Figure 4.2. The figure shows the costs of under- or over-estimating the target size when selecting a stick length and thickness. While the costs of under-estimation appear more significant, the penalty for over-estimation still must not be ignored. Since stick length and thickness are generally set once for an entire image, care must be taken to ensure that an adequate value is selected. The potential exists for an adaptive size stick; however, this topic is beyond the scope of this dissertation.

4.3 Decision Directed Sticks

Implicitly, the techniques described above have assumed that the boundaries are uniformly distributed in their orientation. For the case of medical ultrasound, this is an unwarranted simplification, because the modality is physically incapable of imaging structures which lie parallel to the interrogating sound beam. In fact, the boundaries in an acoustic image will almost all be oriented nearly perpendicularly to the beam direction.

Inclusion of a set of prior probabilities for the line orientation in the detection rule can greatly improve on the performance of the GLRT. The GLRT is similar to a likelihood ratio test (3.1), except that the numerator

$$LRT(\mathbf{x}) \sim \sum_i \pi_i \text{Prob [Receive } \mathbf{x} \mid i \text{ th target present]} \tag{4.8}$$

is replaced with a conditional pdf for the maximum likelihood hypothesis:

$$GLRT(\mathbf{x}) \sim \max_i \text{Prob [Receive } \mathbf{x} \mid i \text{ th target present]}. \tag{4.9}$$

It is most useful when the priors π_i are unknown. If the priors are known or can be estimated, however, we can replace the maximum likelihood estimate in (4.9) with a more powerful maximum *a posteriori* estimate, which we call the decision-directed Sticks detector:

$$DDS(\mathbf{x}) \sim \max_i \pi_i \text{ Prob [Receive } \mathbf{x} \mid i \text{ th target present]}. \tag{4.10}$$

The new test can be implemented by thresholding

$$\begin{aligned}
\gamma &= \max_i \frac{\pi_i \, p_{r \mid H_i}(x \mid H_i)}{\pi_0 \, p_{r \mid H_0}(x \mid H_0)} \\
&= \frac{1}{\pi_0} \max_i \frac{\pi_i \exp\left(\frac{1}{2\sigma}(x-\mu_i)^T(x-\mu_i)\right)}{\exp\left(x^T x^T\right)} \\
&\approx \max_i \pi_i \exp\left(\frac{1}{\sigma^2}\langle x, \mu_i\rangle + \frac{1}{2\sigma}\langle \mu_i, \mu_i\rangle\right) \\
&\approx C \max_i \exp\left(\log \pi_i + \frac{1}{\sigma^2}\langle x, \mu_i\rangle\right)
\end{aligned}$$

$$\approx \max_i \left(\log \pi_i + \frac{1}{\sigma^2} \langle x, \mu_i \rangle \right) \tag{4.11}$$

where $\langle \cdot, \cdot \rangle$ denotes an inner product, μ_i denotes the ith target, and σ^2 is the variance of the noise, assumed to be white and Gaussian, and $C = \exp\left(\frac{1}{2\sigma} \langle \mu_i, \mu_i \rangle\right)$, a constant with respect to i, since all the sticks are the same length and have equal energy. Note that since $0 \leq \pi_i \leq 1$, it is known that $\log \pi_i \leq 0$; thus, the prior term in (4.11) is a penalty on less probable orientations. Furthermore, the penalty is possibly quite stiff, since $\lim_{x \to 0} \log x = -\infty$.

The division of the projection value by the noise variance has an additional interpretation: the prior information attains greater significance in higher noise levels when the projection is highly noisy. Conversely, when the noise level is lower, the projection information is given more weight. In the case of a very high signal to noise ratio, the test reduces to the case of the original Sticks algorithm. If μ_i has values 0 or 1, as in the formulation we have used for line detection, (4.11) reduces to the selection of the line sum with the maximum value after a penalty has been applied to terms unlikely to be true lines. The original Sticks algorithm is obtained as a special case by assuming equal priors, or when the signal to noise ratio is very high.

Even though it is known that only targets perpendicular to the beam will yield strong reflections, it may not be possible to infer a set of prior probabilities from scanning geometry alone. Thus, it is highly desirable to estimate the priors from the image itself. In [39], we presented the the following method of performing this estimation. First, the Sticks algorithm is used to determine the angle of the most prominent line segment passing through each point. Assuming additive white Gaussian speckle for simplicity, this estimate is the maximum likelihood estimate of the orientation of the line present, if one exists. Next, a histogram is formed of the estimated angles near each pixel (e.g., within the support of the stick operators). This histogram is normalized to unit volume and used as a prior distribution on line segments passing through the point. This technique is inspired by the treatment of maximum *a posteriori* probability estimation in [48].

The decision-directed Sticks algorithm can thus be written in three steps [39]: the determination of the most probable line direction at each point, the computation of a prior probability for each angle at each point, and the computation of the final test

statistic:

$$\alpha(x,y) = \arg\max_{\theta} \sum_{i,j} s_\theta(i,j) f(x-i, y-j) \tag{4.12}$$

$$\pi_\theta(x,y) = \sum_{i,j} w(x+i, y+j) I(\alpha(x,y) = \theta) \tag{4.13}$$

$$f'(x,y) = \max_{\theta_i} \left(\log \pi_\theta(x,y) + \frac{1}{\sigma^2} \sum_{i,j} s_\theta(i,j) f(x-i, y-j) \right), \tag{4.14}$$

where $f(x,y)$ is the original image and $f'(x,y)$ denotes the output test statistic, $\alpha(x,y)$ denotes the most probable line orientation at point (x,y), $s_\theta(i,j)$ is a stick at the θ orientation, $w(x,y)$ is a mask function which is unit valued on the union of the support of the sticks and zero-valued elsewhere, $\pi_\theta(x,y)$ is the computed probability of a line at orientation θ at point (x,y), and $I(expr)$ is the indicator function, equal to 1 if *expr* is true, 0 if false.

Figure 4.3(a) shows the result of a length 7, thickness 1 decision-directed Sticks procedure The improved speckle reduction and increased contrast of the boundaries between fat and muscle layers are clear in a comparison of this figure with Figure 4.3(b), which shows an image resulting from length 7, thickness 1 sticks. A vertical slice of each of these images is given in Figure 4.4. These slices show the increases in boundary detectability that result from using the Sticks and decision-directed Sticks procedures. In Figures 4.4(b) and (c) the boundaries are marked by narrower peaks, and the non-boundary points by lower intensity, especially in the decision-directed Sticks image slice, Figure 4.4(c).

4.4 Image Enhancement with False Color

The Sticks technique can be described as a GLRT for lines in additive white Gaussian noise. As such, it is suboptimal even when the noise model is correct. It does, however, have the property that pixels are summed along the maximum likelihood target orientation. It therefore is of value to display not only the magnitude of the test statistic at each point, but also the orientation of the stick which produced the maximum output. This can be accomplished by assigning each pixel an orientation dependent hue in addition to the intensity value proportional to the detector output.

(a)

(b)

Figure 4.3 Original image processed with (a) length 7, thickness 1 sticks, and (b) length 7, thickness 1 decision-directed Sticks procedure.

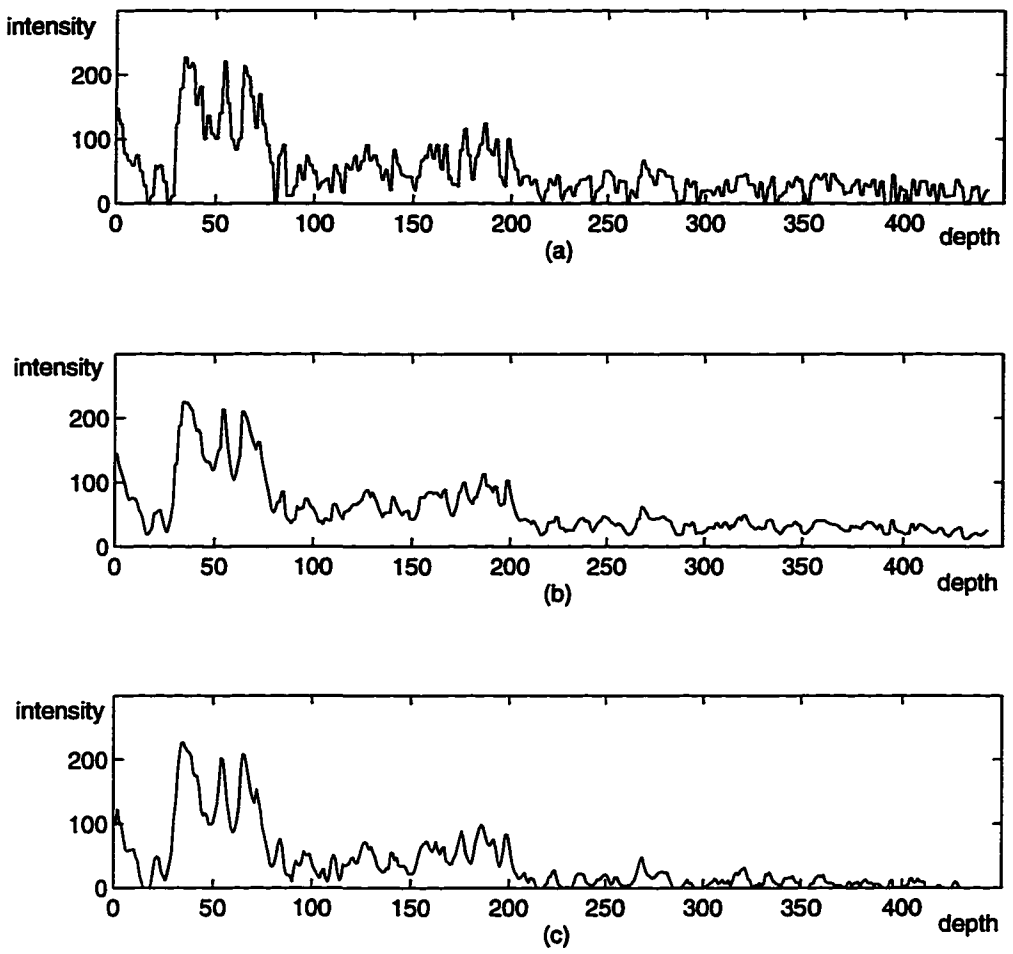

Figure 4.4 Vertical cross sections of the original image (a) and the processed images in Figure 4.3: length 7, thickness 1 sticks (b), and length 7, thickness 1 decision directed sticks (c). Both processing algorithms are effective at reducing noise and making boundary peaks more easily detectable, especially the decision directed approach in (c).

The idea of applying false color to an ultrasound image was used in [49] to display statistical properties of the backscatter at each point. We feel the notion has broad applicability in ultrasound image enhancement and that false color applied to the Sticks procedure can significantly improve the detectability of weak features. Additionally, it provides image detail that otherwise would not be known. As was the case with the decision directed Sticks procedure, the use of false color to display angle information can be implemented in conjunction with any Sticks or rotating kernel technique.

The problem of displaying angle and intensity as a color is one of displaying a hue, saturation and intensity (HSV) color space. This is complicated, because while HSV is a natural space for describing perceptible colors, not every HSV triplet can be made up of the red, green and blue (RGB) components which compose standard computer displays. Thus, the mapping from HSV to RGB space is not exact or unique. Figure 4.5 was produced using the procedure shown in Table 4.1.

Example images resulting from enhancement with false color are shown in Figures 4.5 and 4.6. These figures show the original image and the Sticks output image in false color obtained by coding the orientation of length 15, thickness 1 sticks as a hue. Note that the uncolored images can be obtained from the colored ones by summing red, green and blue components and normalizing to suit the display's dynamic range. In clinical applications, the ability to display additional information without "corrupting" the original image is important because the expertise of the ultrasound sonographer is highly specialized in analyzing images with standard appearance.

Figure 4.5(a) and Figure 4.6(a) show the raw false color images, where hue is equally distributed over all angles. Figure 4.5(b) and Figure 4.6(b) show the same images, but with a color map which shows almost a full spectrum of color in the range of angles that describe the fat boundaries near the top of the image. The colored circle visible in the image was superimposed on the raw image and processed along with the rest of the image; its color at various points on its diameter indicates the hue assigned to boundaries at corresponding orientations.

The colored images, especially the (b) images show clearly that the outermost fat boundary is in actuality two separate boundaries, a fact which is much more visually apparent than in the corresponding gray scale images. Thus, a more precise characterization

(a)

(b)

Figure 4.5 Original image with false color applied to indicate the direction of the most prominent stick at each point. The hue applied is obtained from the direction of the most prominent length 15, thickness 1 sticks at each point. The colored circle visible in the image was superimposed on the raw image and processed along with the rest of the image; its color at various points on its diameter indicates the hue assigned to boundaries at corresponding orientations. The image shows a range of hues along curving lines, such as the fat boundaries near the top of the image. Image (a) is obtained by distributing hues evenly about the color circle; Image (b) is the result of warping the colormap to show a full spectrum along the broad boundary at the top of the image.

Table 4.1 Conversion from (H,S,V) to (R,G,B) color space. Adapted from [1].

```
function (h, s, v) → (r, g, b)

h = h / 60
i = floor (i)
f = h - i
p = v*(1 - s)
q = v*(1 - s*f)
t = v*(1 - s*(1 - f))
case i of
        0: (r, g, b) = (v, t, p)
        1: (r, g, b) = (q, v, p)
        2: (r, g, b) = (p, v, t)
        3: (r, g, b) = (p, q, v)
        4: (r, g, b) = (t, p, v)
        5: (r, g, b) = (v, p, q)
end
```

Notes:
h is an angle between 0° and 360°
s is the saturation value set to some constant between 0 and 1 (unused in this application)
value is normalized to lie between 0 and 1
outputs, r, g and b all fall between 0 and 1.

(a)

(b)

Figure 4.6 Sticks image with false color applied to indicate the direction of the most prominent stick at each point. The hue applied is obtained from the direction of the most prominent length 15, thickness 1 sticks at each point. The colored circle visible in the image was superimposed on the raw image and processed along with the rest of the image; its color at various points on its diameter indicates the hue assigned to boundaries at corresponding orientations. The image shows a range of hues along curving lines, such as the fat boundaries near the top of the image. Image (a) is obtained by distributing hues evenly about the color circle; Image (b) is the result of warping the colormap to show a full spectrum along the broad boundary at the top of the image.

is possible with the colored images. Because of this revealing demonstration, we believe that the use of false color is a very promising technique with potential to significantly improve the capability of diagnostic imaging devices. False color allows two additional degrees of freedom in the display (only one of which is used here), which can be used to supply additional information to the user. Most importantly, the additional information can be introduced into the display or switched off without qualitatively changing the appearance of the scan. Further research is required to determine the best quantities to encode using false color.

4.5 Conclusion

This chapter has discussed the use of the Sticks algorithm to enhance images for boundary detection. The technique operates by applying a set of templates as a filter bank and retaining the largest filter output at each point as a test statistic. It has been shown that by modifying the length and thickness of the templates, the technique can be made more sensitive to thicker lines, or achieve a different trade-off between speckle suppression and the ability to follow tightly curving boundaries. We have also demonstrated a technique for estimating from the image itself the prior probability of a line of any orientation passing through each point, which results in greater speckle rejection and better performance of the detection procedure. Finally, we have presented a means of displaying the angle information at each point as a false color. This is an extremely promising idea because it allows for entirely new information to be incorporated into an image without affecting the gray level value of the original image.

Note that the class of rotating kernel detectors to which these algorithms belong is far broader than that which can be surveyed here. Lee and Rhodes [26, 27, 28, 29] and Hou and Bamberger [30, 31] have experimented with similar approaches. In our own work, we have used the median operation [43] in place of a sum, and obtained results similar to those produced by the Sticks algorithm. These methods have applicability in medical ultrasound imaging because of their ability to enhance the linear image features which correspond to tissue boundaries. They also may find applicability in other forms of

coherent imaging, such as microwave synthetic aperture imaging, because of the statistical and physical analogy between the speckle noise in these two imaging modalities.

CHAPTER 5

DETECTION IN RADIO FREQUENCY (RF) ULTRASOUND

5.1 Detection of Large Scatterers

The techniques studied to this point have been successful in facilitating computer detection of boundaries of interest in ultrasound images. The images studied in Chapters 3 and 4 were produced by non-coherent processing which makes the detection process less sensitive to deviations from the ideal behavior of the radio frequency (RF) signal. Under ideal circumstances, however, the loss of phase in the non-coherent processing can lead to a significant performance loss. In this chapter, we will attempt to estimate this performance loss and quantify the amount of distortion that a coherent system can tolerate. A successful coherent demodulation approach has the potential to significantly improve the boundary resolution capacity of a system by making it possible to detect more precisely the locations of boundaries that fall between resolution cells. Essentially, this detection would combine the stages of image formation and boundary detection.

The model for the RF trace is a signal of the form:

$$\begin{aligned} r(t) &= \sum_k \alpha_k p(t-T_k)\cos(\omega(t-T_k)) + \sum_l \beta_l p(t-T_l)\cos(\omega(t-T_l)) \\ &= n(t) + \sum_l \beta_l p(t-T_l)\cos(\omega(t-T_l)), \end{aligned} \tag{5.1}$$

where the diffuse reflectors' scattering strengths are denoted α_k, and the strengths of the specular reflectors are denoted β_k. Under the assumptions that scatterers are densely spaced and have independent, identically distributed scattering strengths, the resulting signal can be written as the superposition of Gaussian noise and reflected copies of the interrogating pulse from the specular scatterers.

True ultrasound traces deviate from this model in a number of ways. Notably, frequency-dependent pulse attenuation and non-linearities such as phase aberration in the interrogation process lead to distortion of the pulse shape. In addition, the initial phase of each trace is often uncertain because the transducer is manually positioned, a process which can easily lead to uncertainties in position on the order of a fraction of a wavelength (approximately 0.1 mm at 1.5 MHz). Finally, phase aberration leads to widening of the focal region and adds uncertainty to any estimate of transverse correlation. Signal processing approaches to counter these aberrating effects have not yet been successful, and such non-idealities invariably lead to suboptimal coherent detection.

5.2 RF Signal Model

If a large scatterer is located at depth z within a trace, the trace will have the form

$$r(t) = n(t) + \beta p(t - 2z/c)\cos(\omega\,(t - 2z/c)) \tag{5.2}$$

around time $t \approx 2z/c$, where c is the speed of sound, and

$$r(t) = n(t) \tag{5.3}$$

otherwise. As in Chapters 3 and 4, we assume that targets lie along roughly straight lines within the scanning coordinate system. Thus, when a sufficiently strong scatterer is present in one RF trace, the same structure will also be seen in nearby traces. For example, if a target is present at location (x_0, t_0) in the scan plane, then for values of x close to x_0, and some value of θ,

$$r(x,t) = n(x,t) + \beta p\left(t - T(x,\theta)\right)\cos\left(\omega t - \omega T(x,\theta) - \phi(x,0)\right), \tag{5.4}$$

where

$$T(x,\theta) = t_0 - \frac{2(x - x_0)}{c}\tan\theta \tag{5.5}$$

as shown in Figure 5.1, and $\phi(x,0)$ represents the initial phase of the pulse, which is in general unknown, and which may vary with x due to the uncertainty in transducer

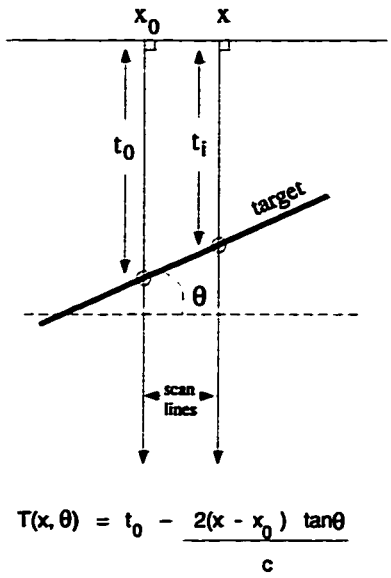

Figure 5.1 Imaging geometry, linear scanning.

positioning. Note that in a particular scanning geometry, the distance $x - x_0$ may be a function of depth (time), for example in a sector scan, where scan lines are spaced linearly in angle.

The Gaussian random process $n(x,t)$ is the sum of reflections from many small unresolvable scatterers within the resolution cell. Its correlation is approximately separable into axial and transverse correlations, with the t (axial) correlation due to intersymbol interference-like effects, and the x (transverse) correlation due to pulse diffraction. In this discussion, we will consider only noise correlation in the axial direction, but in principle, the extension to detection in a speckle field with two-dimensional correlation is straightforward.

5.3 Detection Environment

The detection environment in which RF routines must operate is more uncertain than that of processed images because, in addition to the effects of noise coloration, the signals are degraded by such effects such as phase aberration and frequency dependent attenuation. These can lead to significant and currently unpredictable loss of focus and

pulse distortion. In this section, we explore the effects of a few types of non-idealities in RF detection and compare their effects on detector performance.

5.3.1 White noise

In the white noise case, the observed signal over each of N lines is given by

$$x(t,i) = n(t,i) + p(t - T_i)\cos(\phi_i + \omega t), \quad i = 1, 2, \ldots, N \tag{5.6}$$

where $n(t)$ is a white noise process and ϕ_i is a phase offset on the ith scan line due to uncertainty in the initial position of the transducer. When ϕ_i is non-zero, it is generally unknown.

The detection scenario is analogous to a communication system of N channels. The optimal detection statistic is the sum of terms obtained by demodulation and matched filtering on each channel:

$$\Lambda(x) = \sum_i \int_{T_i} p(t - T_i)\left[(x(t,i)\cos(\omega t)) * LPF(t)\right] dt, \tag{5.7}$$

where $*LPF(t)$ denotes convolution with a low-pass filter to remove double frequency terms in the demodulation, and the integral in (5.7) is performed over all time, but effectively limited to a region around T_i where $p(t - T_i)$ has its energy. This sum of integrals is a generalization of the matched filer to the multichannel detection problem.

In (5.7), the signal is demodulated using only the in-phase component, which yields an optimal detector when $\phi = 0$; non-zero values of ϕ lead to suboptimal performance of the coherent detector. In this case, optimal detection is performed with a quadrature detector sensitive to energy at the modulation frequency, but insensitive to phase errors:

$$\begin{aligned}\Lambda(x) = \sum_i &\left| \int_{T_i} p(t - T_i)\left[x(t,i)\cos(\omega t) * \mathrm{LPF}(t)\right] dt \right|^2 \\ &+ \left| \int_{T_i} p(t - T_i)\left[x(t,i)\sin(\omega t) * \mathrm{LPF}(t)\right] dt \right|^2,\end{aligned} \tag{5.8}$$

where the integrals are in the vicinity of T_i, as in (5.7), and $\mathrm{LPF}(t)$ is a low-pass filter used to remove double frequency terms after quadrature demodulation. The Sticks detector

described in Chapters 3 and 4 is essentially the maximum of a set of sums of absolute values, rather than magnitudes squared:

$$\Lambda(x) = \sum_i \left| \int_{T_i} p(t - T_i) \left[x(t,i) \cos(\omega t) * \mathrm{LPF}(t) \right] dt \right| + \left| \int_{T_i} p(t - T_i) \left[x(t,i) \sin(\omega t) * \mathrm{LPF}(t) \right] dt \right|, \tag{5.9}$$

since ultrasound images are usually formed from magnitude rather than intensity images.

5.3.2 Colored noise

In the more general case where the received signal has axial coloration, a prewhitening filter must be used. In this case, the detection statistic is given by

$$\Lambda(x) = \sum_i \int_{T_i} \tilde{p}(t - T_i) \tilde{x}(t,i) \cos(\omega t) dt, \tag{5.10}$$

where

$$\tilde{p}(t) = \int h^{-1}(\tau) p(t - \tau) d\tau, \tag{5.11}$$

$$\tilde{x}(t,i) = \int h^{-1}(\tau) x(t - \tau, i) d\tau, \tag{5.12}$$

and $h^{-1}(t)$ is the whitening filter for the noise, i.e.,

$$\tilde{n}(t) = \int h^{-1}(\tau) n(t - \tau) d\tau \tag{5.13}$$

is a Gaussian white noise process.

When the data are delayed by an unknown phase, a quadrature detector must again be used:

$$\Lambda(x) = \sum_i \left| \int_{T_i} p(t - T_i) [x(t,i) \cos(\omega t) * \mathrm{LPF}(t) * h^{-1}] dt \right|^2 + \left| \int_{T_i} p(t - T_i) [x(t,i) \sin(\omega t) * \mathrm{LPF}(t) * h^{-1}] dt \right|^2, \tag{5.14}$$

where, as before, $*\text{LPF}(t)$ denotes the filter used to remove double frequency terms, and $h^{-1}(t)$ is the whitening filter, applied to the pulse, as in (5.11), as well as to the received signal.

5.3.3 Pulse distortion

Due to non-linearities in the propagation of sound waves in tissue, ultrasound systems have to contend with pulse distortion. Pulse distortion is simulated by adding in a filtered version of the pulse instead of a pure version, while detection is still performed by correlating with an unfiltered pulse. Coherent and energy detectors are identical in form to those in (5.7) and (5.8).

Pulse distortion can be modeled more generally as a non-linear process by which pulse energy is shifted to higher harmonic frequencies. This has the effect of distributing some signal energy to other frequencies within the passband of the demodulator and other energy into the stopband, where it is severely attenuated by the demodulation process. Thus pulse distortion can be considered as a problem of energy loss as well as spectral modification of the pulse, and true detector performance is in fact worse than indicated below.

5.3.4 Comparison of detector power by simulation

These detection scenarios were simulated to produce receiver operating characteristic (ROC) curves which measure the relative performances of the different detectors. For each simulation, 100 random scans were generated, with and without a target, according to the model in (5.2) and (5.3). Targets were assumed to appear at a known location at one of 20 possible orientations across the scan lines. For each noise realization, detector outputs were produced for each target orientation, leading to a total of 20 detection statistics per simulation. ROC curves were obtained by thresholding the set of all the detection statistics and plotting for each threshold the probability that an output value exceeding that threshold corresponds to a true detection versus the probability that it corresponds to a false alarm. The simulation parameters were set to be typical of ultrasound imaging systems (carrier frequency of 1 MHz, sampling rate 25 MHz, pulse

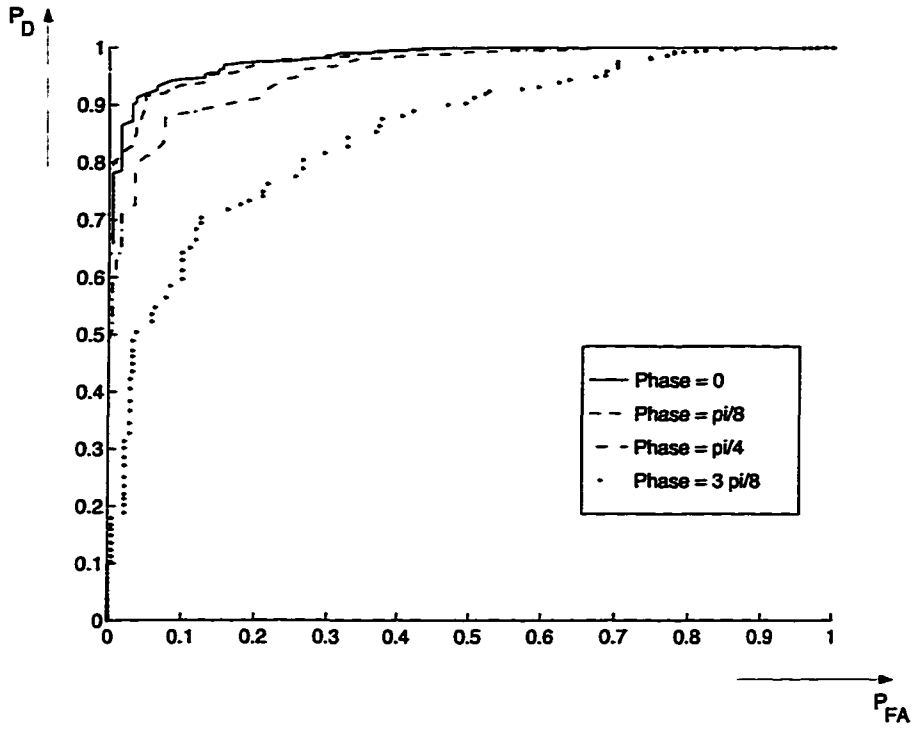

Figure 5.2 ROC curves showing the effect of phase uncertainty on detection in white noise.

duration 20 μ sec). The signal to noise ratio was set empirically at -7dB for all simulations so that variations in ROC curves could be easily compared. As in earlier simulations, the detector was told the target location and the angles at which the target could appear. In the case of techniques dependent on statistical information, the noise statistics were provided to the detectors.

Figure 5.2 shows the ROC curves resulting from simulations of the coherent detector at varying degrees of phase coherence with respect to the target. Phase errors can arise from slight motion of the transducer during a scan or by tissue motion due to, for example, respiration. Motion on the order of a fraction of a wavelength can lead to serious loss in detector power. Errors in sensor positioning also occur in synthetic aperture radar (SAR), and can potentially be corrected by a number of *auto-focus* algorithms that have been developed for use with SAR [50].

Figure 5.3 shows the ROC curves for the coherent detector, the quadrature energy detector and the Sticks detector in white noise. The coherent detector significantly outperforms the energy and Sticks detectors, but the energy and Sticks detector perform

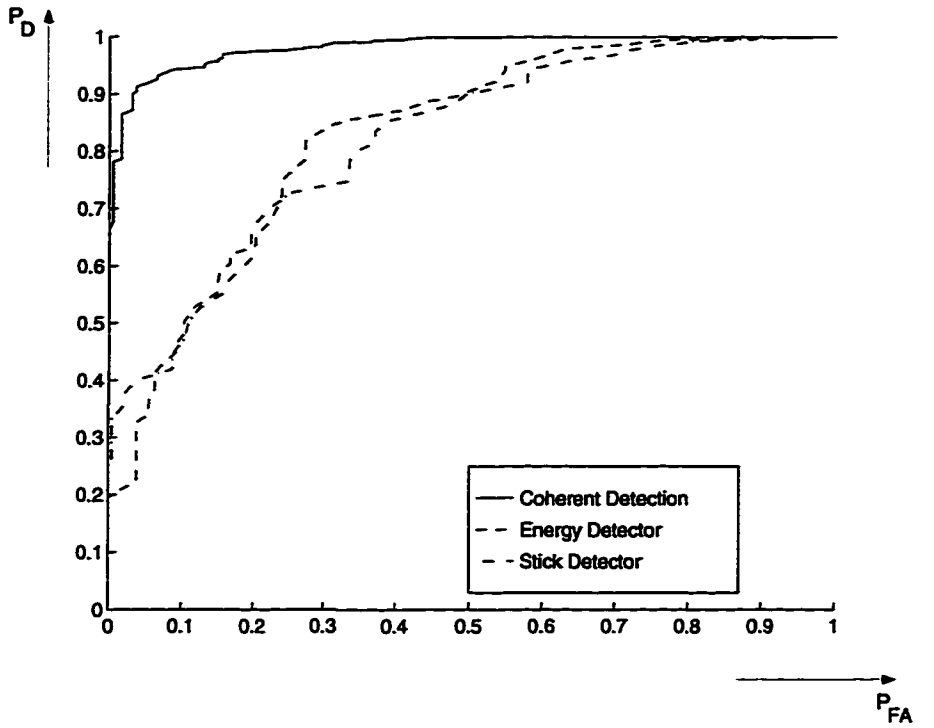

Figure 5.3 ROC curves showing performance gap between coherent detector and energy detector in white noise.

comparably. Figure 5.4 shows ROC curves for colored noise simulations. As in the simulations in Chapter 3, the prewhitening filter improved performance over coherent detection in colored noise and, as in the white noise simulation, the energy and Sticks detectors are far inferior to the coherent detectors.

Figures 5.5 and 5.6 show ROC curves for simulations of ultrasound pulse distortion in white and colored noise, respectively. Pulse distortion was simulated by convolving the received pulse with a copy of itself, approximately doubling its length, but leaving its Gaussian shape intact. Detection was done by correlating with an undistorted copy of the pulse; in ultrasound the true nature of pulse distortion is unknown. In both cases, again, coherent processing, even with a mismatched template, is superior to energy detection.

Finally, Figures 5.7 and 5.8 show the effect of a frequency shift on coherent and envelope detection in white and colored noise. This form of pulse distortion is common in ultrasound imaging, as tissue is a dispersive medium, attenuating higher frequencies more than lower ones which results in a shift of the pulse's center frequency. For this figure, the frequency of demodulation was set to 80% of the frequency of modulation, and curves

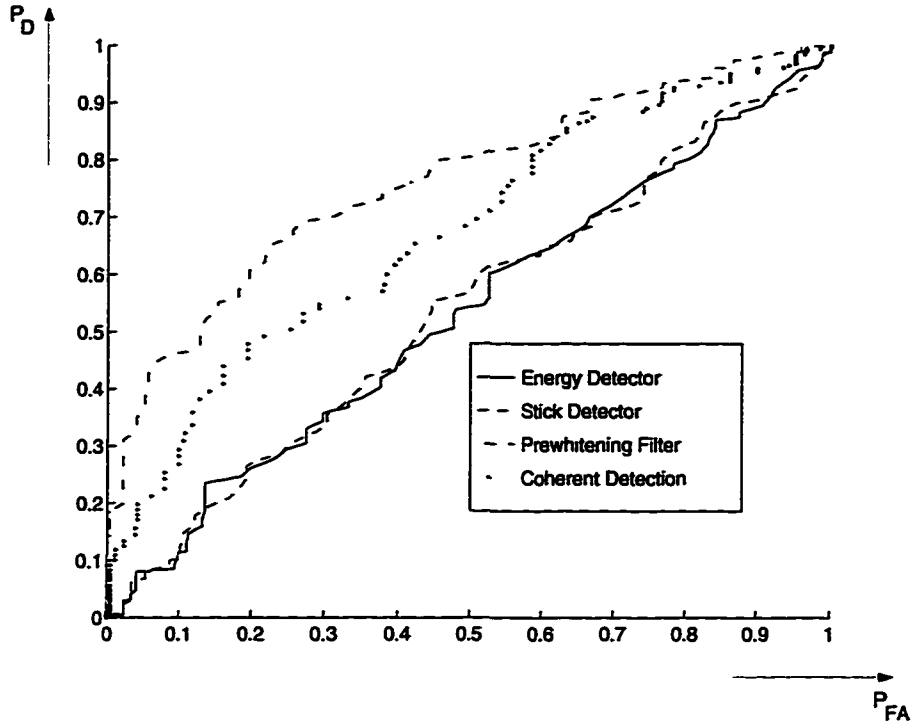

Figure 5.4 ROC curves showing effect of noise coloration on detector performance.

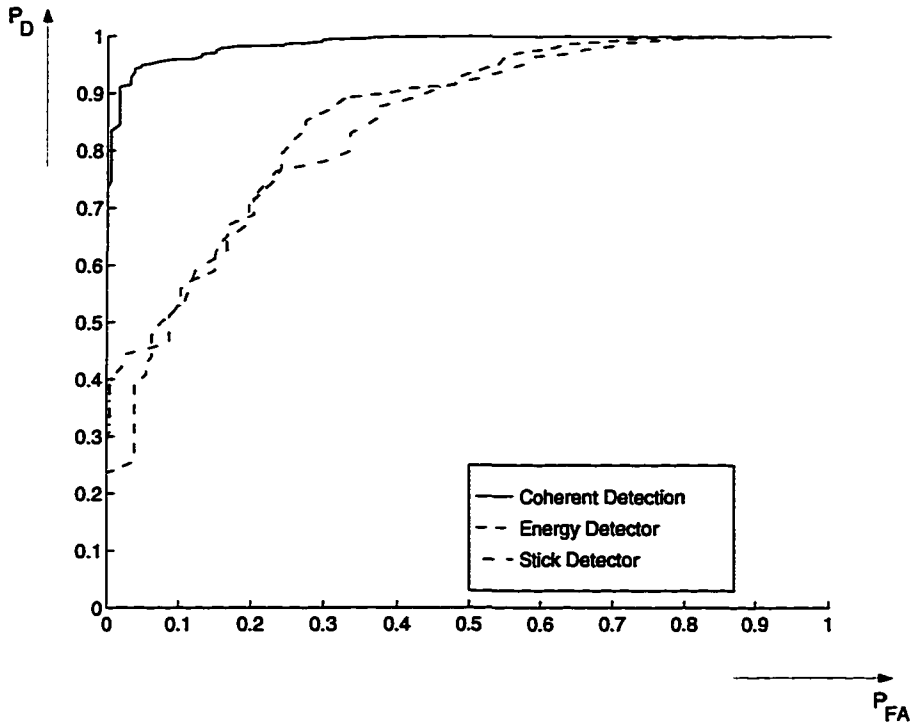

Figure 5.5 ROC curves showing effect of pulse distortion on detector performance in white noise.

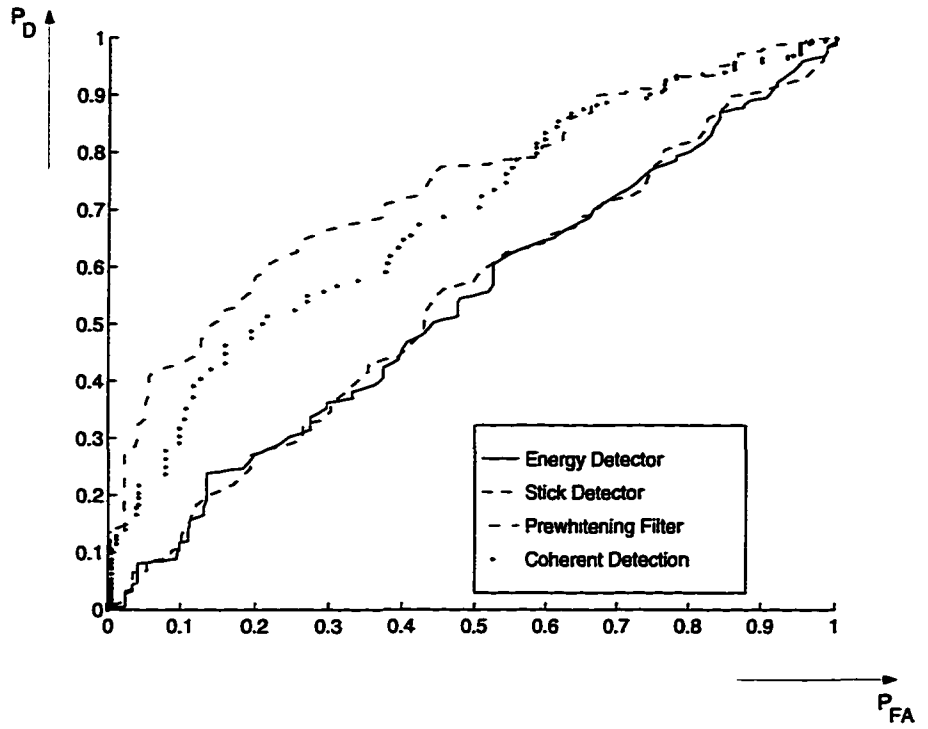

Figure 5.6 ROC curves showing effect of pulse distortion on detector performance in colored noise.

were plotted for a coherent detector and an energy detector. In the white noise case, the energy and Stick detectors offered an advantage over the frequency-mismatched coherent detector, but in colored noise, the coherent detector outperformed the noncoherent detector.

5.4 Conclusion

The simulations presented here have shown that coherent detection of boundaries in RF ultrasound is a practical goal. While phase errors can lead to significant performance losses, the coherent detectors were somewhat less sensitive to the pulse distortions and noise colorations simulated here. In contrast, the energy detector yielded much lower performance, and was itself more sensitive than expected to the distortions simulated. In spite of the uncertain statistical environment of RF ultrasound, the non-coherent processing typically done to produce B-mode ultrasound appears to involve significant sacrifices in performance.

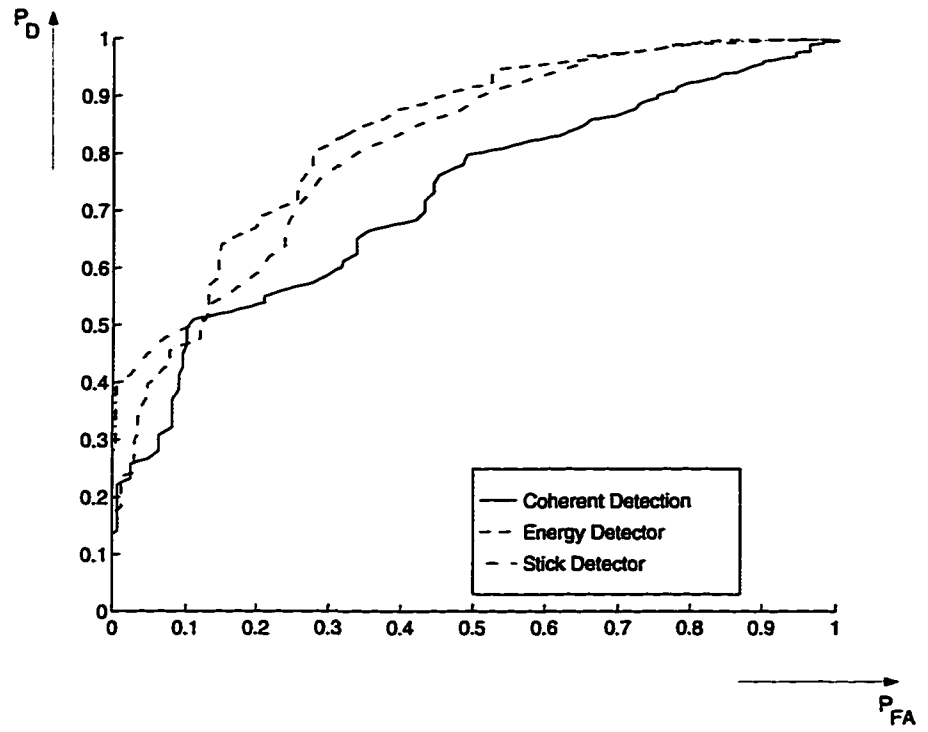

Figure 5.7 ROC curves showing effect of center frequency shift on detector performance in white noise.

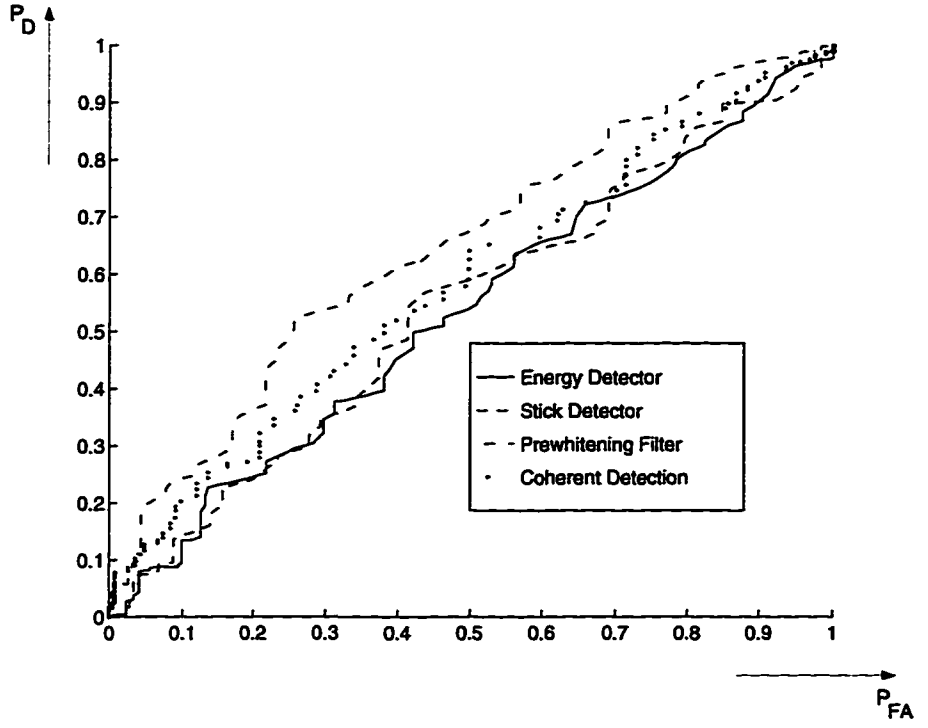

Figure 5.8 ROC curves showing effect of center frequency shift on detector performance in colored noise.

CHAPTER 6

CONCLUSION

6.1 Summary of Research Results

This thesis has presented the results of a comprehensive study of the problem of boundary detection in medical ultrasound. In many cases, the boundary detection approaches require knowledge of the statistical behavior of ultrasonic backscatter; these statistics are derived from physical principles, and a plausible probability density function for images is derived.

Boundaries between tissue layers are surfaces which are observed in cross-section; when an image is formed, they have the appearance of curving lines against a dark background. The curves are broad enough that, in the vicinity of each boundary point, they can be approximated by straight-line segments of some orientation. This simplification allows the problem to be reformulated as a problem of line detection, in which a composite hypothesis test is used to distinguish which orientation segment (if any) is present at each pixel. A number of different detection rules were surveyed, including the optimal likelihood ratio test, a test based on the deflection criterion, and "Sticks" techniques, template-projection based tests reminiscent of matched filtering. These detection rules were compared by simulation under controlled circumstances, and it was found that the Sticks and deflection approaches were nearly optimal in uncorrelated speckle, but Sticks was significantly suboptimal in colored speckle. In the case of colored speckle, a prewhitening filter can be used in conjunction with the Sticks technique to improve performance to nearly that of the deflection detector. The prewhitened Sticks approach, however, is highly sensitive to errors in the estimation of noise parameters and signal form.

In contrast, the basic Sticks technique was shown to be a practical image processing technique, and to have many useful extensions. For example, we presented a technique for enhancing boundary detection by estimation of the most likely angles at each point, and a technique of coding the orientation of the angle of the most prominent line segment at each point onto a false color. This allows the display of additional information without obscuring the image's gray levels.

Finally, we have presented additional simulations which suggest that coherent processing of RF ultrasound is a practical goal with the potential to dramatically improve the performance of mathematical detectors of line segments in medical ultrasound imagery.

6.2 Suggestions for Future Work

The ideas in this dissertation led to many interesting ideas on which work should be continued. Some of these are listed below:

6.2.1 Experimental verification of statistical analysis

The statistical discussion in Chapter 2 is a powerful framework within which many problems may be formulated. In particular, the variance of image moment estimates has real applicability to many current approaches to tissue characterization. Experimental validation of the results in Chapter 2 would make them even more valuable. The validity of the statistical model presented for image intensity is somewhat conjectural at this time, especially for points where a target is visible, or where scatterer density is low. Ideas such as modeling backscatter with a K-distribution are under discussion in the literature [10, 51] but little experimental data have been given to verify the model.

6.2.2 Sequential detection

In Chapter 4 the trade-offs of operator size were quantified, and it was determined that it is highly desirable to match the detection template as well as possible to the targets of interest. Practically, this can be accomplished by performing hypothesis testing at each point by a sequential procedure [33]. This would involve performing detection with

operators of several different scales and using some criterion to decide at which scale to make the final detection. This is reminiscent of the adaptive size median filters described in [44, 43].

6.2.3 Adaptive filtering

The rotating template approach to boundary detection is essentially a two-dimensional adaptive filter allowed to adapt within a small set of possible orientations. This approach has the advantage of being efficiently implementable with a bank of filters, but may be overly constrained with respect to other optimality criteria. Further work in identifying reasonable criteria and exploring gradient-based techniques for optimizing the template at each point may lead to useful techniques of ultrasound image enhancement. This idea may also be implemented in a manner similar to those in [43, 44].

6.2.4 Pixel- or scale-recursive algorithms

For application to large images, or in a sequential detection setting where detection is performed using successively larger templates, the Sticks technique can be implemented with a fast algorithm which exploits certain properties of the templates. For example, each length N projection as in (3.1) is the sum of a length $N-2$ projection and the intensities of two additional pixels. Similarly, stick projections can also be recursively computed from previously computed stick projections at adjacent locations. These recursive computations can result in significant computational savings.

6.2.5 Edge linking

6.2.5.1 Dynamic programming

In some cases where a binary edge map is desired, the enhanced images produced by the Sticks technique may be insufficient. In these cases, an edge linking approach such as that described in [52] may be able to produce smooth lines across discontinuities in the Sticks processed images.

6.2.5.2 Active contour models

Along similar lines, the approach of active contours or Snakes has been used to connect possibly discontinuous boundaries in images. Chalana et al. [53] have used this approach to detect cardiac boundaries in echographic sequences. Their approach has great potential, but requires user input to specify a starting segment for the algorithm. The Sticks technique is complementary to this approach.

6.2.6 Multiscale ultrasound tissue characterization

One idea that surfaced in the course of this research is the idea that ultrasound scattering is fundamentally a multiscale phenomenon. This is because ultrasound interrogation inherently separates the scatterer population into three regimes: scatterers much larger than a wavelength, those much smaller than a wavelength, and those about the same size as a wavelength. Large scatterers reflect ultrasound coherently, while smaller scatterers give rise to diffuse speckle noise. Scatterers about the same size as a wavelength, however, are ignored by this scattering model. The relative sizes of populations of different scale scatterers are, however, of fundmental importance in tissue characterization.

By the use of different frequencies of interrogation, the properties of intermediate size scatterers can be investigated. Furthermore, the multiscale interpretation of scattering may lead to a general theory of multispectral ultrasound image formation, new pulse designs based on wavelet functions, and important contributions to the understanding of ultrasound scattering.

REFERENCES

[1] J. D. Foley, A. van Dam, S. K. Feiner, and J. F. Hughes, *Computer Graphics: Principles and Practice*, Addison-Wesley, Reading, MA, 2nd ed., 1987, p. 593.

[2] J. W. Goodman, "Statistical properties of laser speckle patterns," in *Laser Speckle and Related Phenomena*, J. C. Dainty, Ed., number 9 in Topics in Applied Physics, chapter 2, pp. 9–77. Springer-Verlag, Berlin, 1977.

[3] C. B. Burckhardt, "Speckle in ultrasound B-mode scans," *IEEE Transactions on Sonics and Ultrasonics*, vol. SU-25, no. 1, pp. 1–6, January 1978.

[4] R. F. Wagner, M. F. Insana, and S. W. Smith, "Fundamental correlation lengths of coherent speckle in medical ultrasonic images," *IEEE Transactions on Ultrasonics, Ferroelectrics, and Frequency Control*, vol. 35, no. 1, pp. 34–44, January 1988.

[5] R. F. Wagner, M. F. Insana, and D. G. Brown, "Statistical properties of radio-frequency and envelope-detected signals with applications to medical ultrasound," *Journal of the Optical Society of America*, vol. 4, no. 5, pp. 910 – 922, May 1987.

[6] R. E. Blahut, *Theory of Remote Surveillance*, Manuscript in Progress, March 1993.

[7] G. S. Kino, *Acoustic Waves: Devices, Imaging and Analog Signal Processing*, Prentice Hall, Englewood Cliffs, NJ, 1987.

[8] K. S. Miller, *Complex Stochastic Processes*, Addison-Wesley, Reading, MA, 1974.

[9] G. E. Sleefe and P. P. Lele, "Tissue characterization based on scatterer number density estimation," *IEEE Transactions on Ultrasonics, Ferroelectrics and Frequency Control*, vol. 35, no. 6, pp. 749–757, November 1988.

[10] P. M. Shankar, J. M. Reid, H. Ortega, C. W. Piccoli, and B. B. Goldberg, "Use of non-Rayleigh statistics for the identification of tumors in ultrasonic B-scans of the breast," *IEEE Transactions on Medical Imaging*, vol. 12, no. 4, pp. 687–692, December 1993.

[11] E. Jakeman and P. Pusey, "A model for non-rayleigh sea echo," *IEEE Transactions on Antennas and Propagation*, vol. AP-24, no. 6, pp. 806–814, November 1976.

[12] S. Watts, "Radar detection prediction in sea clutter using the compound K-distribution model," *IEE Proceedings*, vol. 132, Pt. F, no. 7, pp. 613–620, December 1985.

[13] E. Jakeman and R. Tough, "Generalized K distribution: a statistical model for weak scattering," *Journal of the Optical Society of America*, vol. 4, no. 9, pp. 1764–1772, September 1987.

[14] R. N. Czerwinski, D. L. Jones, and W. D. O'Brien, Jr., "An approach to boundary detection in ultrasound imaging," in *1993 IEEE Ultrasonics Symposium Proceedings*, Baltimore, MD, November 1993.

[15] R. F. Wagner, S. W. Smith, J. M. Sandrik, and H. Lopez, "Statistics of speckle in ultrasound B-scans," *IEEE Transactions on Sonics and Ultrasonics*, vol. 30, no. 3, pp. 156–163, May 1983.

[16] D. C. Munson, Jr. and J. L. C. Sanz, "Image reconstruction from frequency-offset Fourier data," *Proceedings of the IEEE*, vol. 72, no. 6, pp. 661–669, June 1984.

[17] R. C. Molthen, P. M. Shankar, J. M. Reid, V. Genis, and L. Vergara-Dominguez, "Ultrasound echo evaluation by K-distribution," in *Proceedings of the 1993 IEEE Ultrasonics Symposium*, Baltimore, MD, October 31 - November 3 1993.

[18] D. T. Kuan, A. A. Sawchuk, T. C. Strand, and P. Chavel, "Adaptive restoration of images with speckle," *IEEE Transactions on Signal Processing*, vol. ASSP-35, no. 3, pp. 373–383, March 1987.

[19] K. D. Donohue, "Maximum likelihood estimation of A-scan amplitudes for coherent targets in media of unresolvable scatterers," *IEEE Transactions on Ultrasonics, Ferroelectrics, and Frequency Control*, vol. 39, no. 3, pp. 422–431, May 1992.

[20] M. R. Zaman and C. R. Moloney, "A comparison of adaptive filters for edge-preserving smoothing of speckle noise," in *Proceedings of the IEEE International Conference on Acoustics, Speech and Signal Processing — ICASSP '93*, 1993, pp. V–77–V–80.

[21] A. C. Bovik and D. C. Munson, Jr., "Boundary detection in speckle images," in *Proceedings of the IEEE International Conference on Acoustics, Speech and Signal Processing — ICASSP '85*, Tampa, FL, 1985, pp. 893–896.

[22] A. C. Bovik, "On detecting edges in speckle imagery," *IEEE Transactions on Signal Processing*, vol. 36, no. 10, pp. 1618–1627, October 1988.

[23] K. D. Donohue, M. Rahmati, L. G. Hassebrook, and P. Gopalakrishnan, "Parametric and nonparametric edge detection for speckle degraded images," *Optical Engineering*, August 1993.

[24] M. Tur, K. C. Chin, and J. W. Goodman, "When is speckle noise multiplicative?," *Applied Optics*, vol. 21, no. 7, pp. 1157–1159, April 1982.

[25] R. O. Duda and P. E. Hart, "Use of the Hough transform to detect lines and curves in pictures," *Communications of the ACM*, vol. 15, no. 1, pp. 11–15, January 1972.

[26] Y. K. Lee and W. T. Rhodes, "Feature detection and enhancement by a rotating kernel min-max transformation," in *Hybrid Image and Signal Processing II*, Franklin T. Luk, Ed., Proc. SPIE 1297, 1990, pp. 154–159.

[27] Y. K. Lee and W. T. Rhodes, "Scale- and rotation-invariant pattern recognition by a rotating kernel min-max transformation," in *Optical Information-Processing Systems and Architectures II*, Franklin T. Luk, Ed., Proc. SPIE 1347, 1990, pp. 146–155.

[28] Y. K. Lee and W. T. Rhodes, "Nonlinear image processing by a rotating kernel transformation," *Optics Letters*, vol. 15, no. 23, pp. 1383–1385, December 1990.

[29] Y. K. Lee and W. T. Rhodes, "Invariant pattern recognition using angular signature functions," *Applied Optics*, vol. 32, no. 23, pp. 4372–4377, 10 August 1993.

[30] J. Hou and R. Bamberger, "Orientation selective operators for ridge, valley, edge, and line detection in imagery," in *Proceedings of the IEEE International Conference on Acoustics, Speech and Signal Processing — ICASSP '94*, Adelaide, Australia, May 1994, pp. V–25–V–28.

[31] J. Hou and R. Bamberger, "A robust system for lineament analysis of aero-magnetic imagery using orientation analysis and edge linking," in *Proceedings of the IEEE International Conference on Image Processing — ICIP '94*, Austin, TX, November 1994, pp. I–963 – I–967.

[32] R. N. Czerwinski, D. L. Jones, and W. D. O'Brien, Jr., "Edge detection in ultrasound speckle noise," in *Proceedings of the IEEE International Conference on Image Processing — ICIP '94*, Austin, TX, November 1994.

[33] H. V. Poor, *An Introduction to Signal Detection and Estimation*, Springer-Verlag, New York, 1988.

[34] H. Stark and J. W. Woods, *Probability, Random Processes, and Estimation Theory for Engineers*, Prentice Hall, Englewood Cliffs, NJ, 1986.

[35] C. R. Baker, "Optimum quadratic detection of a random vector in Gaussian noise," *IEEE Transactions on Communications*, vol. COM-14, pp. 802–805, December 1966.

[36] B. Picinbono and P. Duvaut, "Optimal linear-quadratic systems for detection and estimation," *IEEE Transactions on Information Theory*, vol. 34, no. 2, pp. 304–311, March 1988.

[37] H. L. Van Trees, *Detection, Estimation, and Modulation Theory, Part I*, John Wiley and Sons, New York, 1968.

[38] R. N. Czerwinski, D. L. Jones, and W. D. O'Brien, Jr., "A comparison of detection rules for lines and boundaries in acoustic speckle," in *Presented at the Twenty-Second International Symposium on Acoustic Imaging*, Florence, Italy, September 1995.

[39] R. N. Czerwinski, D. L. Jones, and W. D. O'Brien, Jr., "Decision directed line detection with application to medical ultrasound," in *Proceedings of the 1996 SPIE International Symposium on Medical Imaging*, Newport Beach, CA, February 1996.

[40] W. H. Press, B. P. Flannery, S. A. Teukolsky, and W. T. Vetterling, *Numerical Recipes in C*, Cambridge University Press, Cambridge, UK, 1988.

[41] E. Anderson et al., *LAPACK Users' Guide*, SIAM, Philadelphia, PA, 1993.

[42] The MathWorks Inc., *Matlab External Interface Guide*, The MathWorks, Inc., Natick, MA, 1993.

[43] R. N. Czerwinski, D. L. Jones, and W. D. O'Brien, Jr., "Ultrasound speckle reduction by directional median filtering," in *Proceedings of the IEEE International Conference on Image Processing — ICIP '95*, Washington, DC, October 1995.

[44] T. Loupas, W. N. McDicken, and P. L. Allan, "An adaptive weighted median filter for speckle suppression in medical ultrasonic images," *IEEE Transactions on Circuits and Systems*, vol. 36, no. 1, pp. 129–135, January 1989.

[45] J. Canny, "A computational approach to edge detection," *IEEE Transactions on Pattern Analysis and Machine Intelligence*, vol. PAMI-8, no. 6, pp. 679–698, November 1986.

[46] R. C. Gonzalez and R. E. Woods, *Digital Image Processing*, Addison-Wesley, Reading, MA, 1992.

[47] T. A. Tuthill, R. H. Sperry, and K. J. Parker, "Deviations from Rayleigh statistics in ultrasonic speckle," *Ultrasonic Imaging*, vol. 10, no. 1, pp. 81–89, January 1988.

[48] R. O. Duda and P. E. Hart, *Pattern Classification and Scene Analysis*, Wiley, New York, 1973.

[49] R. Momenan, R. F. Wagner, B. S. Garra, M. H. Loew, and M. F. Insana, "Image staining and differential diagnosis of ultrasound scans based on the mahalanobis distance," *IEEE Transactions on Medical Imaging*, vol. 13, no. 1, pp. 37–47, March 1994.

[50] C. V. Jakowatz, D. E. Wahl, P. H. Eichel, D. C. Ghiglia, and P. A. Thompson, *Spotlight-Mode Synthetic Aperture Radar: A Signal Processing Approach*, Kluwer Academic Publishers, Boston, MA, 1996.

[51] V. Dutt and J. F. Greenleaf, "Statistics of the log-compressed echo envelope," *Journal of the Acoustical Society of America*, Submitted.

[52] A. Waks, *Robust Framework for Object Boundary Detection*, Ph.D. dissertation, Drexel University, 1991.

[53] V. Chalana, D. Linker, D. R. Haynor, and Y. Kim, "A multiple active contour model for cardiac boundary detection on echographic sequences," Preprint.

APPENDIX A

MEASURES OPERATING MANUAL

```
*                                                    *
* Measures Operating Manual (MOM)                    *
* Revision 0.8                                       *
*                                                    *
* Rich Czerwinski                                    *
* University of Illinois                             *
* May 10, 1994                                       *
*                                                    *
* Touched up and revised slightly for                *
* inclusion in prelim document.                      *
* rnc March 9, 1995                                  *
```

1.0 Introduction

This is a guide to the software used in the automatic estimation of fat and muscle thicknesses in the Beef Ultrasound Grading System (BUGS) project [1], [2], ongoing at the University of Illinois.

The software described in this document has all been developed for the specific purpose of facilitating the boundary detection. Some of this work has been published in the open literature [3], [4] and more publications have been submitted for peer review [5], [6].

The software is of three varieties:

i) stand-alone code written in C

ii) Matlab m-files which are interpreted by Matlab, a commercial software package sold by The MathWorks, Natick, MA.

iii) scripts which execute a number of C programs, unix commands or Matlab m-files in batch mode.

The m-files will be translated into C code at some future date, at which point the image analysis software will be completely stand-alone (i.e., will not require the presence of commercial software.)

2.0 Input/Output

2.1 Preprocessing

The BUGS system collects a large amount of data from each carcass. Each scan is done with two transducers, each of which collects data at each of the various gain settings. The Measures programs do not yet operate on RF data; instead the raw data must be processed into images via the following procedure:

i) extract a-lines,

ii) Hilbert transformation,

iii) time-gain compensation,

iv) spatial transformation (i.e., displaying pixels in their appropriate physical position, using the transducer position information collected at scan time),

v) compounding images from left and right transducers, so an entire half carcass can be seen in a single image.

The preprocessing and naming convention of RF data files is discussed in [7].

2.2 Input Files

2.2.1 Image files

The input image files required by the measures programs are stored in

(horizontal scans)
/bugs/images_rich/anml_xxx/cold/c?cgc???.pgm
/bugs/images_rich/anml_xxx/hide_on/n?cgc???.pgm
/bugs/images_rich/anml_xxx/hide_off/f?cgc???.pgm,

(skin scans)
/bugs/images_rich/anml_xxx/cold/cs?gc???.pgm
/bugs/images_rich/anml_xxx/hide_on/ns?gc???.pgm
/bugs/images_rich/anml_xxx/hide_off/fs?gc???.pgm,

where the unix wild card character '?' shows where the different files' names differ. The 'cgc' string appearing in all the file names indicates a compounded left/right transducer image, with time-gain compensation.

2.2.2 Position files

Every horizontal image file is accompanied by a position file which indicates the absolute positions of the image with respect to the carcass spine. The position files are found in
/bugs/images_rich/anml_xxx/cold/c?cgc???.pos
/bugs/images_rich/anml_xxx/hide_on/n?cgc???.pos
/bugs/images_rich/anml_xxx/hide_off/f?cgc???.pos .

2.3 Output Files

The Measures routines produce an output file
/bugs/results/measures-xxx,
which is a listing of animal numbers, carcass ID numbers, and measurements, which is suitable for processing using SAS.

A copy of the measures output file is stored compressed in
/home/wdo/rnc/analysis/working/measures_xxx.Z
for backup purposes.

An error file
/home/wdo/rnc/analysis/errors_xxx.Z
can be produced by directing stderr to a file while running the script. The error file is useful in determining if the script has run to completion, or if some files need to be rerun.

3.0 Measures Files

3.1 C Files

The following are the executable C files used in estimating fat and muscle thicknesses:

/home/wdo/rnc/analysis/cfiles/pgmchar_to_sun
    -- Convert pgm format to sunraster.

/home/wdo/rnc/analysis/cfiles/sunshiftup
    -- Shift image columns up so the skin surface is in row 0.

/home/wdo/rnc/analysis/cfiles/sticks
    -- Image line enhancement program as described in [3].

/home/wdo/rnc/analysis/cfiles/sun_to_ml
    -- Convert sunraster image into Matlab readable format.

/home/wdo/rnc/analysis/cfiles/slices
    -- Extract five, ten and fifteen cm vertical slices and
       write to a Matlab readable file.

```
/home/wdo/rnc/analysis/cfiles/number
     -- Extract animal id information from position file and
        store it so that info is available to a Matlab m-file
        at a later time.
/home/wdo/rnc/analysis/cfiles/one_stika
     -- Modified Sticks algorithm used in processing skin scans.
/home/wdo/rnc/analysis/cfiles/one_stikb
     -- Ditto above.
```

The source code for these programs is found in the files listed below. Indented are the names of the files that must be compiled externally and linked with the main program:

```
/home/wdo/rnc/analysis/cfiles/sources/pgmchar_to_sun.c
     /home/wdo/rnc/analysis/cfiles/sources/jmast.c
     /home/wdo/rnc/analysis/cfiles/sources/sunraster.c
/home/wdo/rnc/analysis/cfiles/sunshiftup.c
     /home/wdo/rnc/analysis/cfiles/sources/jmast.c
     /home/wdo/rnc/analysis/cfiles/sources/sunraster.c
/home/wdo/rnc/analysis/cfiles/sticks.c
     /home/wdo/rnc/analysis/cfiles/sources/jmast.c
     /home/wdo/rnc/analysis/cfiles/sources/sunraster.c
/home/wdo/rnc/analysis/cfiles/sun_to_ml.c
     /home/wdo/rnc/analysis/cfiles/sources/jmast.c
     /home/wdo/rnc/analysis/cfiles/sources/sunraster.c
     /home/wdo/rnc/analysis/cfiles/sources/savemat.c
/home/wdo/rnc/analysis/cfiles/slices.c
     /home/wdo/rnc/analysis/cfiles/sources/savemat.c
/home/wdo/rnc/analysis/cfiles/number.c
     /home/wdo/rnc/analysis/cfiles/sources/savemat.c
/home/wdo/rnc/analysis/cfiles/one_stika.c
```

/home/wdo/rnc/analysis/cfiles/sources/jmast.c

/home/wdo/rnc/analysis/cfiles/sources/sunraster.c

/home/wdo/rnc/analysis/cfiles/sources/savemat.c

/home/wdo/rnc/analysis/cfiles/one_stikb.c

/home/wdo/rnc/analysis/cfiles/sources/jmast.c

/home/wdo/rnc/analysis/cfiles/sources/sunraster.c

/home/wdo/rnc/analysis/cfiles/sources/savemat.c

The externally compiled files contain functions needed to save sunraster files, and Matlab files.

3.2 M-files

3.2.1 Primary processing programs

The following files run under Matlab in batch mode, invoked directly from the unix shell:

/home/wdo/rnc/analysis/mfiles/cold.m

-- Process cold files.

/home/wdo/rnc/analysis/mfiles/hideon.m

-- Process hide on files.

/home/wdo/rnc/analysis/mfiles/hideoff.m

-- Process hide off files.

3.2.2 Auxiliary files

The following files contain functions called by the m-files listed in section 3.2.1 :

/home/wdo/rnc/analysis/mfiles/first_peak.m

-- Find location of first peak in a sequence of data past a given point. Locations of peaks are obtained from maxes.m, described below.

/home/wdo/rnc/analysis/mfiles/horiz_thick.m

-- Find fat and muscle thickness given a vertical

```
        cross section, and fat and muscle thickness
        mean and standard deviation.  Works by finding
        the location of the local maximum of greatest
        value within a range defined by
        (skin position + fat thick mean +/- two standard deviations)
        for fat and
        (skin pos. + meas. fat thick + muscle thick mean +/- two std dev)
        for muscle.  The result is scaled by 1/20 since
        each pixel represents 0.5mm .
/home/wdo/rnc/analysis/mfiles/loc.m
     -- Find location of the largest peak in a sequence
        in a given range.  This works by taking the list
        of maxima provided by maxes.m (see below), and
        finding the list entry in the given range for
        which the function has the greatest value.
/home/wdo/rnc/analysis/mfiles/maxes.m
     -- Return indices of local maxima in a data sequence.
        This is a key routine.  It works by first convolving
        the data sequence by the filter [1 3 1], then computing
        a first order difference y(k) = x(k) - x(k - 1).
        Locations of local extrema are places where y(k) y(k+1) < 0.
        In other words, where y(k) changes sign.  A local maximum
        is any local extremum where y(k+1) > y(k).
```

3.2.3 Data file

```
/home/wdo/rnc/analysis/mfiles/measures.m
     -- Contains the mean and standard deviation information for
        fat and muscle thickness at all measurement locations.
```

3.2.4 Debugging tool

/home/wdo/rnc/analysis/mfiles/mark.m

-- Utility function to mark a specified point on a Matlab plot

3.3 Scripts

The following files are unix shell scripts which perform series of operations on the images in batch mode:

/home/wdo/rnc/analysis/scripts/process

-- Process data files from a particular animal into results files.

/home/wdo/rnc/analysis/scripts/process_cold

-- Process only cold data files.

/home/wdo/rnc/analysis/scripts/process_hide_on

-- Process only hide_on data files.

/home/wdo/rnc/analysis/scripts/process_hide_off

-- Process only hide_off data files.

4.0 Processing Mechanics

This section is devoted to describing the mechanics of the data processing in a step by step fashion. The processing sequence is slightly different between horizontal and skin scans, but the flow of the processing is not dependent on carcass state (i.e., cold, hide on, hide off) except in the names of files. We step through the processing of a horizontal scan first, then show how a skin scan differs.

4.1 Processing a (cold) horizontal scan

The following steps are done from a unix shell:

i) Convert pgm file to sunraster file called cold_xxx_temp

ii) Copy cold_xxx_temp to cold_xxx_temp1 (this appears to be obsolete).

iii) Shift columns up so that skin surface is flush with the top

of the image window. Store output file in filename.sun (e.g. clcgcm02.sun).

iv) Run Sticks on filename.sun, length 31 stick, raising each pixel to 1.5 power and renormalizing to 255 gray levels to enhance lines. Store output in filename.sti31 .

v) Convert sunrasterfile filename.sti31 to Matlab readable form filename.mat .

vi) Extract vertical slices of Sticks output image at five, ten and fifteen centimeters from the spine. Store the slices in filename.mat .

vii) Read animal carcass ID from position file; store ID number as animal number in filename.mat .

viii) Remove all *temp* files.

The following steps are done within a Matlab m-file, executed in batch mode from within the unix shell.

ix) Load filename.mat .

x) open output file measures_xxx .

xi) Load in fat, muscle thickness mean and standard deviation for 5cm location.

xii) Locate the skin surface.

xiii) Identify the fat/muscle boundary.

xiv) Identify the back wall of the muscle.

xv) Compute fat and muscle thicknesses.

xvi) Print data line to output file

xvii) Repeat xi) through xvi) for 10 and 15 cm locations.

The following steps are done from the original unix shell.

xviii) Copy measures_xxx to /bugs/results/measures-xxx

xix) Compress *.sun, *.mat, and *.sti31

4.2 Processing a skin scan

The processing of a skin scan is the same as the processing of a horizontal scan except for a few key differences:

i) No shifting of columns is necessary.

ii) The line enhancement program is the simpler onestika or onestikb, instead of full Sticks.

iii) There is no need to produce a Matlab readable version of the Sticks output image, or extract slices, because these things are incorporated in onestika and onestikb.

4.3 Executing the Programs

The software is executed by typing (at a unix prompt on ecstasy)

```
cd ~rnc/analysis/working
nice process xxx >& errors_xxx &
compress measures_xxx errors_* >& /dev/null
```

The result is a measures results file in the /bugs/results/ directory, a local copy of the measures results, a local error file, and various intermediate output files.

These commands can themselves be executed in a script.

5.0 References

[1] Hein, I. A. , Novakofski, J. A. , and O'Brien, W. D. Jr., ''Ultrasound Data Acquisition System Design for Collecting High Quality RF Data from Beef Carcasses in the Slaughterhouse Environment,'' Proc. IEEE Ultrasonics Symposium, Tuscon, AZ, 1992

[2] Lee, R. , et. al.

[3] Czerwinski, R. N. , Jones, D. L., and O'Brien, W. D. Jr. ''An Approach to Boundary Detection in Ultrasound Imaging,'' Proc.

IEEE Ultrasonics Symposium, Baltimore, MD, 1993.

[4] Czerwinski, R. N. , Jones, D. L., and O'Brien, W. D. Jr. ''Edge Detection in Ultrasound Speckle Noise,'' Proc. IEEE International Conference on Image Processing, Austin, TX, 1994.

[5] Czerwinski, R. N. , Jones, D. L., and O'Brien, W. D. Jr. ''Line and Boundary Detection in Speckle Images,'' submitted to IEEE Transactions on Image Processing.

[6] Czerwinski, R. N. , Jones, D. L., and O'Brien, W. D. Jr. ''Detection of Lines and Curves in Speckle Images - Application to Ultrasound Imaging,'' submitted to IEEE Transactions on Medical Imaging.

[7] O'Brien, W. D. Jr. ''Routine Scanning Protocol,'' August 1993.

VITA

Richard Norman Czerwinski received the B.S.E.E. degree *cum laude* from Drexel University, Philadelphia, PA in 1990, where he held a Presidential Scholarship, and was honored by the Alumni Association as an Outstanding Senior. He entered the Graduate College at the University of Illinois, Urbana, IL in the Department of Electrical and Computer Engineering, and received the M.S. degree in 1993. He was appointed a graduate research assistant in 1991 and 1992 in the Coordinated Science Laboratory and from 1992 through 1996 in the Bioacoustics Research Laboratory. During 1995 and 1996 he held a Radiation Oncology Training Fellowship awarded by the National Cancer Institute. In 1996, he took first place in the 27th Annual Student Paper Competition, sponsored by the University of Illinois Chapter of Sigma Xi. He has accepted a position on the technical staff of the Lincoln Laboratory of the Massachusetts Institute of Technology, Lexington, MA, in the Systems and Analysis Group. His current research interests are in statistical ultrasound signal and image processing and time-frequency signal analysis. He is a member and former chapter officer of Eta Kappa Nu and Tau Beta Pi.